GRAZ UNIVERSITY OF TECHNOLOGY

DOCTORAL THESIS

On the Performance Testing of MIMO Enabled Wireless Mobile User Devices

Author:
Dipl.-Ing. Bernhard AUINGER

Supervisor:
Univ.-Prof. Dipl.-Ing. Dr. techn. Wolfgang BÖSCH

conducted at the

Institute of Microwave and Photonic Engineering

Assessors/Examiners:
Univ.-Prof. Dipl.-Ing. Dr. techn. Wolfgang BÖSCH
Priv.-Doz. Dr. techn. Thomas ZEMEN

June 2015

Declaration of Authorship / Eidesstattliche Erklärung

I, Dipl.-Ing. Bernhard AUINGER, born in Grieskirchen, March 3rd, 1977, declare that I have authored this thesis independently, that I have not used other than the declared sources/resources, and that I have explicitly marked all material which has been quoted either literally or by content from the used sources. The text document uploaded to TUGRAZ online is identical to the present doctoral dissertation.

Ich, Dipl.-Ing. Bernhard AUINGER, geboren am 3. März 1977 in Grieskirchen, erkläre an Eides statt, dass ich die vorliegende Arbeit selbstständig verfasst, andere als die angegebenen Quellen/Hilfsmittel nicht benutzt, und die den benutzten Quellen wörtlich und inhaltlich entnommenen Stellen als solche kenntlich gemacht habe. Das in TUGRAZ online hochgeladene Textdokument ist mit der vorliegenden Dissertation identisch.

Signed / Unterschrieben: _____

Date / Datum: _____

i

GRAZ UNIVERSITY OF TECHNOLOGY

Abstract

On the Performance Testing of MIMO Enabled Wireless Mobile User Devices

by Dipl.-Ing. Bernhard AUINGER

With the vastly progressing development of mobile communication standards under the umbrella terms *fourth generation, fifth generation* (4G, 5G) many new techniques have found and will find their way in mobile wireless devices. They will allow way higher data throughput rates, even when the user is moving. These methodologies are enabled through the risen computing power of state of the art integrated circuits. Among others, the so-called *Multiple-Input Multiple-Output* (MIMO) antenna technology is a crucial part, because it introduces the additional dimension SPACE to the wireless transmission system. It employs more antennas on both transmitter and receiver side to transmit independent data streams in the same frequency band. Mobile wireless equipment manufacturers and network providers want to compare the performance of devices, including antennas, analog frontends, digital receiving algorithms, baseband processing and so on. Old well known *single-input single-output* (SISO) performance tests do not suffice these new exigences, like to test multi antenna systems, anymore.

This thesis deals with the performance tests of MIMO transmission systems. A figure of merit for MIMO antenna performance will be introduced, namely the *envelope correlation coefficient* (ECC). Investigations of behaviour of a reference antenna design for wireless standard *long term evolution* (LTE) Band 13 (751 MHz) will be presented, including a comparison between measured and simulated results.

Progressing from antenna system tests to performance tests of entire wireless devices, an overview of the current test methods will be given. The worldwide *3rd generation partnership project* (3GPP) proposed these methods. This thesis provides the investigations on a new and promising one using an anechoic chamber, the 'Decomposition Method'. It also shows the validity of the method in the majority of application cases and defines the error bounds. It provides the necessary mathematical foundations and shows strengths and limitation of the test method.

Acknowledgements

First of all, this PhD thesis would not have been possible without the support of the company *Rohde & Schwarz, Munich, Germany*. The company enabled this research work and the publication of their measurement results. I owe my deep gratitude to Dr.-Ing. Christoph von GAGERN and Dr.-Ing. Adam TANKIELUN at *Rohde & Schwarz*, who gave me the opportunity to execute this doctoral thesis and strongly supported me. I would like to use this opportunity to articulate a big thanks to my doctoral thesis supervisor Univ.-Prof. Dipl.-Ing. Dr. techn. Wolfgang BÖSCH and my supervisor Dipl.-Ing. Dr.techn. Michael GADRINGER at the *Institute of Microwave and Photonic Engineering, University of Technology Graz, Austria*, for breaking new scientific grounds with me. It was a pleasure to work with you.

I am indebted to Assoc.-Prof. Dipl.-Ing. Dr. Klaus WITRISAL, Dipl.-Ing. Dr. Andreas PEDROSS-ENGEL, Dipl.-Ing. Dr.techn. Bernhard GEIGER, Dipl-Ing. Dr.tech. Paul MEISSNER, Dipl.-Ing. Erik LEITINGER at the *Institute of Signal Processing and Speech Communication, University of Technology Graz, Austria*, Assoc.-Prof. Dipl.-Ing. Dr.techn. Univ.-Doz. Wilfried GAPPMAIR at *the Institute of Communication Networks and Satellite Communications, University of Technology Graz, Austria* and Priv.-Doz. Dr.techn. Thomas ZEMEN at *the Austrian Institute of Technology (AIT), Vienna, Austria*, they contributed towards this thesis with great discussions and essential technical suggestions.

I gratefully acknowledge my office mates Dipl.-Ing. Philipp FREIDL and Hasan Noor KHAN, MSc, who know the ups and downs of the process of writing a PhD thesis, for the good company and the fruitful discussions.

I am owing a big obeisance to my teacher Oswald ELLEBERGER, for sharing his traditional knowledge and essential basics. Thanks for your endless patience.

For letting me experience unconventional, simple and well working solutions for technical problems from early childhood on, I want to thank Mr. Ernst BAUERECKER.

My dear girlfriend, Ms. Lisa REITER, always is a source of smile and inspiration, she gives me big relief and encouragement.

Last but not least, I would like to show my gratitude to my parents Mrs. Paula AUINGER and Mr. Rudolf AUINGER. They gave me a very good basis for life and had the patience for a youngster taking dozens of broken TV sets apart and awaking them to new life.

Contents

List of Figures

List of Tables

Abbreviations

3GPP	**3**rd **g**eneration **p**artnership **p**roject
ANT	**ant**enna
BL	**b**aseline
CH	**ch**annel
DCM	**d**e**c**omposition **m**ethod
Det	**det**ector
ECC	**e**nvelope **c**orrelation **c**oefficient
ICD	**i**nverse **c**hannel **d**etector
IID	**i**dentical **i**ndependently **d**istributed
LTE	**l**ong **t**erm **e**volution
MIMO	**m**ultiple **i**nput **m**ultiple **o**utput
MISO	**m**ultiple **i**nput **s**ingle **o**utput
MMSE	**m**inimum **m**ean **s**quare **e**rror
Mod	**mod**ulator
OTA	**o**ver **t**he **a**ir
OA	**o**ver**a**ll
P/S	**p**arallel **s**erial translator
UE	**u**ser **e**quipment
RX	**r**e**c**eive
SF	**s**ub**f**rame
SIMO	**s**ingle-**i**nput **m**ultiple-**o**utput
S/P	**s**erial **p**arallel translator
TX	**t**ransmit
ZF	**z**ero **f**orcing

Chapter 1

Introduction

1.1 Concept and Motivation

The users have become agile. They want to use different applications like social media and streaming services wherever they may reside. They use a variety of devices, all of them are linked in a certain way, whether directly or to bigger networks. They want to be connected and involved. These needs technically come down to the following technical requirements the wireless transmission system has to fulfill: coverage, adaptive transmission systems, intelligent networks, high data throughput rates and stable connections. The answer to these risen exigences is covered by various fields of electrical engineering. The *multiple-input multiple-output* (MIMO) antenna technology benefits from former severe drawbacks of wireless technology, the multipath radio propagation. The transmission channels can be treated as if they were independent, having different gains. *"If a student would have said twenty-five years ago that he wants to transmit data by multiple closely spaced antennas to multiple antennas on the receiver in the same frequency band at the same time, he would have suspended the exam. Nowadays we do it, without any ache"*[14]. Knowing the atrocities that happen to the transmitted signals while propagating from the transmitter to the receiver, these effects can almost be canceled by equalization. These aftermaths can also be covered by stochastic models, which allow intelligent allocation of the payload in the domains time, frequency and space.

With all these possibilities many challenges have to be taken and problems have to be solved in the design phase of the user equipment. Having the working device, a prototype or a partly implemented version on the table, the manufacturer or the network provider

1

wants to compare the performance against other products. Due to the exploitation of multi-path propagation in MIMO-enabled user equipment, the ways of testing the user device efficiency have to be rethought. Hardware and software is strongly entangled. Old SISO test systems are not able to cover the needs for multi-antenna transmission systems. New test systems and different figures of merit are defined to express this combined system behaviour objectively.

Organizations have defined test cases and models for representative transmission scenarios, that should reflect the "real world" behaviour. All test systems try to implement these transmission models in their setup in a realistic way. They have different benefits and downsides regarding measurement equipment costs, setup and test time, calibration effort, spatial resolution and mapping real transmission scenarios to certain antenna constellations, to name a few.

This thesis will introduce and guide the reader into this heterogeneous world between electromagnetism, antenna theory, discrete time signal processing and matrix calculus. It will explain figures of merit for antennas and a simple method for measurement and simulation to rate the MIMO capabilities of antenna systems with coupled antennas. It discusses different test methodologies and will deeply focus on one very promising solution, the *"Decomposition Method"*. This approach combines the split performance measurements of the antenna system and the algorithmic performance tests. Up till now, it has not been investigated theoretically, although it has proven functionality in several practical tests. The breaking new thing about this thesis is to end this circumstance and to investigate the method theoretically. The author analyzes it in different ways. The strong sides will be highlighted as well as the limitations will be given.

1.2   Outline and Contribution

Chapter 1 is this introduction.

Chapter 2 provides the necessary antenna theory, electromagnetic field foundations and a bird's view on MIMO communication systems. The author summarizes the existing theory.

Chapter 3 presents a commonly used figure of merit for MIMO antenna systems, the *Envelope Correlation Coefficient* (ECC). A practically applicable measurement method using the ECC to rate the MIMO capabilities of antenna systems will be shown, from

theory to the comparison of measurement and simulation of a reference antenna system. The author presents the existing theory of the ECC and shows his investigations of a coupled MIMO antenna system employing *Rohde & Schwarz* reference antennas. He investigates the ECC for the different antenna distances and draws conclusions.

The worldwide cooperation *3rd Generation Partnership Project* (3GPP) has taken responsibility for the standardization process and provided several approaches for tests of entire wireless mobile devices. **Chapter 4** presents these methods, also looking at their pros and cons. One of these tests shows some big benefits in terms of test time, setup cost and spatial resolution, the *Decomposition Method*. The author summarizes several documents to give a good overview on the methods and takes a closer theoretical look on the "Decomposition Method".

Chapter 6 deals with a different validation method of the DCM using the MIMO channel capacity formulas. This approach is more generic as it does not contain certain receiving concepts. The author establishes the validity of the DCM by using a different way and demonstrates the results.

Chap. 7 shows the numerical investigations by simulation of transmission systems employing an ICD/ZF and *Minimum Mean Square Error* (MMSE) receivers. The author employs the substantial parts of the *Long Term Evolution* (LTE) standard for the implementation of the simulations. He reveals the validity of the Decomposition Method in a wide range of applications, including the usage of common LTE reference antennas. The author also exhibits comparisons of the simulation results to measurement data and shows the constraints of the method for successful practical usage.

Chapter 8 contains the results of the measurements performed by our partners at the company *Rohde & Schwarz*. The author presents the experimental validation of the decomposition method.

Finally the author summarizes his work in **Chapter 9** by giving a conclusion.

Chapter 2

Foundations

2.1 Signal Theory of MIMO Systems

With the rising demand on wireless data channels, new ressources had to be made accessible. SPACE is the dimension that has become available by usage of the MIMO antenna systems and by exploitation of the multipath propagation scenarios. Basically two strategies can be embarked. The former one is to utilize the possibility of mathematically separating signals that are transmitted as multiple layer data streams in the same frequency band. This allows a substantial increase in terms of data rate. The latter one rises the transmission security, decreasing the number of dropped connections. This can be achieved by exploiting the diversity of multiple antenna systems or by better interferer caused disturbance suppression using beam forming.

Different wireless transmission concepts with multiple antennas at one side and a single antenna on the other side of the transmission chain are available. They are called *Multiple-Input Multiple-Output* (MISO) or *Single-Input Multiple-Output* (SIMO) systems. For example *space time-coding*, like the *Alamouti-scheme*, in the MISO case and *Maximum Ratio Combining* (MRC) in the SIMO case can be used to accomplish a more robust transmission than in the SISO case. Nevertheless, a MIMO system employing a higher number of antennas than MISO or SIMO systems delivers better results.

This thesis deals with the general case of a MIMO antenna transmission system with multiple antennas on both sides. To achieve highest possible gains it is crucial to have

knowledge about the transmission channel at the transmitter side. In the best case the instantaneous channel matrix is known. Still gain can be achieved in comparison to SISO systems, if the receiving systems only have statistical knowledge of the channel. This chapter mainly follows [15] and also takes the explanations of [11] and [16] into account.

The data are transmitted from the base station through a wireless multi-path propagation channel to the UE. Figure 2.1 illustrates such a situation encountered by the mobile device. Reflections from scatterers arrive under different angles, angular spread and time delay, as well as *Line Of Sight* (LOS) connections are possible.
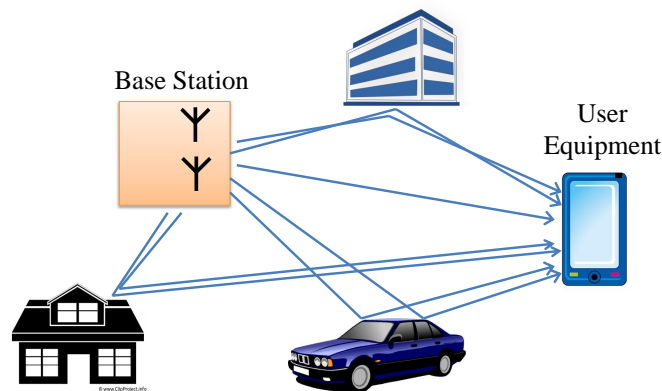
FIGURE 2.1: Real world transmission scenario - downlink scenario

Switching to block diagrams, the configuration of a general MIMO transmission system is shown in Fig. 2.2.
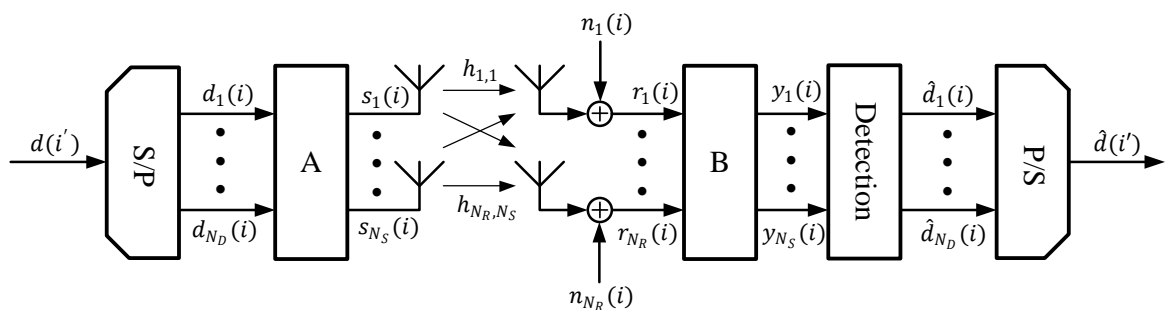
FIGURE 2.2: General MIMO transmission system

On the left side in Fig. 2.2 the transmitter with the TX antennas is shown, we can see the correlated wireless channel in the middle and the receiver on the right side. The arrows in the block diagram indicate the direction of the data flow.

The input data $\mathbf{d}(i')$ is transformed to column data vector $\mathbf{d}(i)$

$$\mathbf{d}(i) = \begin{bmatrix} d_1(i) & \dots & d_{N_{\mathrm{D}}}(i) \end{bmatrix}^T \tag{2.1}$$

and is multiplied with the predistortion matrix $\mathbf{A}$. This results in the transmit data vector $\mathbf{s}(i)$,

$$\mathbf{s}(i) = \begin{bmatrix} s_1(i) & \dots & s_{N_{\mathrm{S}}}(i) \end{bmatrix}^T \tag{2.2}$$

which is transmitted by several antennas over the wireless channel $\mathbf{H}$ (2.5). The transmitted symbols of $\mathbf{s}(i)$ completely overlap frequency [11]. N_{S} is the number of transmit antennas, N_{D} is the number of independent data streams.

$$\mathbf{s}(i) = \mathbf{A}\,\mathbf{d}(i), \quad \mathbf{d}(i) \in \mathbb{C}^{N_{\mathrm{D}} \times 1}, \quad \mathbf{s}(i) \in \mathbb{C}^{N_{\mathrm{S}} \times 1}, \quad \mathbf{A} \in \mathbb{C}^{N_{\mathrm{S}} \times N_{\mathrm{D}}} \tag{2.3}$$

The receiver employs N_R receive antennas, therefore the received vector $\mathbf{r}(i)$ is $[N_{\mathrm{R}} \times 1]$ dimensional. As this thesis only deals with frequency flat channels and delay free matrices, the convolution simplifies to a multiplication of signals and matrices. Multiplying $\mathbf{r}(i)$ with the post-distortion matrix $\mathbf{B}$ results in the vector $\mathbf{y}(i)$

$$\mathbf{r}(i) = \begin{bmatrix} r_1(i) & \dots & r_{N_{\mathrm{R}}}(i) \end{bmatrix}^T$$
$$\mathbf{y}(i) = \begin{bmatrix} y_1(i) & \dots & y_{N_{\mathrm{S}}}(i) \end{bmatrix}^T \tag{2.4}$$
$$\mathbf{y}(i) = \mathbf{B}\,\mathbf{r}(i), \quad \mathbf{r}(i) \in \mathbb{C}^{N_{\mathrm{R}} \times 1}, \quad \mathbf{y}(i) \in \mathbb{C}^{N_{\mathrm{D}} \times 1}, \quad \mathbf{B} \in \mathbb{C}^{N_{\mathrm{D}} \times N_{\mathrm{R}}}$$

$\mathbf{A}$ and $\mathbf{B}$ are important for the mathematical split of the MIMO channel into separated channels. The data vector $\mathbf{s}(i)$ is transmitted over the wireless channel that is assumed to be memory-less in the time domain. Its response in the frequency domain is flat (*"flat fading channel"*). The author assumes this fact because of the flat fading nature of *orthogonal frequency division multiplexing* (OFDM) narrow-band channels. E.g. the wireless communication standard LTE uses a bandwidth of $15\,\mathrm{kHz}$ per subcarrier and therefore the channel response can be regarded as flat fading.

The receiver employs the data vector $\mathbf{y}(i)$ for the detection. The detected data vectors $\hat{\mathbf{d}}(i)$ are transformed into a single serial data stream ("P/S" block).

The transmission characteristics of the channel are described with an $[N_R \times N_S]$ dimensional matrix $\mathbf{H}$, that contains the complex weights h_{xy}. They describe the path gain from transmit antenna x to receive antenna y (see channel model in Fig. 2.2). Block

fading is assumed, this means that during a block transmission the channel is assumed stay constant. The discrete time index i is dropped for the sake of simplicity.

$$\mathbf{H} = \begin{bmatrix} h_{1,1} & h_{1,2} & \dots & h_{1,N_S} \\ h_{2,1} & h_{2,2} & \dots & h_{2,N_S} \\ \vdots & \vdots & \ddots & \vdots \\ h_{N_R,1} & h_{N_R,2} & \dots & h_{N_R,N_S} \end{bmatrix}, \quad h_{x,y} \in \mathbb{C} \tag{2.5}$$

The receiver input signal $\mathbf{r}(i)$ contains the data, as well as intrinsic receiver noise coming from the receiver circuitry. Mathematically the noise can be described with a noise vector $\mathbf{n}(i)$, whose elements are independent identically distributed (IID) Gaussian random variables. The MIMO signal model is described with matrix equations modeling a transmission in the base band.

$$\mathbf{r}(i) = \mathbf{H}\,\mathbf{s}(i) + \mathbf{n}(i) = \mathbf{H}\,\mathbf{A}\,\mathbf{d}(i) + \mathbf{n}(i). \tag{2.6}$$

Assuming the channel matrix $\mathbf{H}$ is known, a singular value decomposition can be performed

$$\mathbf{H} = \mathbf{U}\,\boldsymbol{\Sigma}\,\mathbf{V}^{\mathrm{H}}, \quad \mathbf{U} \in \mathbb{C}^{N_R \times N_R}, \quad \mathbf{V} \in \mathbb{C}^{N_S \times N_S} \tag{2.7}$$

$\mathbf{H}^{\mathrm{H}}$ is the Hermitian transpose of the channel matrix $\mathbf{H}$. $\mathbf{U}$ contains the eigenvectors of $\mathbf{HH}^{\mathrm{H}}$ in its columns and $\mathbf{V}$ the eigenvectors of $\mathbf{H}^H\mathbf{H}$, respectively. Both $\mathbf{U}$ and $\mathbf{V}$ are unitary matrices

$$\mathbf{U}^H\,\mathbf{U} = \mathbf{I}_{N_R}, \quad \mathbf{V}^H\,\mathbf{V} = \mathbf{I}_{N_S} \tag{2.8}$$

The matrix $\boldsymbol{\Sigma}$ has the dimension $[N_R \times N_S]$ and contains the singular values σ_μ on its main diagonal ($\mu \in 1, 2, .., N_S$), all other elements are zero

$$\boldsymbol{\Sigma} = \begin{bmatrix} \sigma_1 & & & 0 \\ & \sigma_2 & & \\ & & \ddots & \\ 0 & & & \sigma_N \end{bmatrix} \qquad N = \min(\,N_R, N_S) \tag{2.9}$$

By multiplying $\mathbf{r}(i)$ with $\mathbf{U}^{\mathrm{H}}$ and replacing the channel matrix $\mathbf{H}$ with the result of the singular value decomposition, a different representation is obtained

$$\mathbf{y}(i) = \mathbf{U}^{\mathrm{H}}\mathbf{r}(i) = \mathbf{U}^{\mathrm{H}}\mathbf{U}\boldsymbol{\Sigma}\mathbf{V}^{\mathrm{H}}\mathbf{s}(i) + \mathbf{U}^{\mathrm{H}}\mathbf{n}(i) = \boldsymbol{\Sigma}\mathbf{V}^{\mathrm{H}}\mathbf{s}(i) + \tilde{\mathbf{n}}(i). \qquad (2.10)$$

The noise vector $\tilde{\mathbf{n}}(i)$ is the result of the multiplication of a unitary matrix with the original noise vector. The statistical properties of $\mathbf{n}(i)$ and $\tilde{\mathbf{n}}(i)$ are the same [15]. $\mathbf{V}^{\mathrm{H}}\mathbf{s}(i)$ is said to be the data vector $\mathbf{d}(i)$

$$\mathbf{d}(i) = \mathbf{V}^{H}\mathbf{s}(i) \qquad (2.11)$$

Following the signal flow from transmitter in direction to the receiver, this implies that the transmit vector $\mathbf{s}(i)$ equals

$$\mathbf{s}(i) = \mathbf{V}\mathbf{d}(i). \qquad (2.12)$$

Remember, $\mathbf{V}$ is a unitary matrix. Using (2.10) and (2.12) leads to

$$\mathbf{y}(i) = \boldsymbol{\Sigma}\,\mathbf{d}(i) + \tilde{\mathbf{n}}(i). \qquad (2.13)$$

Equation (2.13) is now the nucleus of the MIMO transmission scheme. The received data vector $\mathbf{y}(i)$ is directly calculated by a multiplication of the diagonal matrix $\boldsymbol{\Sigma}$ with the data vector $\mathbf{d}(i)$ and is only disturbed by the noise vector $\tilde{\mathbf{n}}(i)$. Taking a single equation from the vector $\mathbf{y}(i)$, it can be seen that the MIMO system can be decomposed in N_{S} independent SISO channels (2.14). The singular values σ_μ represent the gains of the channels. If one of them is very small, the assigned channel will almost vanish.

$$y_\mu = \sigma_\mu d_\mu(i) + \tilde{n}_\mu(i), \quad \mu \in \{1, ..., N\}, \qquad N = \min(\,N_{\mathrm{R}}, N_{\mathrm{S}}). \qquad (2.14)$$

The matrices of Fig. 2.2 are set to

$$\mathbf{A} = \mathbf{V} \qquad \mathbf{B} = \mathbf{U}^{\mathrm{H}}, \qquad (2.15)$$

allowing a separation in parallel independent SISO channels. Fig. 2.3 shows the block diagram of the transmission system with additionally added gain blocks $\sqrt{p_\mu}$. They allow easy power allocation to the channels, as used in the *Waterfilling-Principle* [17]. This concept can be used for optimizing power distribution between the MIMO channels
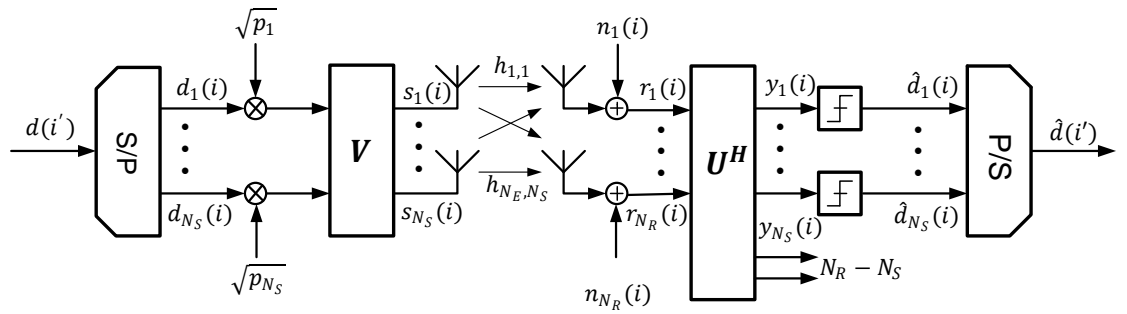
FIGURE 2.3: MIMO transmission system with applied matrices

for a given overall transmission power.

To exploit the full MIMO gain, the transmitter has to have knowledge about the channel, to calculate the matrix $\mathbf{V}$. This channel estimation can be done by transmission of known pilot signals, estimating the channels in the receiver by using these known signals and feeding these estimated values back to the transmitter.

The separate channels are depicted in the block diagram in Fig. 2.4.
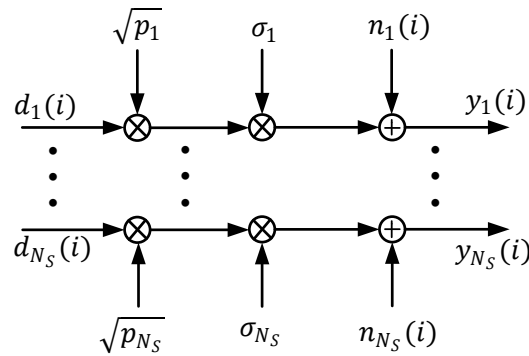
FIGURE 2.4: Simplified MIMO scheme - MIMO channels as separated channels

A MIMO transmission system takes advantage of multipath propagations. It sends different data streams through multiple antennas via different propagation paths. The data streams are usually uncorrelated (2.16). The expectation value is denoted by $\mathscr{E}\{\}$, $\mathbf{d}_\mu(i), \mathbf{d}_\nu(i)$ are the input data vectors.

$$\mathscr{E}\{\mathbf{d}_\mu(i)^{\mathrm{H}}\mathbf{d}_\nu(i)\} = 0 \qquad \forall\, \mu, \nu \in 1, 2, ..., N_{\mathrm{S}}; \quad \mu \neq \nu \qquad (2.16)$$

Figure 2.5 maps the real world scenario of Fig. 2.1 into a block diagram (base band representation). The base station processes the uncorrelated data vector $\mathbf{d}$ and delivers the still uncorrelated symbol vector $\mathbf{s}$ and transmits it by its transmit (TX) antennas over the channel to the receiver with its RX antennas, resulting in the received data vector $\mathbf{r}$

$$\mathbf{r} = \mathbf{H}_{\text{antenna,rx}} \ \mathbf{H}_{\beta,1} \ \mathbf{H}_{\text{channel}} \ \mathbf{H}_{\alpha,1} \ \mathbf{H}_{\text{antenna,tx}} \ \mathbf{s} \qquad (2.17)$$

By MIMO signal processing in the base station and in the UE the multipath propagation channel can be treated as separated paths, which results in an uncorrelated channel matrix $\mathbf{H}_{\text{channel}}$ (Chap. 2.1). The TX antenna is represented by two blocks, the TX antenna gain block, and the TX antenna correlation block. The TX antenna gain block $\mathbf{H}_{\text{antenna,tx}}$ is assumed to be a unity matrix, and a correlation matrix $\mathbf{H}_{\alpha,1}$, which depicts the coupling between the base station antenna elements. The RX antenna of the UE is represented by the diagonal gain matrix $\mathbf{H}_{\text{antenna,rx}}$ and the correlation matrix $\mathbf{H}_{\beta,1}$, representing the coupling between the RX antenna elements. Chapter 5.4.1 will explore further details on the uncorrelated channel with correlation matrices, so-called *Kronecker channel model*.

The data vectors $\mathbf{d}_{\mu}(i)$ $(\mu \in \{1, 2, ..., N_{\text{S}}\})$ are transmitted over the mathematically separated paths, the base station antenna system and UE antenna system add correlation to the transmitted data vectors, as depicted by the blocks $\mathbf{H}_{\alpha,1}$ and $\mathbf{H}_{\beta,1}$. $\mathbf{H}_{\alpha,1}$ is part of the base station and $\mathbf{H}_{\beta,1}$ is part of the UE [1]. This decomposition of the antenna system properties eases mathematical treatment.

The less the elements of the received data vector $\mathbf{r}$ are correlated, the higher is the performance of the transmission system, as the investigations in this thesis exhibit in Chap. 7 and App. A. High performance in this sense is characterized by high data throughputs at low downlink power levels. The receiver sees the "overall" channel $\mathbf{H}_{\text{overall}}$

$$\mathbf{H}_{\text{overall}} = \mathbf{H}_{\text{antenna,rx}} \ \mathbf{H}_{\beta,1} \ \mathbf{H}_{\text{channel}} \ \mathbf{H}_{\alpha,1} \ \mathbf{H}_{\text{antenna,tx}} \qquad (2.18)$$

This thesis employs *Zero Forcing / Inverse Channel Detection* (ZF/ICD) and *minimum mean square error* (MMSE) receivers. These receivers use the inverse of the "overall" $\mathbf{H}_{\text{overall}}$ channel for the receiving process. The more the channel matrix elements of

---

[1]For investigations in Chap. 6 and Chap. 7 the correlation matrices $\mathbf{H}_{\alpha,1}$ and $\mathbf{H}_{\beta,1}$ are part of the channel model. The reason is that in the measurements these matrices are emulated by the channel emulator.
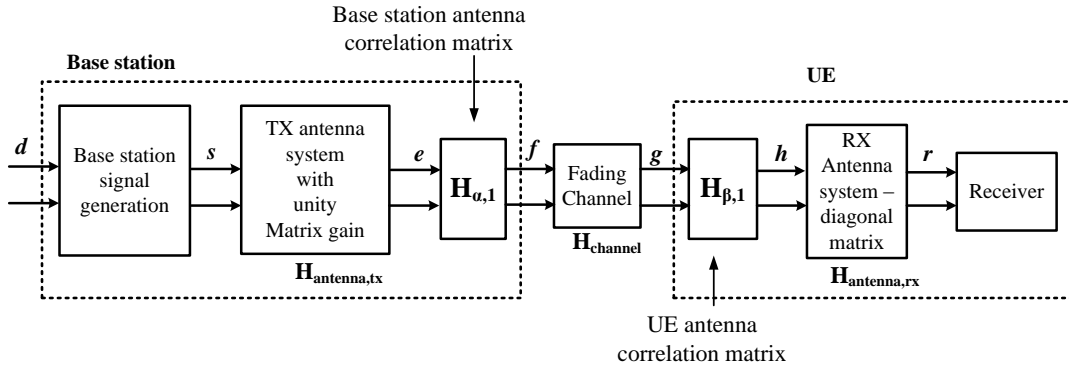
FIGURE 2.5: Downlink transmission scenario block diagram with fading channel matrix $\mathbf{H}_{\text{channel}}$, correlation matrices $\mathbf{H}_{\alpha,1}$ and $\mathbf{H}_{\beta,1}$, which are incorporated in base station and UE

$\mathbf{H}_{\text{overall}}$ are correlated, the worse is its conditioning, resulting in intrinsic noise enhancement in the receivers. The risen noise in the receiver affords more downlink power for a consistant throughput.

2.2 Antenna and Field Theory

Antennas and electromagnetic wave propagation are a crucial part of every wireless transmission system. Therefore a short introduction to these foundations is given here. An electromagnetic wave very far away from its source is approximately planar. In free space it can be modeled with a TEM (*transversal electromagnetic*) wave [18].
The electric field vector $\vec{E}$, the magnetic field vector $\vec{H}$ and the propagation direction unit vector $\vec{e}_r$ build an orthogonal right handed trihedron. There is no field component in the propagation direction (Fig. 2.6).

The fixed relation between the amplitudes of the electric field $\vec{E}$ and the magnetic field $\vec{H}$ is described by free space impedance Z_w: $Z_w = E/H$. $\vec{H}$ and $\vec{E}$ are orthogonal to each other [19]. Therefore it is sufficient to consider the electric field $\vec{E}$ only. The vector $\vec{E}$ is dependent on the time t and the distance from its origin r. It can be described with two orthogonal phasors and their unit vectors $\vec{e}_\Phi$ and in $\vec{e}_\Theta$ in the Φ and Θ plane
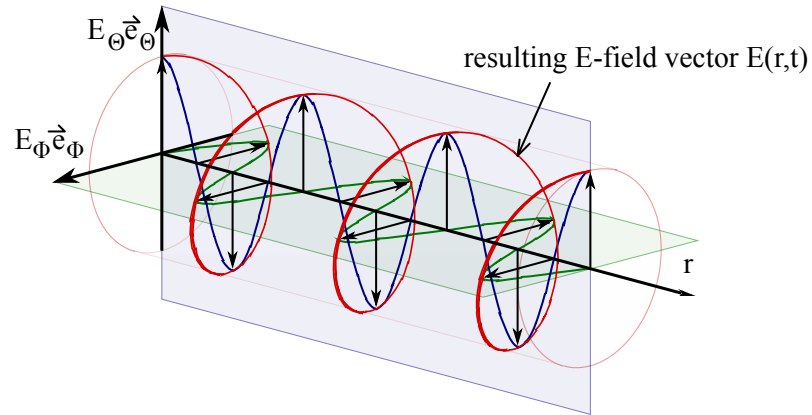
FIGURE 2.6: E-Field of propagating polarized EM-wave [1]

of a spherical coordinate system

$$
\begin{aligned}
\vec{E}(r,t) = \vec{E}_\Phi(r,t,\Phi,\Theta) + \vec{E}_\Theta(r,t,\Phi,\Theta) = \\
Re(\vec{e_\Phi}E_\Phi(r)e^{j\omega t} + \vec{e_\Theta}E_\Theta(r)e^{j\omega t}) = \\
Re(\vec{e_\Phi}E_\Phi e^{j\omega t - k_0 r} + \vec{e_\Theta}E_\Theta e^{j\omega t - k_0 r}) = \\
\vec{e_\Phi}E_\Phi cos(\omega t + k_0 r) + \vec{e_\Theta}E_\Theta cos(\omega t + k_0 r)
\end{aligned}
\tag{2.19}
$$

In this sense $\vec{e_\Phi}$ and $\vec{e_\Theta}$ denote the unit vectors in Φ and Θ direction (Fig. 2.7). Unit vector $\vec{e}_\Theta$ points in Θ direction (Fig. 2.7). Unit vector $\vec{e}_r$ points in the propagation direction. The wave number k_0 denotes the number of wavelengths λ_0 that fit in a
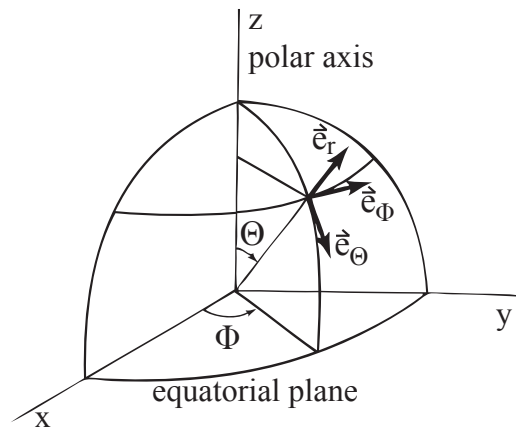
FIGURE 2.7: Coordinate system with unit vectors

complete cycle of 2π [18], [20].

$$
k_0 = \frac{2\pi}{\lambda_0} \qquad \left[\frac{\text{rad}}{\text{m}}\right]
\tag{2.20}
$$

The two E-field parts $\vec{E}_\Phi$ and $\vec{E}_\Theta$ are locally orthogonal to each other. $\vec{S}_r$ is the Poynting vector, which describes the power density of a TEM wave in propagation direction $\vec{S}_r = \vec{E} \times \vec{H}$ [2], as shown in Fig. 2.9.

The antennas are a crucial part of every transmission system. *Kraus et al* defined an antenna the following way [2]: "*The transmitting antenna is a region of transition from a guided wave on a transmission line to a free-space wave. The receiving antenna is a region of transition from free-space wave to a guided wave on a transmission line. So to say, an antenna is a transducer between a guided wave and a free-space wave, and vice versa. The antenna is a device which interfaces a circuit and space*". Fig. 2.8 illustrates this quotation.
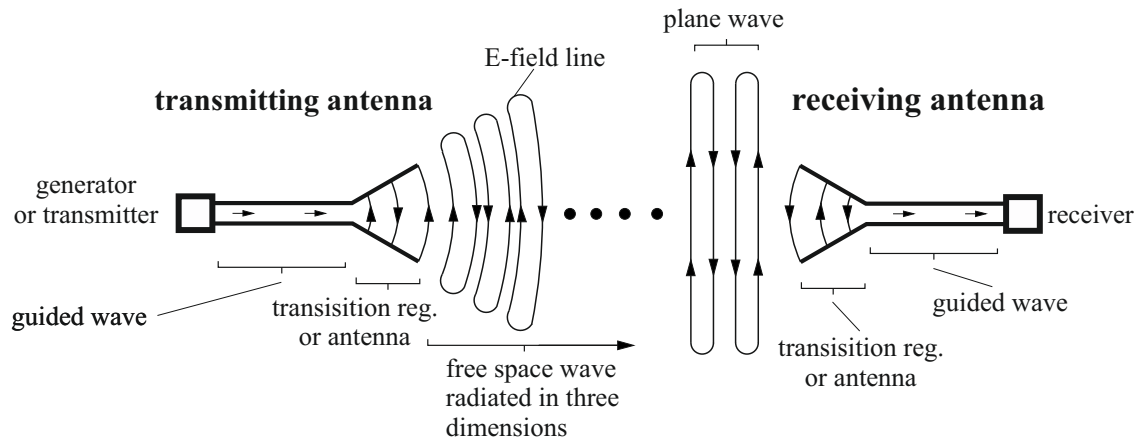
FIGURE 2.8: General wireless transmission system with antennas explaining the different regions [2]

For MIMO antenna systems it is important to know the received signals in their amplitude and relative phase, otherwise MIMO processing is not possible [15]. The transmitting and receiving antenna systems are assumed to be far away from each other. The distance between them is in the far field region of both antenna systems, therefore far field patterns are used [21]. The minimum distance of one antenna to another antenna to be in the farfield region d_0 can be calculated by [2]

$$d_0 \geq \frac{2D^2}{\lambda} \tag{2.21}$$

D is the biggest antenna dimension and λ is the wavelength. The pattern are mostly presented in the spherical coordinates system, as it allows convenient mathematical

treatment. The coordinates are the azimuth angle Φ and the zenith angle Θ, as shown in Fig. 2.9(a). The distance from the origin of the coordinate system to the point is r.
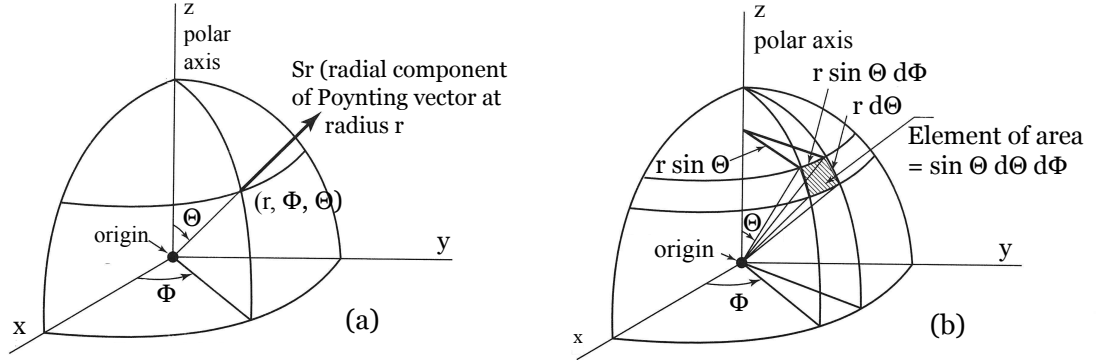
FIGURE 2.9: Spherical coordinate system [2]

The *normalized antenna E-Field Pattern* $F_\Phi(\Phi, \Theta)_n$ and $F_\Theta(\Phi, \Theta)_n$

$$
\begin{aligned}
F_\Phi(\Phi, \Theta)_n &= \frac{F_\Phi(\Phi, \Theta)}{F_\Phi(\Phi, \Theta)_{max}} \\
F_\Theta(\Phi, \Theta)_n &= \frac{F_\Theta(\Phi, \Theta)}{F_\Theta(\Phi, \Theta)_{max}}
\end{aligned}
\tag{2.22}
$$

is defined by the ratio of the E-field at a certain angle constellation $F_\nu(\Phi, \Theta)_n$ divided by the maximum E-Field $F_\nu(\Phi, \Theta)_{max}$ in a certain polarization ($\nu \in \Phi, \Theta$) [2]. Please note that subscript Φ and Θ denote polarizations in $\vec{e}_\Phi$ and $\vec{e}_\Theta$ direction, normal Φ and Θ describe coordinate angles, n is the number of the antenna.

The complex envelope of the received voltage $V(t)$ at the antenna is

$$
V(t) = c \oint \vec{E}(\Omega)\vec{F}(\Omega)d\Omega
\tag{2.23}
$$

where Ω is a set of angles containing the angles Φ and Θ [22], factor c is a proportionality constant.

$$
\Omega = \{\Phi, \Theta\}
\tag{2.24}
$$

The integrand is defined as

$$
\oint d\Omega = \int_0^{2\pi} \int_0^{\pi} \sin \Theta \, d\Phi \, d\Theta
\tag{2.25}
$$

and is visualized in Fig. 2.9(b). Any movement of the transmit and receive antennas is neglected, therefore no Doppler Shift is applied in (2.23).

Chapter 3

Antenna Performance Tests for MIMO Capabilities

3.1 Introduction to the Envelope Correlation Coefficient

Looking at small sized hand held user equipment (UE), it is likely that the antennas are closely spaced to each other. This proximity introduces unwanted coupling effects and consequently adds correlation of to the received data vector $\mathbf{r}$ (2.5), resulting in a performance degradation of the investigated systems. An important figure of merit to quantify these coupling effects in *Multiple Input Multiple Output* (MIMO) antenna systems is the *Envelope Correlation Coefficient* (ECC). The references [23–37] also investigate antenna systems with closely coupled antenna elements. They all employ the ECC as a figure of merit because of its tremendous influence on the receiver performance.

This chapter presents the exemplary investigations on two coupled planar reference antennas for LTE Band 13 (uplink 777 MHz to 787 MHz, downlink 746 MHz 756 MHz), designed by the company *Rohde & Schwarz*. The results are presented by numeric simulation and by measurement and a comparison between both is given in this chapter. A good agreement between the simulated and the measured ECC can be reported.

3.2   Theoretical Background

The ECC ρ_e is an important figure of merit for the comparison of MIMO capabilities of coupled antennas. It was originally suggested by *Vaughan* and *Andersen* in [38].
The following considerations are for an antenna system with two antennas. The incident E-field $\vec{E}$ consists of two polarization parts, as described in (2.19). The EM waves steming from different directions are assumed to be uncorrelated, since their phases are not dependent on each other. The directions are indicated by the angle constellation Ω, which indicates the spherical angles for the waves as well as for the antenna pattern in zenith (Θ) and azimuth (Φ). The angle constellation Ω is the set of (Φ, Θ). $\vec{e}_\Theta$ and $\vec{e}_\Phi$ are spherical unit vectors [2], [22]. The E-fields of the incoming TEM waves can be described as

$$\vec{E}_k(\Theta, \Phi) = E_{\Theta,k}(\Theta, \Phi)\vec{e}_\Theta + E_{\Phi,k}(\Theta, \Phi)\vec{e}_\Phi \quad (k \in 1, 2) \tag{3.1}$$

The E-fields are impinging from different spatial directions Ω and Ω' and are uncorrelated,

$$\begin{aligned} \mathscr{E}\{E_\Phi(\Omega)E_\Phi^*(\Omega')\} &= 0 \\ \mathscr{E}\{E_\Theta(\Omega)E_\Theta^*(\Omega')\} &= 0 \end{aligned} \tag{3.2}$$

where $\mathscr{E}\{\}$ indicates the expectation value and * the conjugate complex of a value. Also $E_\Phi(\Omega)$ and $E_\Theta(\Omega')$ are independent [39]

$$\mathscr{E}\{E_\Theta(\Omega)E_\Phi^*(\Omega')\} = 0 \tag{3.3}$$

The complex E-field antenna pattern for the two antennas ($\vec{F}_1(\Omega)$ and $\vec{F}_2(\Omega)$) consist of Θ and Φ polarized parts (3.4)

$$\vec{F}_k(\Theta, \Phi) = F_{\Theta,k}(\Theta, \Phi)\vec{e}_\Theta + F_{\Phi,k}(\Theta, \Phi)\vec{e}_\Phi \quad (k \in 1, 2) \tag{3.4}$$

When the antenna pattern are measured one after the other, the distances between the test antenna and the antenna to be measured must not be changed, as well as the position of the antenna to be measured must not be changed. This is the *conditio sine qua non* that the antenna patterns have the same phase reference [22] and that the

antenna patterns are correct with respect to each other.

The observed signals at the antenna ports V_1 and V_2 result from the incident field $\vec{E}(\Omega)$ on the antenna with its complex antenna E-field pattern $\vec{F}_1(\Omega)$ and $\vec{F}_2(\Omega)$ [39]. The proportionality constants C_1 and C_2 are dependent on the impedance provided at the corresponding antenna port.

$$V_1 = C_1 \oint \vec{F}_1(\Omega)\vec{E}(\Omega)\ d\Omega \tag{3.5}$$

$$V_2 = C_2 \oint \vec{F}_2(\Omega)\vec{E}(\Omega)\ d\Omega \tag{3.6}$$

Every impinging E-field coming from a certain spatial direction Ω is received with the antenna gain for this Ω. The spherical integrand $d\Omega$ is shown in (2.25). Doppler shift and movement of the antennas are neglected.

The cross polarization rate (XPR) is defined as

$$XPR = P_\Theta/P_\Phi. \tag{3.7}$$

P_Θ and P_Φ are the mean received powers in Θ and Φ polarizations over all possible positions in Ω.

Calculating the cross correlation of the received signal V_1 and V_2 by applying (3.2), (3.3), (3.5), (3.6) and (3.7) leads to

$$R_{12} = \mathscr{E}\{V_1 V_2^*\} = KP_\Phi \oint \text{XPR}\ F_{\Theta 1}(\Omega)F_{\Theta 2}^*(\Omega)\ pdf_\Theta(\Omega) + F_{\Phi 1}(\Omega)F_{\Phi 2}^*(\Omega)\ pdf_\Phi(\Omega)\ d\Omega \tag{3.8}$$

The angular power density functions of the incoming electromagnetic waves are described with $pdf_\Theta(\Theta,\Phi)$ and $pdf_\Phi(\Theta,\Phi)$, K is a proportionality constant. They fulfill the property

$$\oint pdf_\Theta(\Theta,\Phi)\ d\Omega = \oint pdf_\Phi(\Theta,\Phi)\ d\Omega = 1 \tag{3.9}$$

Assuming that the incoming signals $V_m\{m \in 1,2\}$ are Gaussian distributed and have zero mean value, their variances are

$$\sigma_m^2 = \mathscr{E}\{V_m V_m^*\} =$$

$$P_\Phi \oint \text{XPR } F_{\Theta,m}(\Omega)\, F_{\Theta,m}^*\, \text{pdf}_\Theta(\Omega) + F_{\Phi,m}(\Omega)\, F_{\Phi,m}^*\, \text{pdf}_\Phi(\Omega)\, d\Omega \qquad (m \in \{1,2\})$$

$$(3.10)$$

The *Envelope Correlation Coefficient* (ECC) ρ_e is now calculated by the squared absolute cross correlation of the received signals (3.5) and (3.6) divided by the product of their variances (3.11) [22].

$$\rho_e \cong \frac{|R_{12}|^2}{\sigma_1^2 \sigma_2^2} \qquad (3.11)$$

Measuring and calculating ρ_e using the electric fields requires lots of measurement effort. The antenna system has to be measured over an entire sphere surface, as the closed integral $\oint d\Omega$ over the spherical surface in (3.8) and (3.10) indicate. This takes time, because the test antennas have to be moved to the correct position in the anechoic chamber.

Salonen et al found a simplified method [40]. They use the reciprocity of antennas and found an equivalence between the complex E-field pattern and the S-parameters of the antenna system under certain circumstances. This leads to (3.12), ρ_e can be calculated by means of the scattering parameters of the antenna system [41]

$$\rho_e = \frac{|S_{11}^* S_{12} + S_{21}^* S_{22}|^2}{(1 - (|S_{11}|^2 + |S_{21}|^2))(1 - (|S_{22}|^2 + |S_{12}|^2))} \qquad (3.12)$$

No test antenna placement procedure is necessary, only the S-parameters have to be measured once. Within certain limitations this simplified formula delivers good comparison possibilities between antenna systems [41]:

- Antennas are assumed to be lossless.

- If omnidirectional source distribution can be assumed for the incident waves on the antenna system in the used environment, the usage of the S-parameter method to calculate ρ_e [42] is acceptable. However, measurements have shown that there are no major differences between ideal and real environments [43]. Especially for indoor environments this scenario is a good approximation [38].

(a) Coupling structure and connection   (b) Dipole and transformer
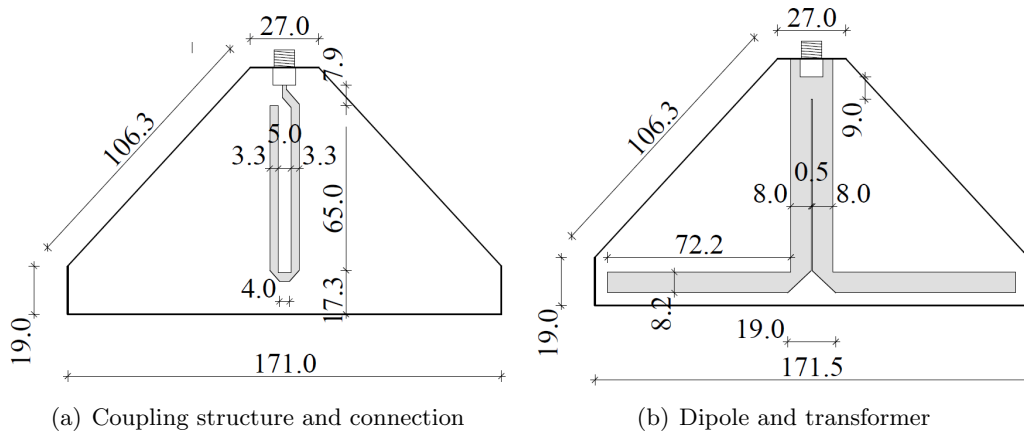
FIGURE 3.1: Reference Antenna for Band 13 (front and back side)

- The antenna ports termination of the not measured antenna is equal to a characteristic impedance of the employed vector network analyzer (VNA). A commonly used value for this impedance is $50\,\Omega$ [44]. In practice, the RF front ends do not always match this condition, nevertheless this evaluation method is commonly accepted [41, 45, 46].

3.3 Reference Antennas and Setup

The author investigates a practical antenna system containing two reference antennas for LTE band 13. The coupling of the antenna system has been simulated and measured. Antenna parameters are presented by simulation results.

The antenna itself is manufactured on a printed circuit board with Rogers 4350B substrate characterized by a dielectric constant $\epsilon_{\mathrm{r}} = 3.48$. It is designed for the LTE Band 13, with downlink frequency range from $746\,\mathrm{MHz}$ to $756\,\mathrm{MHz}$, and uplink range from $777\,\mathrm{MHz}$ to $787\,\mathrm{MHz}$.

The utilized antenna system consists of two single antennas. Figure 3.4(b) shows the simulated setup, while Fig. 3.8(b) shows the real setup. Each antenna is composed of a dipole and a $\lambda/4$ transformer located on one side of the printed circuit board (PCB) (Fig. 3.1(b)). On the other side a coupling structure is placed (Fig. 3.1(a)). It also serves as a BALUN (*Balanced Unbalanced Transformer*) and minimizes the influence of the connected cable. The directivity of a single antenna is depicted in Fig. 3.2 (Θ polarization) and Fig. 3.3 (Φ polarization).
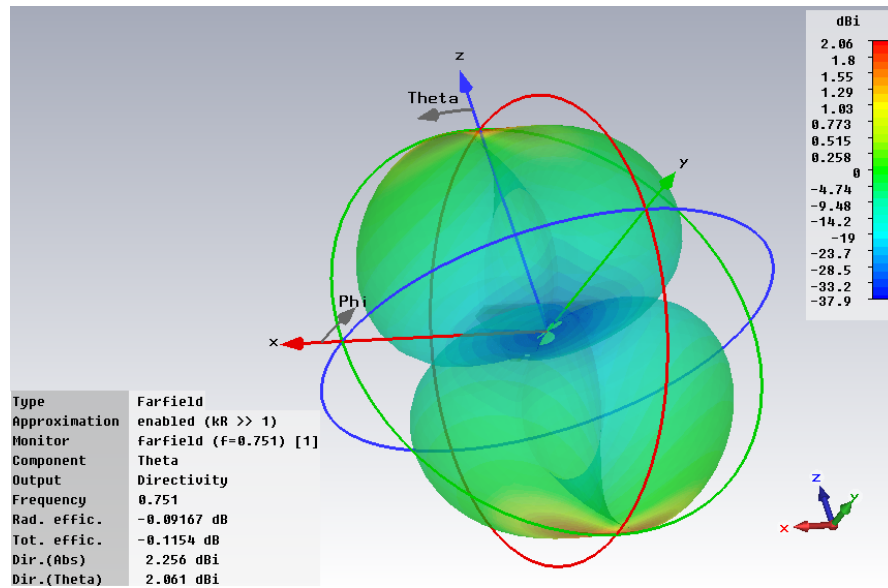
FIGURE 3.2: Directivity of single antenna in Θ polarization
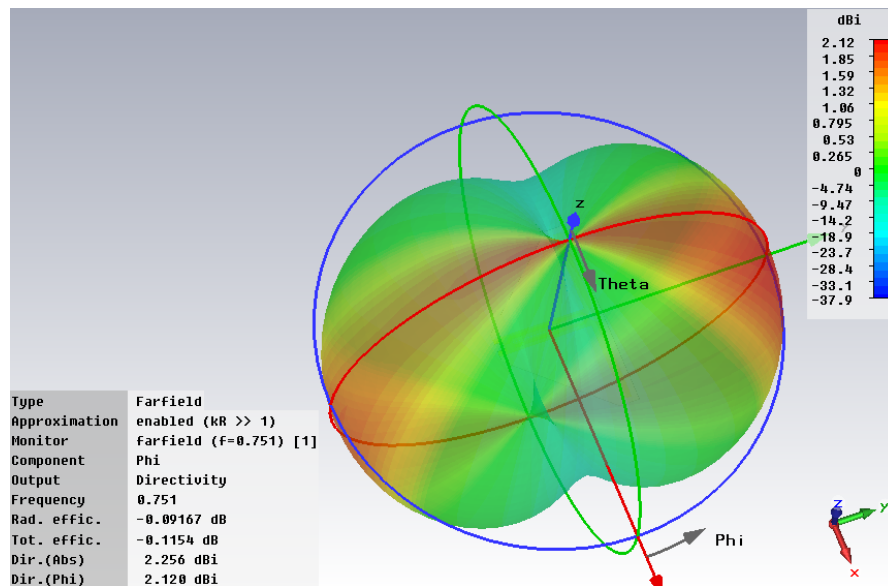
FIGURE 3.3: Directivity of single antenna in Φ polarization

The antenna system is placed with a polystyrene stand (Fig. 3.8(b)), with placing slots for changing the distance between the antennas. Polystyrene has a dielectric constant ϵ_r close to one, and almost does not influence the measurements. All measurements were accomplished in an shielded anechoic chamber, to avoid influence of laboratory facilities and equipment.

(a) Measurement setup of antenna group   (b) Simulation setup of antenna group
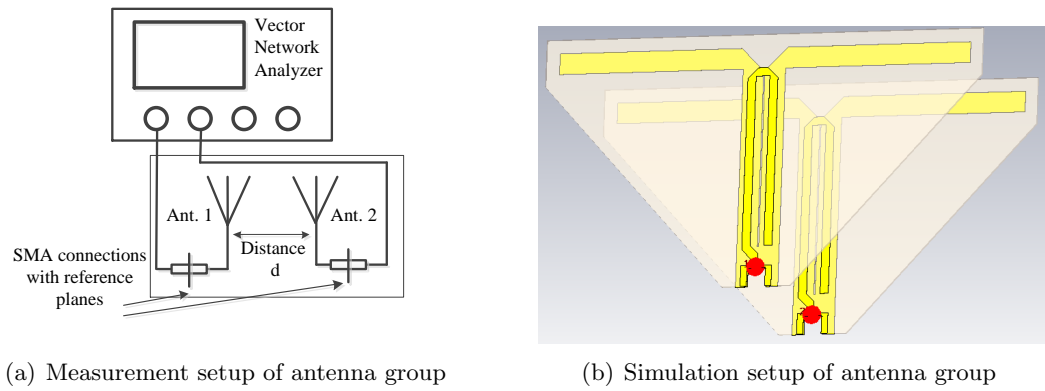
FIGURE 3.4: Measurement and Simulation Setup

3.4 Investigations

A parallel antenna setup is chosen for the antenna stand setup (Fig. 3.4(b), Fig. 3.8(b)), because the highest possible coupling of the antennas is expected in this case. The used distances between the antenna elements are 20 mm, 40 mm, 60 mm, 80 mm, 100 mm, 200 mm and 300 mm. Both antennas have the same orientation with the dipoles aligned in the same direction. This thesis determines the ECC ρ_e using both the measured and the simulated S-parameter according to (3.12).

3.4.1 Simulations

The author simulates the antenna systems in *CST Microwave Studio*. In the simulations, the antennas have are placed in air with a dielectric constant $\epsilon_r = 1$ (Fig. 3.4(b)).

3.4.2 Measurements

The S-parameters of the reference antennas are measured using coaxial cable connections between antenna elements and the ports of the VNA. Calibration of the measurement setup was accomplished up to the male *sub-miniature version A* (SMA) connectors of the connection cables, as the principle measurement depicts in Fig. 3.4(a).

(a) $d = 20mm$ (b) $d = 100mm$
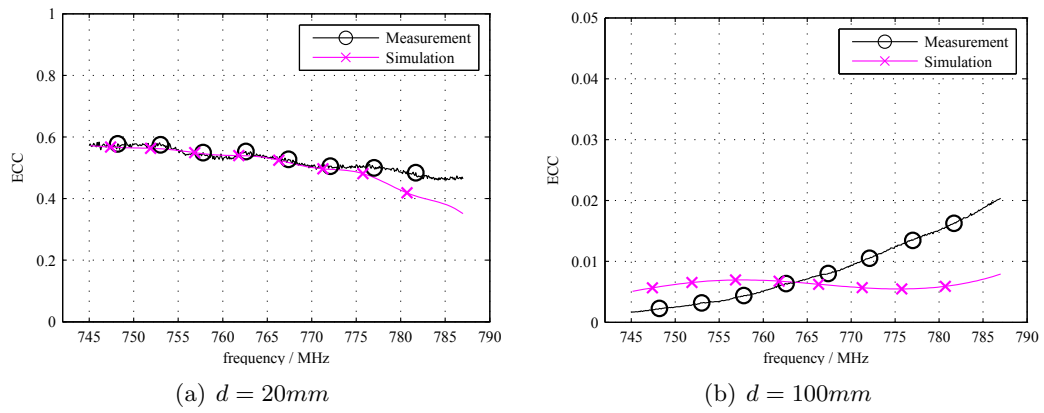
FIGURE 3.5: Comparison ρ_e of measurement and simulation

(a) $d = 40mm$ (b) $d = 200mm$
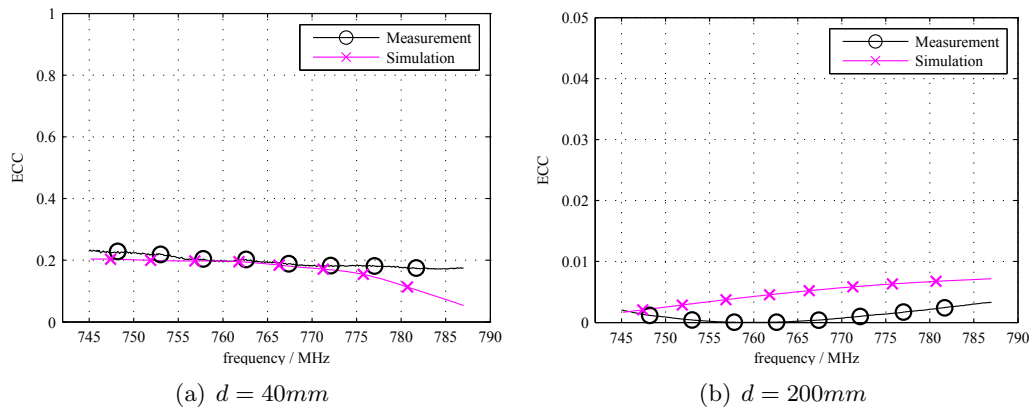
FIGURE 3.6: Comparison ρ_e of measurement and simulation

(a) $d = 60mm$ (b) $d = 300mm$

FIGURE 3.7: Comparison ρ_e of measurement and simulation

(a) ECC ρ_e vs. distance at 766 MHz

(b) Setup for the measurement of the antenna system
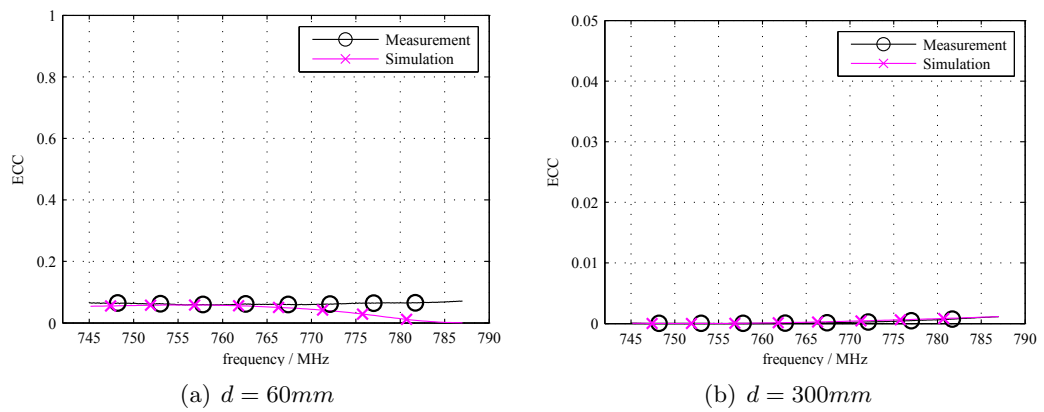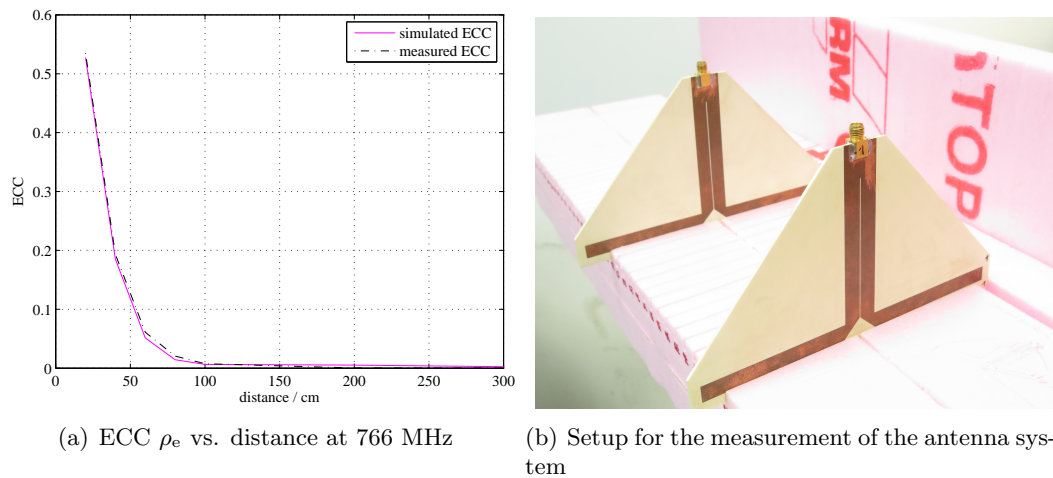
FIGURE 3.8: Comparison ρ_e versus distance / physical setup

3.4.3 Comparison of Simulated and Measured Results

The result graphs exhibit two different scalings. The diagrams for 20 mm (Fig. 3.5(a)), 40 mm (Fig. 3.6(a)) and 60 mm (Fig. 3.7(a)) use the full possible ECC ρ_e scaling from zero to one. The diagrams for 100 mm (Fig. 3.5(b)), 200 mm (Fig. 3.6(b)) and 300 mm distance (Fig. 3.7(b)) employ a scaling from 0 to 0.05, representing the lowered ρ_e for bigger antenna distances d.

The results obtained in the investigations, both simulation and measurement, show a clear trend of a decreasing ECC ρ_e with increasing distance between the coupled antennas.

The influence of the distance between the antennas on the ECC ρ_e can be seen in Fig. 3.8(a) for 760 MHz. The bigger the distance between the antennas, the lower gets the ECC ρ_e.

As mentioned, the chosen S-parameter method for calculation of the ECC ρ_e is ascertained to give a fast estimation on the quality of a MIMO antenna system. There is good congruence between measurement and simulation results.

3.5 Conclusion on Chap. 3

This chapters presented a wrap up on the theory of the *Envelope Correlation Coefficient* (ECC). It is a good figure of merit for comparing coupled MIMO antenna systems. A single LTE reference antenna for Band 13 with its directivity pattern was indicated. A

system employing two of these antennas was investigated.

There are two possible ways of achieving the ECC ρ_e, the simpler one using S-parameters was chosen. The ECC is decreasing with increasing distance between the planar antennas. It was shown that simulations show a good accordance with simulation.

Chapter 4

Performance Tests of Entire Devices

4.1 Introduction

With the introduction of MIMO and receiver diversity wireless devices are expected to give large gains in downlink throughput performance. The rise of these gains is highly dependent on the performance of the receive-antenna system [9] and the receiving algorithm [47]. The devices can change the behaviour of the antenna systems, e.g. by using beamforming mechanisms [4]. They also can adapt software algorithms to suit the environment they are currently used in. The radiated performance is also a function of the device usage circumstances and position [47], which has to be considered in the adaptation.

The wireless equipment manufacturers as well as the network providers are pushing to have performance tests of the devices available at hand. The network providers want to recommend the UEs with the best performance to their customers, the manufacturers want to be able to rate the quality of their own UE to the one of the competitor. Both want to have the ability to do easily applicable comparisons between the different devices. UEs have to work properly in many different environments with changing parameters, e.g. a user is viewing a video stream in a car that is moving from the country side to the city center. During the ride the wireless channel completely changes its behavior, the speed of the car is changing, the holding position of the UE is changed by the user, to

name a few. It is not practical to test the user equipment in this wide range of available real world scenarios. Hence, these real world cases have to be modeled for the use with test equipment. The worldwide consortium *3rd Generation Partnership Project* (3GPP) has taken over responsibility of selecting one or two adequate test methods. Also other institutions have taken efforts to investigate this topic: *COST2100* (European Cooperation in Science and Technology), *COST IC1004* and *CTIA* (*The Wireless Association*, formerly called *Cellular Telecommunications and Internet Association*).

"*The scope [...] is to define a [...] methodology or set of comparable methodologies for measuring the radiated performance of multiple antenna reception and MIMO receivers in the UE (*user equipment*). The test methodology should be relevant for* High Speed Package Access *(HSPA) and* Long Term Evolution *(LTE) .*" [9]

These methods must be able to [9]

- verify the radiated *Over-The-Air* (OTA) performance of the device

- accurately reflect MIMO and SIMO performance of the device under realistic MIMO and SIMO channel conditions. They shall be able to distinguish between UE of "good" and "bad" receive OTA performance, and offer a good estimation of a likely user experience in the field.

- offer good reliability, repeatability and an acceptable level of measurement uncertainty.

The test methodologies have to enable performance verifications for [9]

- handheld devices, devices embedded in laptop computers, and other devices such as *Machine-to-Machine* (M2M) equipment;

- all transmission modes used in LTE and HSDPA, including spatial multiplexing (MIMO) and single spatial layer operation;

- initially the tests should use LTE transmission mode 3 (spatial multiplexing), *Fixed Reference Channels* (FRC), and forced rank 2 (2×2 MIMO system). As the test methods progress, other modes shall be introduced.

All test methods, except two, employ one setup and one measurement principle for the performance tests. These two test methods, namely the the *Two-Stage Method* and the

Decomposition Method, split the tests and utilize more setups and measurements. This chapter reveals the basic principles of all methods.

In order to compare results across different methods, the *absolute throughput* is used as figure of merit. The investigations in this thesis will use the *relative throughput*, due to its proportonality to the absolute throughput, its generality and indepence of certain FRCs. Result curves will be presented as throughput y versus downlink power P_{downlink} $(P_{\text{downlink}}(y))$.

The tests should include the performance of the entire wireless device, including MIMO antenna systems, analog frontends, mixers, receiving algorithms, switching of modulation and coding scheme, to name a few.

This chapter gives an overview of the proposed test methods divided into two groups, which differ a lot from each other, namely

- anechoic chamber tests

- reverberation chamber tests

Anechoic chambers ideally do not have reflections, as the inside walls are covered with material that absorbs all electromagnetic waves. They have metallic walls, no radiation from outside is impinging on devices placed in it.

The *reverberation chamber* is the complete opposite, it is made of metal walls, does not contain anechoic material and is highly reflective. These two groups represent two ends of a broad spectrum of environmental conditions for wireless device testing. Most of the real world environments lie somewhere in between these two extremes. Fig. 2.1 illustrates such a situation encountered by the mobile device. Reflections from scatterers arrive under different angles, angular spread and time delay, as well as LOS (*Line Of Sight*) connections are possible.

The question arises, which features have to be implemented to approximate these reality scenarios. Additionally the test system should support phantom heads and hands to simulate the way of the mobile usage and the provoked near field effects on the UE [47]. All performance tests deliver throughput y versus downlink power P_{downlink} curves as the result $(P_{\text{downlink}}(y))$.

Both groups, anechoic chamber methods and reverberation chamber methods, have their advantages and drawbacks, which will be discussed. The setup of the measurement system, the emulation of the wireless transmission channel, the generation of the EM-fields

impinging on the UE antennas and the generation of the results will be included in the follow discussion below. One of these methods, a yet very promising one, will be investigated further in this thesis.

4.2 Test Methods Using Anechoic Chambers

The following methods have in common that they employ anechoic chambers. An anechoic chamber is a metal cavity with absorber material on its inside walls. No radiation is entering or leaving the cell and all radiation emitted by the mobile device placed in the cell is absorbed. Ideally nothing is reflected. For downlink tests, the electromagnetic wave is emitted by the test antennas and is received by the UE antennas, the different test methods have differing approaches to make use of this circumstance to implement the test scenarios.

The quiet zone of an anechoic chamber is specified certain volume, where the reflections coming from walls of the chamber and equipment placed in the chamber, are below a certain value [48]. In this volume the Device Under Test (DUT) has to be placed for evaluation [49].

4.2.1 Multi-Probe Method

The Multi-Probe Method uses the fact that desired EM fields in the quiet zone can be synthesized by several EM waves. This principle allows the fast generation of EM waves impinging on the UE to be tested. This method executes all performance tests, faded and static, at once.

Figure 4.1(a) shows the principle of the antenna setups for the Multi-Probe Method. They are arranged on a horizontal circle (azimuth plane), while the UE is placed in the center of this circle. Figure 4.1(b) shows a horizontal alignment with eight test antennas seen from above, the quiet zone is around the center of the antenna ring. All these circulary placed antennas generate EM fields that lead to a superposition of fields in the quiet zone, resulting in the desired test field. A practical realization of the Multi-Probe Method employing 16 dual polarized antennas can be seen in Fig. 4.2(a).

As the block diagram of the measurement system in Fig. 4.3 reveals, the signals of the
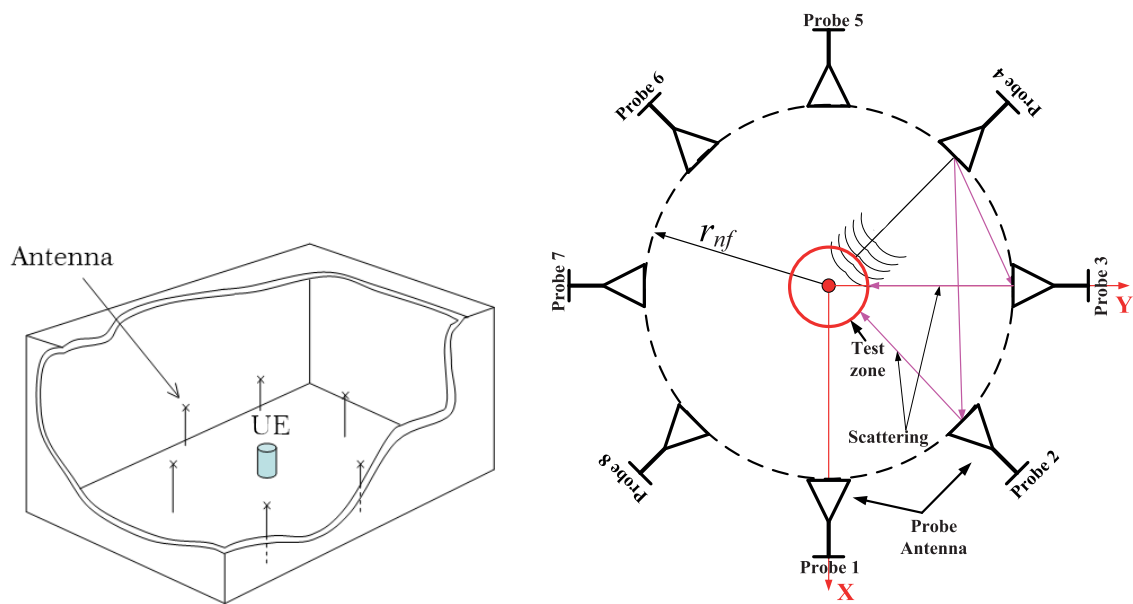
(a) principle setup of Multi-Probe Method in ane-
choic chamber [9]

(b) Multi-Probe setup with eight antennas [50]

FIGURE 4.1: Multi-Probe Method Setup (I)
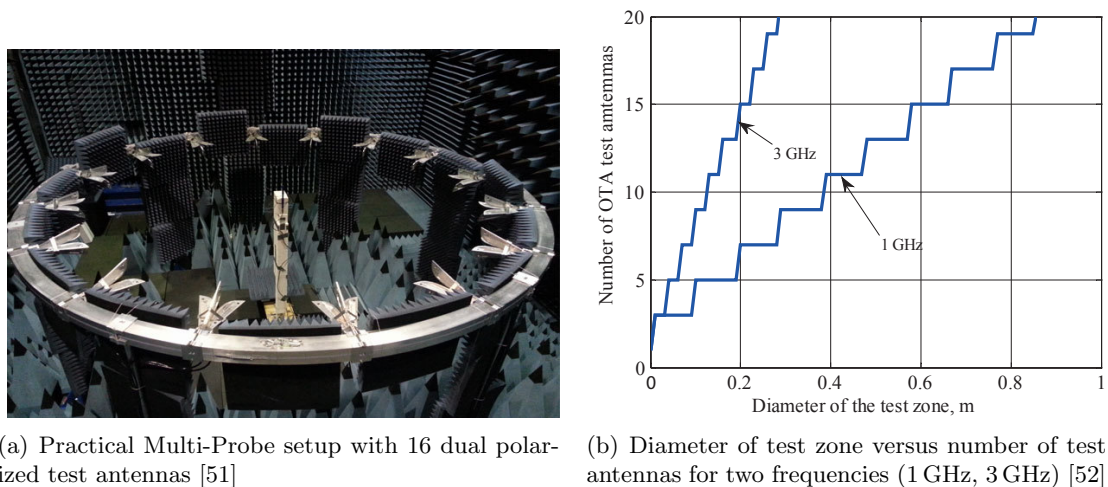
(a) Practical Multi-Probe setup with 16 dual polar-
ized test antennas [51]

(b) Diameter of test zone versus number of test
antennas for two frequencies (1 GHz, 3 GHz) [52]

FIGURE 4.2: Multi-Probe Method Setup (II) and Number of Necessary Antennas

radio communication tester [9] (base station emulator) are treated in a spatial channel
emulator. The channel emulator changes the signals in a way as if they would pass
through a certain wireless propagation channel. After amplification they pass the cali-
bration unit, where corrections are done to compensate phase and amplitude differences
for all antennas. Finally the test antennas are fed with this signal. The user equipment
receives the incoming signals and delivers its feedback to the base station emulator.

A central computer is used for placement of the UE (UE motion controller) and for data
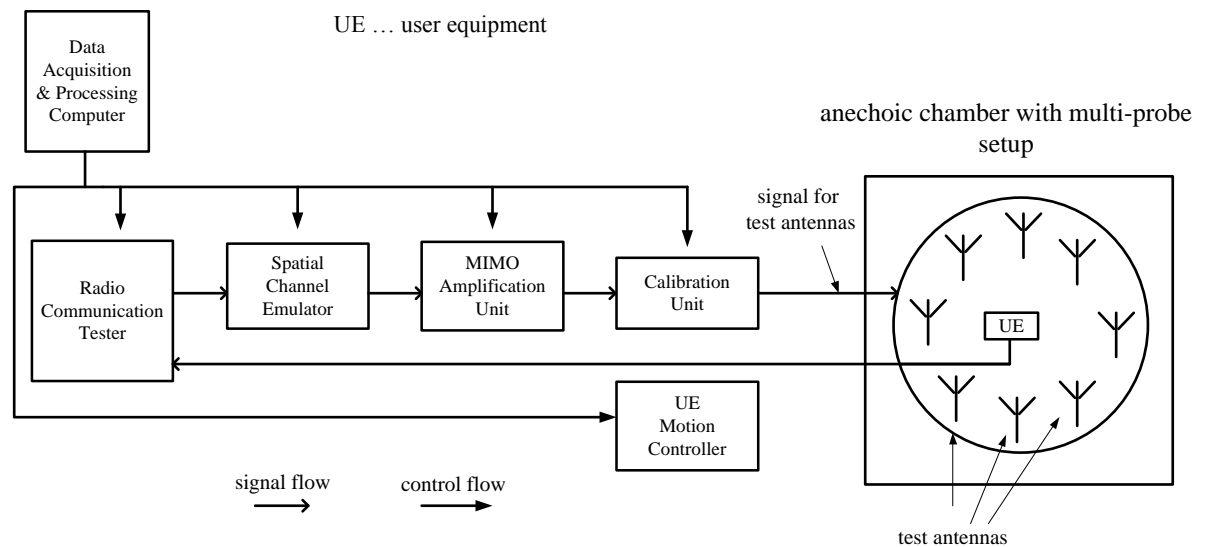
FIGURE 4.3: Block diagram of Multi-Probe measurement setup [3]

acquisition and processing. This method is well described [53–56] and allows very fast reproduction of a desired test field. Nevertheless, it requires lots of equipment, including a high number of antennas, many amplifiers and calibration equipment.

The effort for calibration is high [50], due to necessary the knowledge of amplitude and phase of the measurement system including all test antennas. The setup is sensible to mechanical changes. An operator has to vary the functionality of the UE very carefully not touching the test antennas at all. Otherwise the results will be incorrect and recalibrations have to be done.

The size of the quiet zone is depending on the test frequency and on the number of test antennas, as shown in Fig. 4.2(b). Generally, the higher the number of test antennas, the bigger is the quiet zone. With higher frequencies more test antennas are needed for the same test zone radius. E.g. for a diameter of 20 cm it is necessary to use at least 7 test antennas for a frequency of 1 GHz, but a minimum of 15(!) are needed for 3 GHz, as shown in [52]. The higher the number of antennas, the higher the effort in the amplification and calibration unit. The method employing one antenna ring is only capable of reproducing fields in a 2D plane, which does not reflect a realistic scenario. The method can be extended with UE roll positioners, which turn the UE in an azimuth plane, and a second antenna ring. Still, it cannot cover many existing possibilities for three dimensional impinging E-fields.

4.2.2 Two-Stage Method

The *Two-Stage Method* measures the UE antenna patterns in the first stage and employs these patterns in the channel emulator to emulate appropriate antenna voltages with the help of the base station emulator in the second stage. The block diagram is depicted in Fig. 4.4.
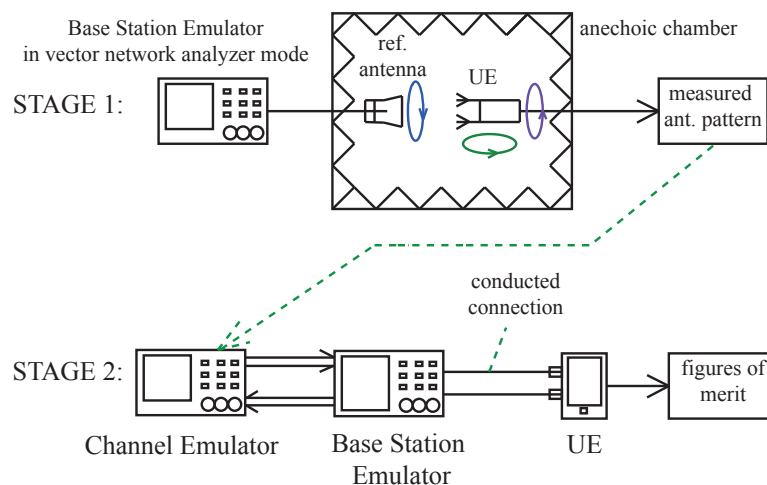
FIGURE 4.4: Block diagram of the Two-Stage setup employing an anechoic chamber with a UE positioner and a reference antenna, a base station emulator and a channel emulator [4]

The setup of the first stage consists of a classical antenna measurement in an anechoic chamber. The base station emulator is in vector network analyzer mode, the UE antennas are connected to it. For a three dimensional measurement, the reference antenna can be placed in zenith angle and the UE can be placed in azimuth angle. A *roll positioner* allows additional positions of the UE for the measurements [57].

The setup of the second stage consists of the UE connected to the base station emulator that is using the channel emulator. The connection is a conducted one. The channel emulator provides calculations so that the base station emulator can provide adequate conducted test signals, as if these test signals from the base station were received by the antennas of the UE.

The advantage of the *Two-Stage Method* is that an anechoic chamber is only necessary for the antenna pattern measurements of the first stage. The antenna patterns are measured in gain and phase. The measurements of the second stage can be done in a normal laboratory environment.

The UE has to be able to deliver the necessary figures of merit, like throughput versus downlink power. The rank of the MIMO transmission can easily be changed to higher

orders than 2×2, if the base station emulator and the channel emulator are capable of these modes. Stage 1 requires a classic anechoic chamber with one test antenna, which is also called reference antenna by the inventors of the method. Anechoic chamber usage time is a scarce resource, the chamber will be less loaded as with other methods. Additionally, already existing chambers do not have to be upgraded. This classical anechoic chamber setup using one test antenna are also called *Single-Input Single-Output* (SISO) test systems. The first stage antenna pattern measurements can also be done wireless, if the UE possesses an antenna pattern measurement mode.

A disadvantage of the method is that self desensitization of the UE is not recognized anymore at the second stage, if conducted connections are used. In self desensitization the transmitter jams its own receiver. A possible solution to this problem is to use radiated connections in the second stage. This would require two or more test antennas, according to the order of the MIMO transmission scheme. It is necessary to convolve the inverse of transmission matrix of the chamber $\mathbf{H}_c$ with the matrix of the fading channels $\mathbf{H}_{ch}$ to cancel effects of crosstalk between the antennas. This behavior of the canceled crosstalk is reflected in $\tilde{\mathbf{H}}_{ch}$,

$$\tilde{\mathbf{H}}_{ch} = \mathbf{H}_c^{-1} * \mathbf{H}_{ch} \tag{4.1}$$

where $*$ denotes the convolution. The former advantage of saving anechoic chamber usage time is lost, if a wireless connection is used in the second stage.

These radiated connections in the second stage are an update to the current specification [9], they are investigated in [58] and [59]. Operator handling is not too challenging, except the placement of the UE during the antenna pattern measurements. Calibration effort is low, as few critical connections are used.

4.2.3   Decomposition Method

4.2.3.1   Introduction

The Decomposition Method [5], [60] maps the "real world" test scenario (Fig. 4.5) in a *conducted* and a *radiated* setup. The "real world" scenario consists of a transmission chain from the base station to base station antenna system over the "real world" wireless propagation channel to the UE receive (RX) antennas. This scenario is split into two different measurement setups, which speeds up the measurement by a factor of 36 (see

Chap. 4.2.4). These split setups deliver different measurement results that are used as a basis for calculating the overall performance result of the UE. The UE delivers feedback to the BSE regarding the received data during all the measurement procedures, the BSE calculates the throughput over downlink power curves with this information.

The author explains this method more in detail, therefore he uses sub-sections in this chapter. Nevertheless, the structure itself is similar to the descriptions of the other methods.

4.2.3.2   Radiated and Conducted Setup

The conducted setup consists of the BSE with a connected channel emulator transmitting to the UE by wired connections. The conducted setup can include fading ("Channel" measurements) or have no fading (static "Baseline" measurements). Figure 4.6(a) exhibits the conducted setup using fading for the "Channel" measurements. The measurements employing the conducted setup can be done in normal laboratory environment and do not require an anechoic chamber. Figure 4.6(b) depicts the conducted static (without fading) measurement setup for "Baseline" tests. The "Baseline" performance measurement will deliver the lowest possible dowlink power values for a certain throughput. It is the performance limit measurement of the UE due to its unfaded conducted connection.

The radiated setup (Fig. 4.7) employs the *Two-Channel-Method* for the radiated tests, also called *Over-The-Air* (OTA) tests [61]. It employs an anechoic chamber with two test antennas that are positionable in a Θ-plane, a turntable for UE placement that is turnable in the Φ-plane, as exhibited in Fig. 4.8(a). The UE is placed in the center of the quiet zone. The test antennas always have a constant distance to the UE and they are fed with signals from the BSE. The name Two-Channel-Method comes from the two downlink channels towards the UE enabled by the two test antennas. The radiated setup is static and does not contain any fading, it is mainly used for antenna performance tests. The UE behavior on faded channels is not included in the static radiated tests.
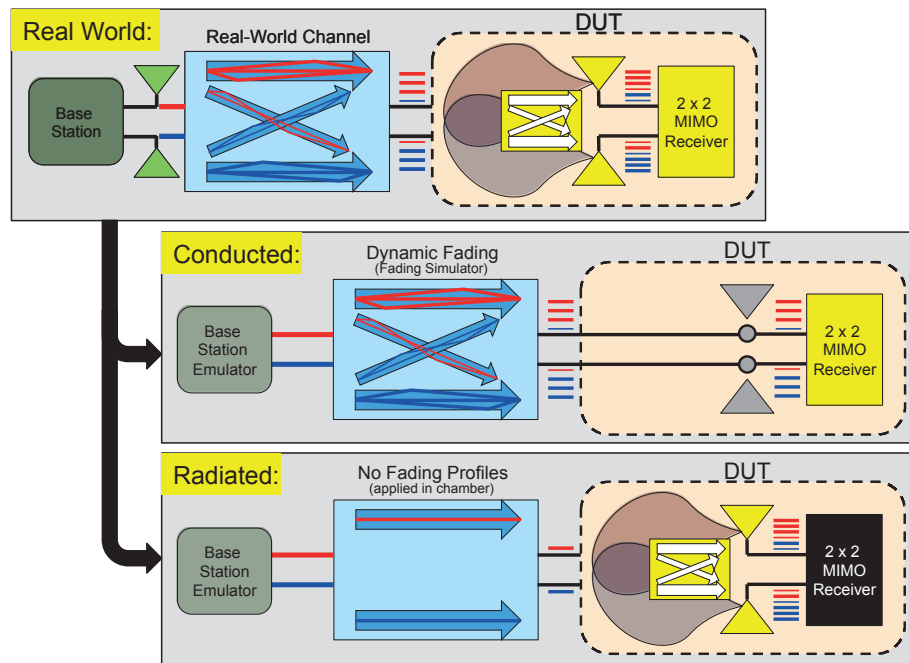
FIGURE 4.5: Block diagram of Decomposition Method - downlink case for a 2×2 MIMO system [5]

(a) Conducted faded measurement setup – „Channel" Measurement

(b) Conducted unfaded measurement setup (static) – „Baseline" measurement
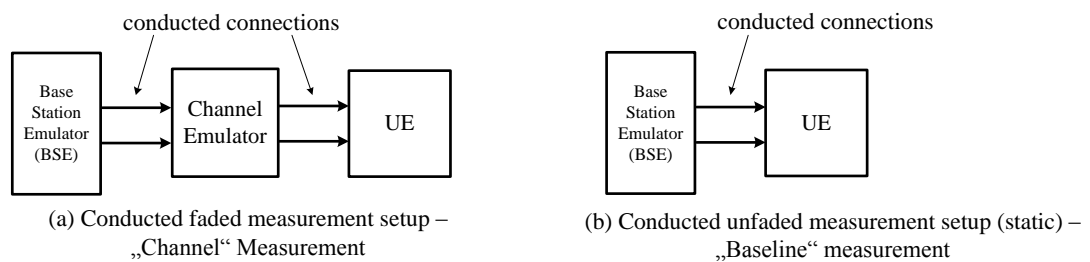
FIGURE 4.6: Measurement setup for conducted measurements employing BSE, channel emulator, UE and wired connections

4.2.3.3 Generation of Fields and Emulation of the Channel Propagation Conditions

The two test antennas generate the EM field impinging on the UE for the radiated tests. The polarizations of the test antennas can be switched independently between vertical (Θ) and horizontal (Φ) polarization.

The wireless propagation channel is emulated by a channel emulator. The emulator changes the signals in a way a physical wireless propagation channel would do it, including multipath propagation (frequency dependent channels) and Doppler effects. When
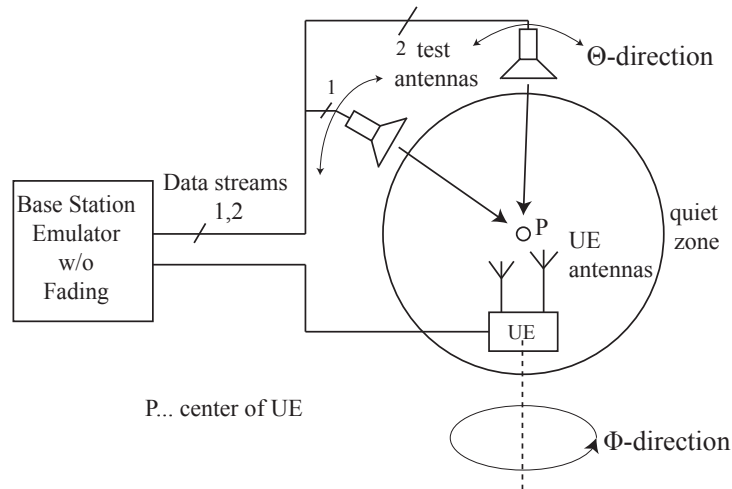
FIGURE 4.7: Measurement setup employing Two-Channel Method for the static radiated tests of the Decomposition Method; BSE without channel emulator [6]

(a) Rotation planes of test antenna and device under test in the anechoic chamber[61]

(b) Setup Example - test horn antennas and laptop as device under test in the anechoic chamber [61]
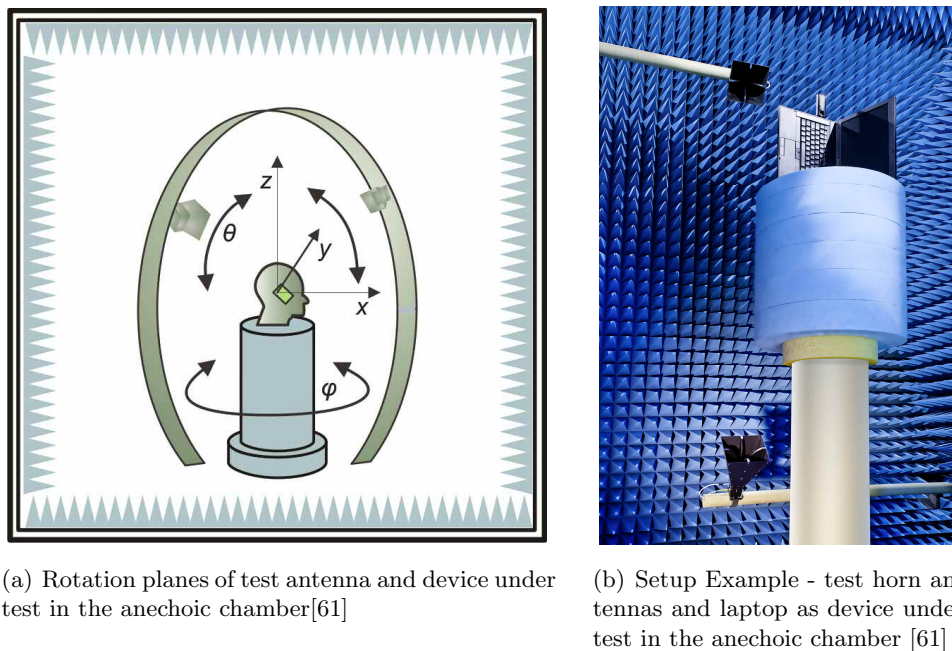
FIGURE 4.8: Test system setup - theoretical and practical

this thesis talks about fading and faded channels, it means all effects a wireless channel is incorporating.

4.2.4 The Split of the Measurements

The Decomposition Method requires performance test results of the UE in different setups (Fig. 4.6, Fig. 4.7):

- conducted connection between base station emulator, channel emulator and UE

- radiated connection between base station emulator and UE

The "Baseline" measurement (unfaded conducted measurement) is the simplest possible measurement, because the user equipment is connected to the base station emulator by two coaxial cables, the channel matrix **H** is an identity matrix. It is depicted in Fig. 4.6(b)). It exhibits the best performance the device can ever achieve, it is only limited by the intrinsic UE noise. The result of the "Baseline" measurement is the downlink power at a certain throughput $P_{bl}(y)$.

The faded conducted measurements (Fig. 4.5 - conducted; Fig. 4.6(a)) are also executed in conducted mode. This time the signal is dynamically faded, Doppler shifts and spreads can be applied. These tests are also called "Channel" measurements or simulations. The ability of the device to cope with these circumstances without the UE antenna system influence is tested. The devices performance will be degraded in comparison the "Baseline" test. The conducted faded result is $P_{ch}(y)$, where the subscript $_{ch}$ reflects the "Channel"' measurement.

The unfaded radiated measurement (Fig. 4.5 - radiated), covered by the *Two-Channel Method* [61], checks the performance of the device antennas (including the receiving algorithms without its fading behaviour). They are also named "Antenna" tests. No fading is applied. The radiated coupling between test antennas and user equipment is exhibited in Fig. 4.8(a). The user has to choose a proper set of test antennas and device positions, so called *constellations*. These constellations also include the test antenna polarizations, that are used during the measurements (Chap. 4.2.4.2). The result of the measurement is $P_{ant}(y)$, where the subscript $_{ant}$ reflects the "Antenna"' measurement.

The "Overall" scenario (Fig. 4.5 - real world) with testing faded and radiated performance at once, is the ideal setup for measuring the UE, delivering exact results.

Using the "Overall" setup for a measurement of $N = 128$ constellations, takes the time t_{overall}. Measuring the UE's behavior on the channel with block fading takes the time $t_{\text{bf\_ch}}$, whether radiated for a single constellation or conducted. For the results of the static radiated "Antenna" results, it takes the time $t_{\text{ant,st}}$. An example with reasonable times from practical measurements is given:

$$t_{\text{overall}} = N \times t_{\text{bf\_ch}} = 128 \times 20 \text{ sec} = 2560 \text{ sec} \tag{4.2}$$

In comparison, if the measurements are split into conducted and radiated tests, the complete test time needed is t_{dc}

$$t_{dc} = 1 \times t_{bf\_ch} + N \times t_{ant,st} =$$
$$= 1 \times 20 \text{ sec} + 128 \times 0.4 \text{ sec} = 71.2 \text{ sec} \tag{4.3}$$

$$\text{Acceleration factor } a = \frac{2560 \text{ sec}}{71.2 \text{ sec}} \approx 36 \tag{4.4}$$

This is a acceleration of the measurements of a factor $a = 36$! Therefore measuring the "Overall" setup is impractical, and the Decomposition Method with its splitted measurements shows its strengths. The author uses the "Overall" results only for comparison to the Decomposition Method results.

In test data payload is organized in subframes, e. g. for the mobile communication standard *Long Term Evolution* (LTE). The times t_{dc} and $t_{overall}$ were measured with a data payload of 400 sub-frames for the static measurements and 20000 sub-frames for the faded measurements per single measurement or per constellation. This number of subframes guarantees that 95% of the results lie within a reasonable confidence interval. If the faded measurements require more sub-frames, the acceleration rate is even bigger then 36. This acceleration also reduces the anechoic chamber occupancy. The high side of the Decomposition Method is that faded measurements have to be done only once, resulting in the mentioned acceleration of test speed.

4.2.4.1 Calculating the Decomposition Results

To determine the overall performance curve of a UE using the Decomposition Method, the three above described measurements are necessary:

- conducted "Baseline" measurement $P_{bl}(y)$ (Fig. 4.9), (Fig. 4.10) and (Fig. 4.11)

- conducted faded "Channel" measurement $P_{ch}(y)$ (Fig. 4.9)

- radiated unfaded "Antenna" measurement $P_{ant}(y)$ (Fig. 4.10)

Fig. 4.9, Fig. 4.10 and Fig. 4.11 show the baseline measurement with the dashed line. This measurement mode exhibits the lowest possible downlink power level (DL). Fig. 4.10 shows radiated static device performance (red curve).
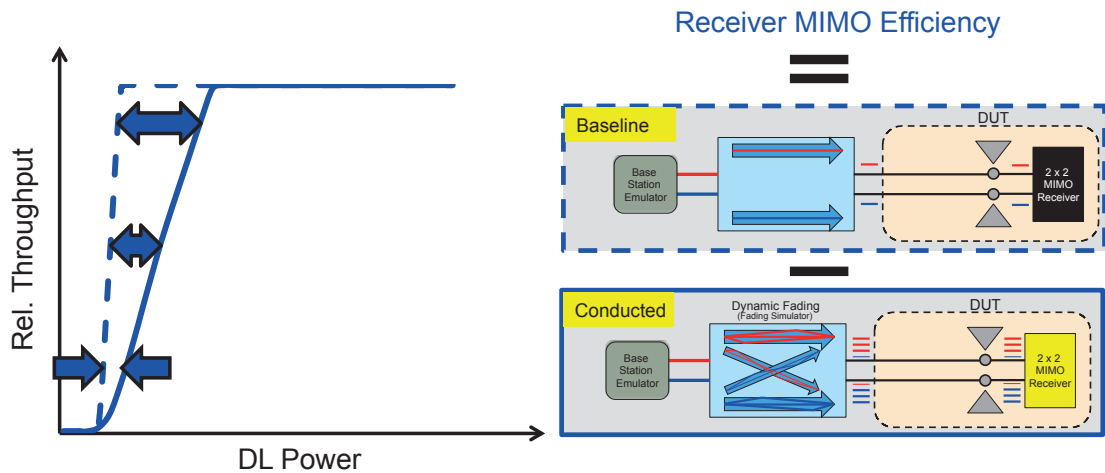
FIGURE 4.9: Receiver MIMO efficiency; "Baseline" (dashed line) and faded "Channel" measurement / rel. throughput vs. downlink (DL) power [5]
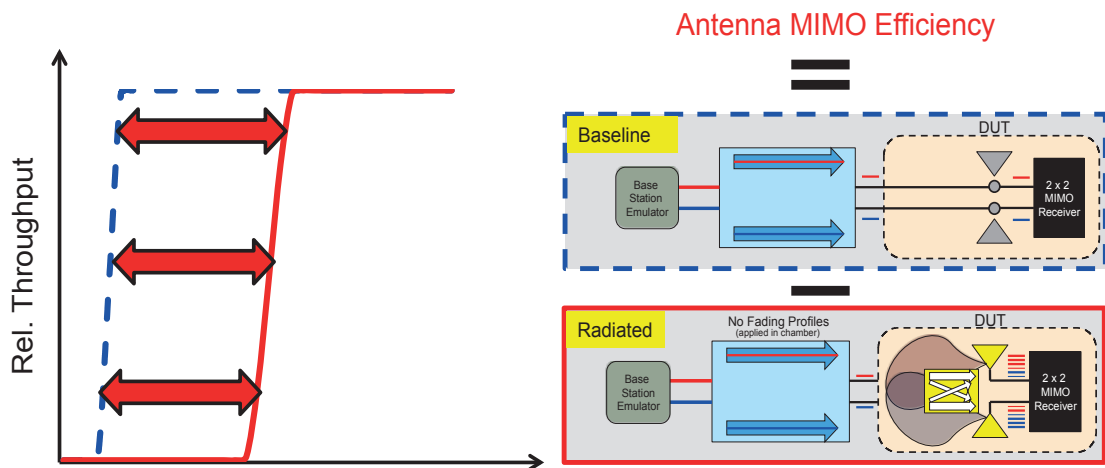
FIGURE 4.10: Antenna MIMO efficiency; "Baseline" (dashed line) and radiated un-faded "Antenna" measurement / rel. throughput vs. downlink (DL) power [5]

The faded conducted measurement curve (Fig. 4.9) is less steep than the baseline curve due to the stochastic distribution of the fading channel parameters.

As the user equipment antennas are closely spaced to each other, they add correlation to the transmitted data vectors of the investigated systems and subsequently degrade the performance of the transmission system, as the investigations in Chap. 7.4.1 exhibit. This performance degradation results in the "Antenna" measurement curve, which is a parallel right shifted version of the "Baseline" curve (Fig. 4.10).

Fig. 4.11 shows the result of the Decomposition Method [5]. Mathematically expressed,

the result $P_{dc}(y)$ is computed by

$$P_{dc}(y) = P_{ant}(y) \frac{P_{ch}(y)}{P_{bl}(y)} \tag{4.5}$$

If (4.5) is expressed with logarithmic values, it is consisting only of summations and subtractions, as applied in Fig. 4.11

$$P_{\text{dc,log}}(y) = P_{\text{ant,log}}(y) + P_{\text{ch,log}}(y) - P_{\text{bl,log}}(y) \tag{4.6}$$

Looking at Fig. 4.11, the logarithmic addition and subtraction can be seen.
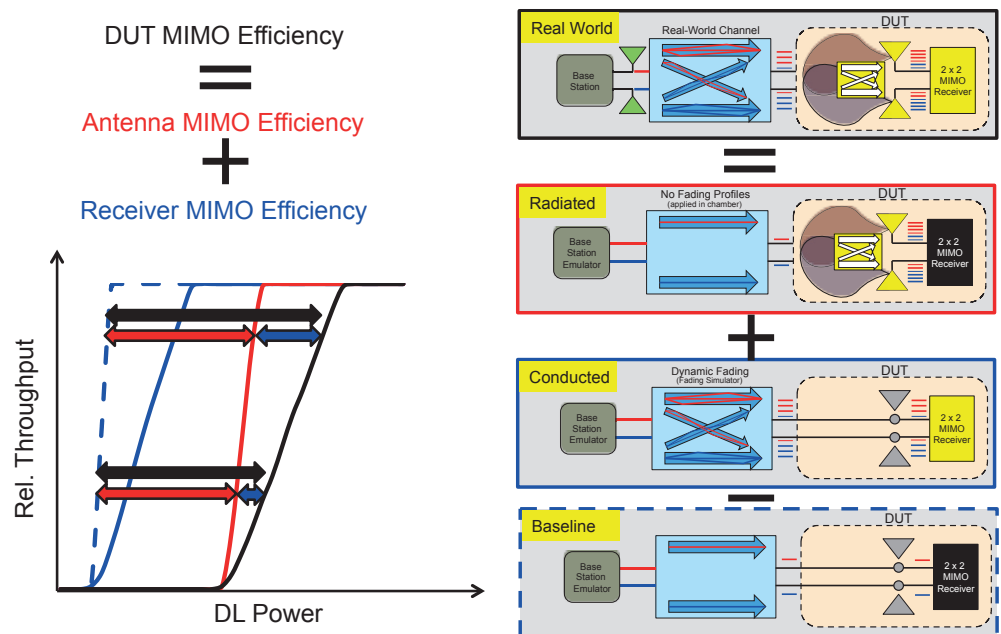
FIGURE 4.11: Combining the radiated unfaded and conducted faded
rel. throughput vs. downlink power curves [5]

The decomposition method result $P_{dc}(y)$ is ideally the same as the *real world scenario* result $P_{oa}(y)$.

$$P_{dc}(y) \overset{!}{=} P_{oa}(y) \tag{4.7}$$

4.2.4.2 Generation of the Constellations for Radiated Measurements

Complete performance tests of a UE afford positioning of the test antennas on the complete surface of a sphere. The test antenna and device positioners can cover this need almost completely. The positions of the test antennas including polarization and

the UE placement is a *constellation* [61]. Such a constellation contains the following information:

- Φ_1, Φ_2 - the azimuth angles of the UE placed on the turntable

- Θ_1, Θ_2 - the zenith angles of the test antennas

- the polarizations of the test antennas TA_1 and TA_2 (Θ and Φ polarization)

In spatial measurements of UEs, it is mandatory to measure the performance of the device over the complete surface of a sphere. If the angles Φ_1, Φ_2, Θ_1 and Θ_2 cover the whole sphere surface and follow a uniform distribution, they will cause over-sampling at the poles and probable under-sampling at the equator of the measurement sphere. To avoid such effects a different distribution of the angles has to be chosen.

One possible way is to calculate the angle Φ_1, Φ_2 deterministically using the *Golden Angle*. This angle can be observed in the circular distribution of leaves of a plant, in order to maximize its exposure to sunlight [62]. It is shown considerably in Fig. 4.12. The Golden Angle of 137.508^o is multiplied with the actual constellation number n,

$$\Phi_\mu = n \ 137.508^o \div 360^o \qquad \{\mu \in 1, 2\}, \quad \{n \in 1, ..., N\} \tag{4.8}$$

where $\div$ is the modulo division, N is the total number of constellations, μ is the number of the test antenna. The usage of the "Golden Angle" in the azimuth plane has the advantage that a rise of the total constellation number N does not change the distribution of Φ_1, Φ_2, which are independent and identically distributed (IDD). Figure 4.13 depicts this behavior.

For the distribution of the zenith angles Θ_1, Θ_2 a sine shaped uniform distribution is employed, as depicted in Fig. 4.13. The sine shaped distribution of the angles provides a uniform distribution of the measurement constellations regarding the sphere surface [8].

The polarizations of the test antennas are also IID. A practical applicable set of constellations that fulfills the mentioned properties, possesses a constellation count of $N = 128$ [8]. The set of Φ_1, Φ_2, Θ_1 and Θ_2 as well as the test antenna polarizations for $N = 128$ are shown in Fig. 4.14.
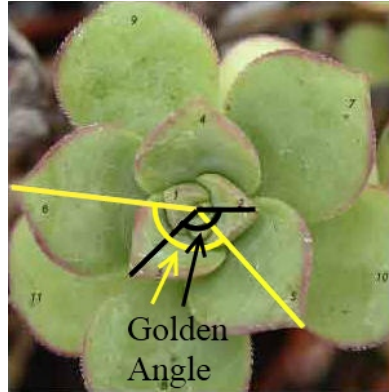
FIGURE 4.12: Appearance of the Golden Angle of 137.508º at the leaves of a plant [7]. Aggregation of the Golden Angle around the center of the plant leads to the shown leave distribution, applying (4.8)
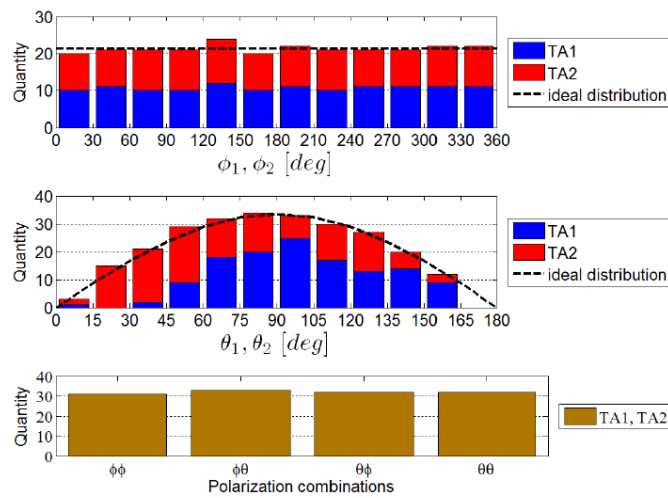
FIGURE 4.13: Histograms of: Φ_1, Φ_2 - UE placement in the azimuth plane using a uniform distribution; Θ_1, Θ_2 - test antenna (TA) position in zenith plane using a sine shaped uniform distribution; uniformly distributed polarization of the TAs [8]
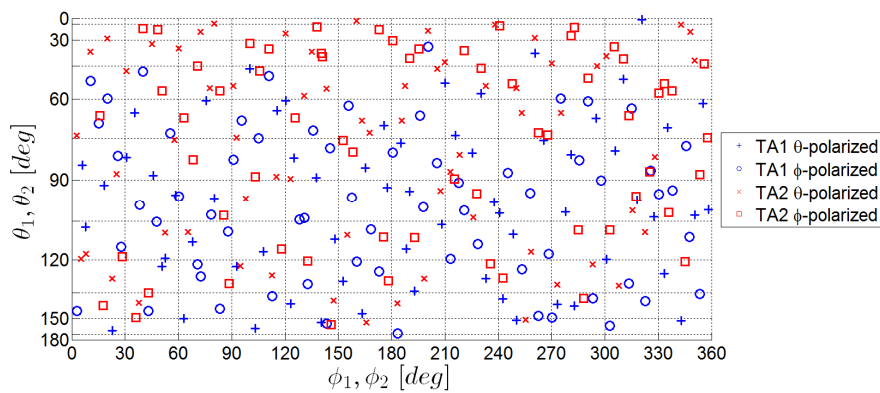
FIGURE 4.14: Constellation distribution diagram: containing Θ_1, Θ_2 - test antenna (TA) position in zenith plane; polarization of the TAs; Φ_1, Φ_2 - UE placement in the azimuth plane [8]

The sine shaped uniform distribution of Θ_1, Θ_2 is very efficient, as it minimizes the number of necessary constellations to get accurate measurement data of the antennas. Other constellation sets using random uniform distributions for Φ_1, Φ_2, Θ_1 and Θ_2 do not provide this efficiency.

4.2.4.3 Results and Extensions

The result curves of all constellations are averaged and lead to a final result curve. The averaging method is the described in Chap. 4.4.

A valuable extension of the Decomposition Method is to replace the conducted measurements with radiated measurements. Therefore one constellation is arbitrarily chosen. In this constellation a radiated unfaded measurement is performed, this is the "Baseline" result $P'_{\text{bl}}(y)$ in this case. As a next step a radiated faded measurement is executed in the same constellation, this is the "Channel" result $P'_{\text{ch}}(y)$. Both "Baseline" and "Channel" measurements again have to be done only once. Comparing the radiated measurements in the linear range, $P_{\text{ch}}(y)$ and $P_{\text{bl}}(y)$ have the same ratio as $P'_{\text{bl}}(y)$ and $P'_{\text{ch}}(y)$

$$\frac{P_{\text{ch}}(y)}{P_{\text{bl}}(y)} = \frac{P'_{\text{ch}}(y)}{P'_{\text{bl}}(y)} \tag{4.9}$$

and in the logarithmic range

$$P_{\text{ch,log}}(y) - P_{\text{bl,log}}(y) = P'_{\text{ch,log}}(y) - P'_{\text{bl,log}}(y) \tag{4.10}$$

This extension is very helpful, as any UE, also if it does not provide connections to its antennas, can be tested. Nevertheless, for better comprehensibleness the author stays with the terms *conducted* and *radiated* tests throughout the thesis.

The calibration effort for the decomposition method is intermediate, as the two the antenna paths have to be calibrated with a reference antenna.

4.3 Methods Using Reverberation Chambers

Two methods have been defined using reverberation chambers. A reverberation chamber is a reflective cavity with metallic walls. Occasionally more cavities with wave guide

connections are used. They represent the other side of the application spectrum, when it is about to reproduce a certain realistic transmission scenario in a laboratory, standing in contrast to the anechoic chamber.

An argument of the proponents for using reverberation chambers for UE testing is that indoor or urban transmission situations can be reproduced easily. A big percentage of mobile connections arise in these situations. The building costs for a reverberation chamber is less than for an anechoic chamber.

In contrast to anechoic chambers, reverberation chambers do not have quiet zones. A quiet zone is a defined volume where the device under test (DUT) has to be placed, to get reliable results.

Reverberation Chamber Method 1 and *Reverberation Chamber Method* 2 have lots of common features. The chamber setup is very similar, as both candidates make use of *mode stirrers* and a turnable table for the device under test. The stirrers alter the boundary conditions inside the chamber and move the maxima and minimas of the field. Lots of newer research work is done on reverberation chambers. A big focus has been put on the stirring elements, as they are essential for changing the propagation conditions in the chamber [63–70].

4.3.1 Reverberation Chamber Method 1

This method is the simpler one of the methods using reverberation chambers, because it doesn't make use of a channel emulator. The UE is placed on the turntable inside the chamber. Different monopole antennas inside the chamber are used for downlink and uplink connections to the mobile device. Every one of the monopoles can be switched to the base station emulator (Fig. 4.15). The BSE generates the test signals, which are transmitted as EM waves by the monopole antennas throughout the chamber. The walls are highly reflective and cause standing waves in the chamber. Every single combination of the stirring element and turntable position represents a certain point in the Rayleigh distribution. In this way artificial Rayleigh distribution is created, if many measurements with different positioning combinations are realized.

The Reverberation Chamber Method is limited in its cabilities to model generic channels [9]:

- the power delay profile (PDP) is limited to a single decaying exponent
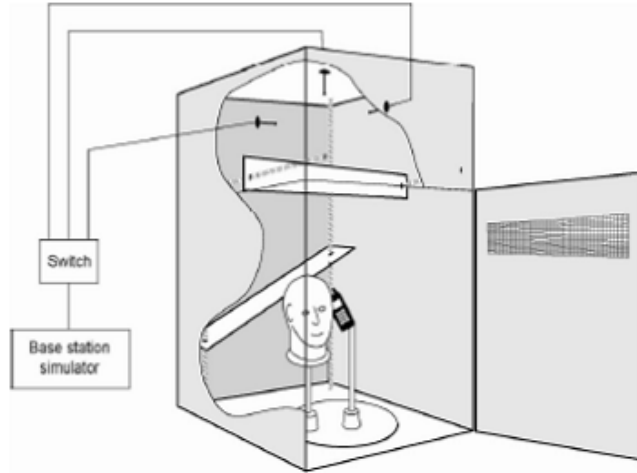
FIGURE 4.15: Reverberation Chamber Method One (single cavity) using base station emulator, monopoles, a turntable and stirring elements [9]

- the Doppler spectrum and maximum Doppler shift is limited by the motion speed of the stirrers and the turntable

- it is difficult to model certain specific MIMO fading correlations

The final result curves are achieved by averaging all single result curves.

4.3.2 Reverberation Chamber Method 2

These limitations can be overcome with Reverberation Chamber Method 2 (Fig. 4.16). It uses the same hardware setup as Reverberation Chamber Method 1, but is extended with a channel emulator. The channel emulator allows the introduction of higher Doppler spreads, tapped delay channel models and correlation models like the Kronecker model. An example of a Kronecker correlation matrix R_{ch} is (4.11), where only the base station correlation is taken into account. The Kronecker product is denoted by $\otimes$.

$$\mathbf{H}_\alpha = \sqrt{\mathbf{R}_\alpha} = \sqrt{\begin{bmatrix} 1 & \rho \\ \rho & 1 \end{bmatrix}}, \mathbf{H}_\beta = \sqrt{\mathbf{R}_\beta} = \sqrt{\begin{bmatrix} 1 & 0 \\ 0 & 1 \end{bmatrix}}, \quad \mathbf{R}_{ch} = \mathbf{R}_\alpha \otimes \mathbf{R}_\beta \qquad (4.11)$$

The base station correlation matrix is denoted by $\mathbf{R}_\alpha$ and the UE correlation matrix is denoted by $\mathbf{R}_\beta$. Using these correlation matrices $\mathbf{R}_\alpha$ and $\mathbf{R}_\beta$, the correlation channel matrices $\mathbf{H}_\alpha$ and $\mathbf{H}_\beta$ can be computed, as shown in (4.11). The correlation matrices $\mathbf{H}_\alpha$ and $\mathbf{H}_\beta$ introduce correlation between the MIMO channels, where $\mathbf{H}_{\text{ch}}$ is a generic
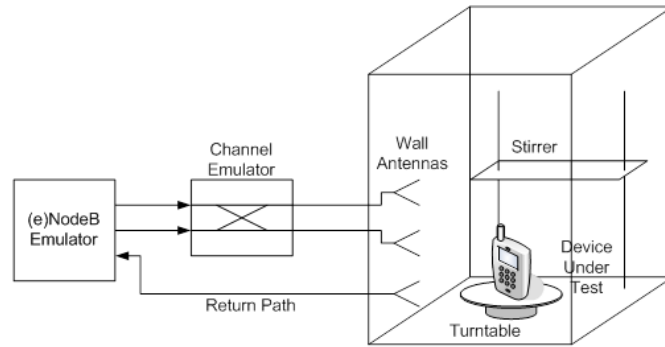
FIGURE 4.16: Reverberation chamber (single cavity) with placed UE using base station emulator, monopoles, a turntable, stirring elements and a fading emulator [9]

channel matrix with uncorrelated elements [9]

$$\mathbf{H}_{\text{ch,correlated}} = \mathbf{H}_{\beta} \; \cdot \; \mathbf{H}_{\text{ch}} \; \cdot \; \mathbf{H}_{\alpha} \tag{4.12}$$

The number of test antennas, also denoted as "wall antennas" should be at least as high as the number of MIMO channels.

There are three different methods to run the tests:

1. The turn table and the stirrers are fixed during a measurement, between them they change the position. The channel emulator is allowed to run for a fixed time length and is paused then.

2. The turn table and the stirrers move continuously, the FOM (figure of merit) is measured continuously. The channel emulator is off.

3. As in point 2, but the channel emulator is running continuously. This mode is the most comparable one to anechoic chamber methods.

Again, all single result curves are averaged and deliver the final result curve. Summarizing the highlights and downsides, the Reverberation Chamber Methods 1 and 2 have many limitations but still offer good performance test possibilities. One of the big limitations is that all Angle of Arrival (AoA) and Angle of Departure (AoD) information of the EM waves gets lost. The angular influence of the antenna pattern is reflected only on an averaged level. Nevertheless, the equipment cost is much lower than in other methods, as the chamber can be built for a lower price than an anechoic chamber.

4.4 Averaging Result Curves of All Constellations

All methods deliver many different single result curves of are averaged to achieve one single final result curve. The employed averaging algorithm is the *inverse averaging algorithm* [9], which is tending strongly towards lower values. N is the total number of measurements.

$$P_{avg,inverse}(y) = \frac{N}{\sum\limits_{n=1}^{N} \frac{1}{P_n(y)}} \tag{4.13}$$

Within one constellation also averaging takes place. In contrast to the inverse averaging method used between different constellations, the author applies linear averaging for the result curves within the same realization of transmission channels.

4.5 Comparison of Test Methods

For better visibility the features of the different methods is summarized in Tab. 4.1. The author evaluates them qualitatively by their hardware effort, measurement time, equipment cost, calibration effort and mechanical sensibility of the setup.

There is no ideal solution existing, there always has to be a weighting between costs, complexity and how well a certain method can map a certain real world transmission scenario into a measurement setup.

The mechanical sensibility is a very practical point, which the user should not underestimate. Operators without the necessary technical knowledge might not understand that exact placement of the test antennas or the UE can be of tremendous importance and directly influences the measurement results. All methods have some mentionable advan-

Test method	Multi-Probe	Two-Stage	Decomposition	Reverb. 1	Reverb. 2
Setup	Anechoic Chamber			Reverberation chamber	
Hardware Effort	high	normal	normal	normal/low	normal/low
Measurement Time	fast	normal	normal	fast	fast
Equipment Costs	high	normal	normal	normal/low	normal/low
Calibration Effort	high	low	low	low	low
Spatial resolution	medium	high	high	-	-
Mechanical Sensibility	high	low	low	low	low

TABLE 4.1: Qualitative comparison of MIMO OTA test methods with anechoic and reverberation chambers

tages, they are listed in Tab. 4.2. On the other hand also method specific drawbacks

exist, these are mentioned in Tab. 4.3. *AoA* denotes *Angle of Arrival*, *AoD* denotes the *Angle of Departure* of the EM waves as seen from the UE.

Method Name	Chamber Type	Highlights
Multi-Probe	Anechoic	fast and precise method
Two-Stage Method	Anechoic	simple anechoic chamber can be used
Decomposition Method	Anechoic	very good compromise between effort and result accuracy
Reverberation Chamber 1	Reverberation	low costs and quick measurements
Reverberation Chamber 2		low costs and quick measurements

TABLE 4.2: Benefits of the different MIMO OTA measurement methods

Method Name	Chamber Type	Downsides
Multi-Probe	Anechoic	only two dimensional measurements possible
Two-Stage Method	Anechoic	desensitization of UE not recognized
Decomposition Method	Anechoic	only two downlink streams possible
Reverberation Chamber 1	Reverberation	no influence of AoA and AoD can be detected
Reverberation Chamber 2	Reverberation	no influence of AoA and AoD can be detected

TABLE 4.3: Drawbacks of the different MIMO OTA measurement methods

The *Multi-Probe Method* is fast and accurate, but it lacks the possibility to check the UE in all three dimensions. There is the possibility to put a second antenna probe ring. Still many positions will not be covered of a complete measurement sphere. Also the calibration effort is very high, as much equipment is envolved.

The *Two-Stage Method* is an efficient method. It reduces anechoic chamber usage to a minimum. But it has the drawback, that it does not really cover *desensitization* of the receive path by the UE transmitter itself. Antennas are simulated in the channel emulator and do not cover these effects. There is also no real *end to end* test involving all stages. If radiated connections are used, the method looses lots of its efficiency.

The *Decomposition-Method* is a well balanced method between effort and test possibility coverage. It has the drawback, that only two radio paths with arbitrary polarization are available. By usage of the second polarization of the test antennas a maximum of four paths become available. The hardware effort is normal, as it needs a base station emulator, a channel emulator and an anechoic chamber with test antennas and UE placement.

The *Reverberation Chamber Methods* are the underdogs in terms of MIMO OTA testing. They lack some important possibilities, but are feasible to do the tests with minimum effort and test time. Reverberation chamber methods cannot distinguish between different *AoAs* and AoDs, as waves come from all directions. Therefore the influence of the antenna patterns, which depend on the angles of the waves, cannot be seen well. On the other hand, indoor situations can be modeled very well.

4.6 Selection of a Test Method for Further Investigation

Some of the test method are well described, while others lack investigations but offer lots of possibilities. This thesis takes a closer look on the *Decomposition Method* as it is a good compromise between costs of equipment, test time, measurement possibilities and accuracy of the results. Consuming channel measurements are being reduced to an absolute minimum and the UE is scanned fully 3D. The described advantages (tab. 4.2) win over the drawbacks (tab. 4.3). It is open to further development in testing MIMO OTA transmission systems.

Chapter 5

Prerequisites for the Validation of the Decomposition Method

5.1 Introduction

The Decomposition Method is the method of choice, the validation of this method is the goal of this thesis. The author validates the hypothesis that radiated fading measurements can be split in conducted and radiated measurements. This chapter explains the prerequisites for the validations and gives insight on the employed transmission systems and its elements. It takes a "Top Down" approach and starts with block diagrams of the transmission systems and progresses to the single blocks. The author explains simplified transmission systems with uncorrelated channel matrices in Chap. 5.2. Full transmission systems with uncorrelated and correlated channel matrices, as used in the numerical simulations, are depicted in Chap. 5.3.

Transmission systems using uncorrelated channel matrices are used for the validation with the MIMO channel capacity approach in Chap. 6. Both uncorrelated and correlated channel matrices are used in the transmission systems of the numerical simulations in Chap. 7. All employed transmission systems use 2×2 MIMO schemes.

5.2 Block Diagrams for the Validation Using the MIMO Channel Capacity Approach

The block diagrams of all transmission systems employed in the validation using the MIMO channel capacity approach are shown in Fig. 5.1. The transmission systems consist of the following blocks:

- a Base Station Emulator (BSE)

- an antenna matrix $\mathbf{H}_{\mathrm{ant}}$ and a channel matrix $\mathbf{H}_{\mathrm{ch}}$

- an intrinsic noise source of the UE $n_{\mathrm{n\_rec}}$

- a receiver, denoted by $\mathbf{H}^{\mathrm{P}}$

Base station antennas are assumed to be uncorrelated and are modeled with a 2×2 identity matrix $\begin{bmatrix} 1 & 0 \\ 0 & 1 \end{bmatrix}$. This is the reason why no base station antenna block is shown throughout Fig. 5.1.

The simple transmission systems without correlated channel matrices are depicted in Fig. 5.1, the author employs them in Chap. 6:

- The "Overall" transmission system containing the channel matrix $\mathbf{H}_{\mathrm{ch}}$ and the antenna matrix $\mathbf{H}_{\mathrm{ant}}$ (Fig. 5.1(a)).

- The radiated static "Antenna" transmission system containing the receiving antenna matrix $\mathbf{H}_{\mathrm{ch}}$ (Fig. 5.1(b)).

- The conducted fading "Channel" transmission system containing $\mathbf{H}_{\mathrm{ch}}$ (Fig. 5.1(c)).

- The conducted "Baseline" transmission system containing a direct wired connection between BSE and UE, which is represented by a 2×2 identity matrix (Fig. 5.1(d)).

The transmission systems block diagrams in Fig. 5.1 visualize the following transmission equations:

$$(a) \quad \mathbf{y} = \mathbf{H}^{\mathrm{P}} \left(\mathbf{H}_{\mathrm{ant}} \ \mathbf{H}_{\mathrm{ch}} \ \mathbf{s} + \mathbf{n}_{\mathrm{n\_rec}} \right) \tag{5.1}$$
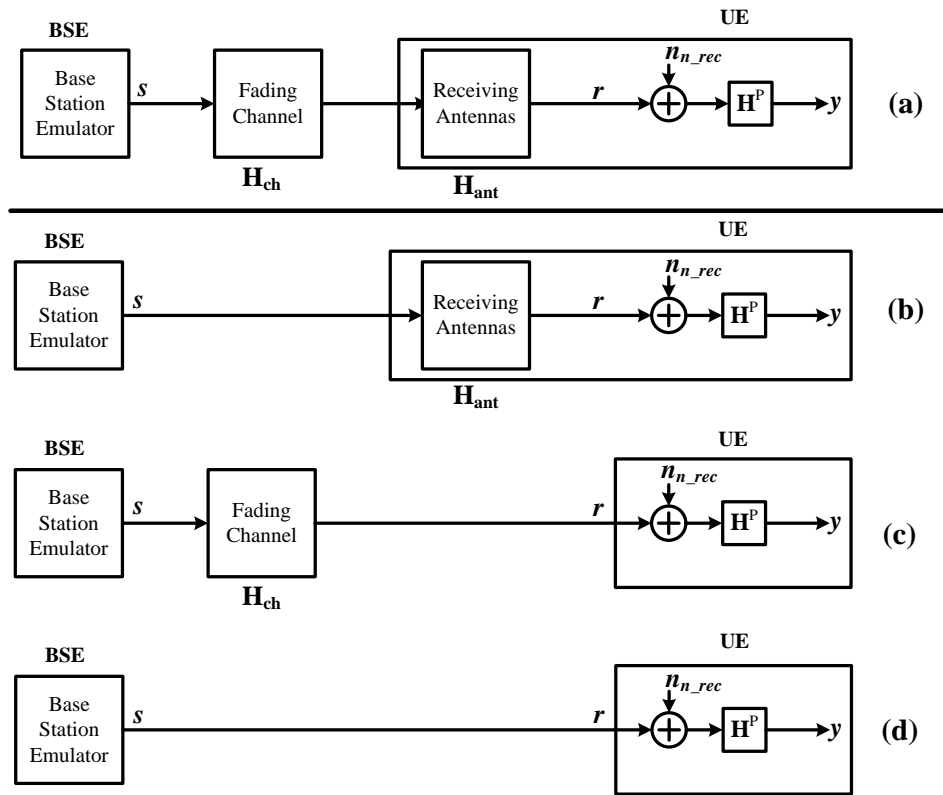
FIGURE 5.1: Block diagrams of the transmission systems used for the validation of the Decomposition Method using the MIMO channel capacity approach

$$(b) \quad \mathbf{y} = \mathbf{H}^{\mathrm{P}} \left(\mathbf{H}_{\mathrm{ant}} \ \mathbf{s} + \mathbf{n}_{\mathrm{n\_rec}} \right) \tag{5.2}$$

$$(c) \quad \mathbf{y} = \mathbf{H}^{\mathrm{P}} \left(\mathbf{H}_{\mathrm{ch}} \ \mathbf{s} + \mathbf{n}_{\mathrm{n\_rec}} \right) \tag{5.3}$$

$$(d) \quad \mathbf{y} = \mathbf{H}^{\mathrm{P}} \left(\mathbf{s} + \mathbf{n}_{\mathrm{n\_rec}} \right) \tag{5.4}$$

5.3 Block Diagrams for the Validation using Numerical Simulations

The complete transmission chain containing all blocks except Downlink Shared Channel Processing (DLSCH) can be seen in Fig. 5.2. They are used in the numerical simulations in Chap. 7. For best understanding, the reader has to jump between the text, the transmission block diagrams in Fig. 5.3 to Fig. 5.9 and the transmission equations (5.7) to (5.14).

A random data stream is generated, and the "MIMO processing - transmit" block splits

the data into two data streams, as a MIMO 2×2 system is investigated. The binary data streams are QPSK modulated and pass the BSE antennas, which are represented by a 2×2 identity matrix.

The matrix $\mathbf{H}_\alpha = \sqrt{\mathbf{R}_\alpha}$ models the correlation introduced by the base station antennas, if they are not uncorrelated anymore, as assumed in Chap. 5.2. The matrix $\mathbf{H}_\beta = \sqrt{\mathbf{R}_\beta}$ is used to model additional UE antenna correlation.

The data pass the base station correlation matrix $\mathbf{H}_\alpha$, the uncorrelated channel matrix $\mathbf{H}_{\mathrm{ch}}$ and the UE correlation matrix $\mathbf{H}_\beta$. In practice, the matrices $\mathbf{H}_\alpha$ and $\mathbf{H}_\beta$ are processed in the channel emulator. This is the reason why they are part of the "Channel" scenario in all block diagrams.

The receiving antenna matrix again can change the amplitude and the phase of the data signals and intrinsic UE noise is added before they are modified in the receiver block $\mathbf{C}$. The symbols arrive at the detector and the symbol decisions are done employing a minimum euclidian distance algorithm. Afterwards the parallel bit streams are reshaped into a serial one. The symbols are determined applying the minimum Euclidian distance algorithms without prior knowledge. In case the ICD/ZF receiving algorithm [16] is investigated,

$$\mathbf{C} = (\mathbf{H}^{\mathrm{H}}\mathbf{H})^{-1}\mathbf{H}^{\mathrm{H}}. \tag{5.5}$$

$\mathbf{C}$ is the *Moore Penrose Pseudoinverse* of a general channel matrix $\mathbf{H}$, which is a reduced to a simple matrix inversion in the case of a square channel matrix.

In the case the Minimum Mean Square Error (MMSE) receiver concept [16] is investigated,

$$\mathbf{C} = (\mathbf{H}^{\mathrm{H}}\mathbf{H} + N_0\mathbf{I})^{-1}\mathbf{H}^{\mathrm{H}}. \tag{5.6}$$

The inverse channel detector/zero forcing (ICD/ZF) receiver equalizes the channel perfectly, but it enhances the noise in the case the channel matrix $\mathbf{H}$ is not well conditioned [15]. The MMSE concept reduces this drawback by simply adding the diagonal offset matrix $N_0\mathbf{I}$ containing the proportional noise contribution (5.6). Both concepts are widely used, therefore they are investigated. In the case of a transmission without any errors, the transmit (TX) data stream and the receive (RX) data stream are equal.

As mentioned in Chap. 4.2.4.2, the Decomposition Method needs three result types, the "Baseline", "Antenna" and "Channel" result, to compute its final outcome. The "Baseline" simulation block diagram is pictured in Fig. 5.3. It represents the BSE connected to the UE by wires, delivering a certain throughput with the lowest possible downlink

power. The "Antenna" transmission scheme is depicted in Fig. 5.4 and represents the radiated static transmission scenario. The "Channel" transmission scheme is exhibited in Fig. 5.5 including a wired connection between the BSE and the UE, plus the correlation matrices $\mathbf{H}_\alpha$, $\mathbf{H}_\beta$ and the uncorrelated channel matrix $\mathbf{H}_\text{ch}$. If a simulation set includes the channel estimation error, all channel parameters of $\mathbf{H}_\text{ch}$ have the normally distributed estimation error signal with variance $\sigma^2_\text{est\_error}$ and zero mean value μ overlayed.

The more complex transmission schemes also include Downlink Shared Channel (DLSCH) processing with Cyclic Redundancy Check (CRC) calculation, turbo coding, rate matching, etc. The transmission scenarios are almost the same as above, but now include DLSCH processing. They are shown in the following figures:

- "Overall" transmission scenario, Fig. 5.6

- "Baseline" transmission scenario, Fig. 5.7

- "Antenna" transmission scenario, Fig. 5.8

- "Channel" transmission scenario, Fig. 5.9

5.3.1 Block Diagrams without Downlink Shared Channel Processing (DLSCH)

This chapter depicts the block diagram of all transmission systems without DLSCH employed in the numerical validations. The signal leaving the transmit antennas are described by $\mathbf{s}$.
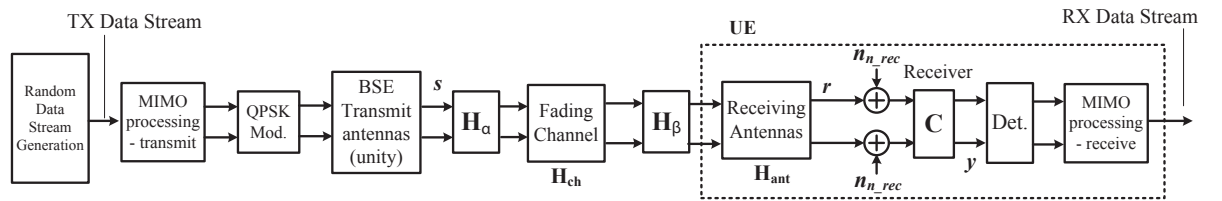
FIGURE 5.2: Wireless transmission system block diagram for the "Overall" simulation (5.7)

The transmission systems shown in Fig. 5.2 to Fig. 5.5 can be described by the detector input signal

$$\text{Fig. 5.2:} \qquad \mathbf{y} = \mathbf{C}\,(\mathbf{H}_\text{ant}\,\mathbf{H}_\beta\,\mathbf{H}_\text{ch}\,\mathbf{H}_\alpha\,\mathbf{s} + \mathbf{n}_\text{n\_rec}), \qquad\qquad (5.7)$$
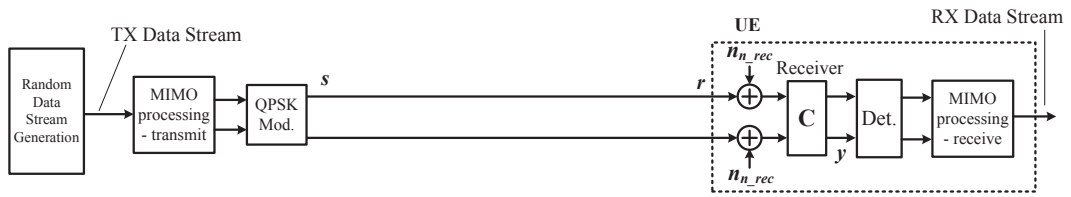
FIGURE 5.3: Wireless transmission system block diagram for the "Baseline" simulation (5.8)
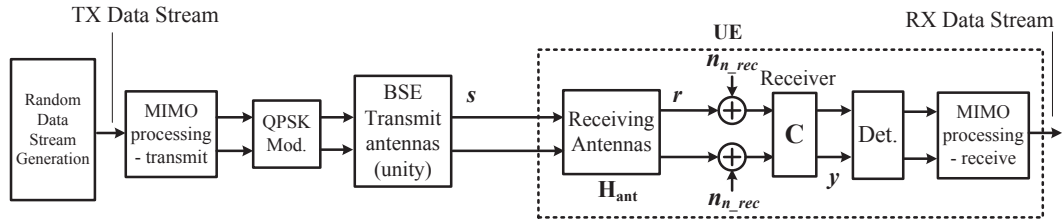
FIGURE 5.4: Wireless transmission system block diagram for the "Antenna" simulation (5.9)
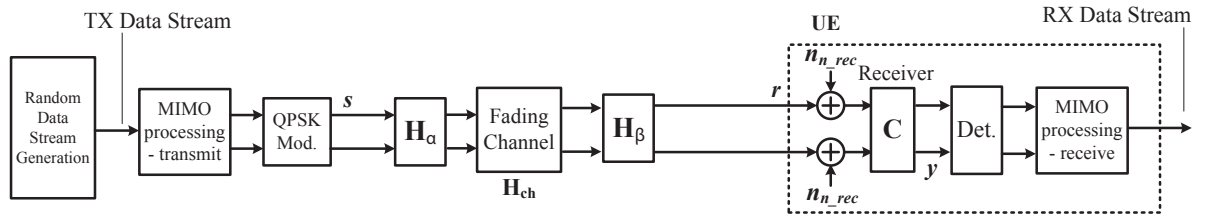
FIGURE 5.5: Wireless transmission system block diagram for the "Channel" simulation (5.10)

$$\text{Fig. 5.3:} \quad \mathbf{y} = \mathbf{C} \left(\mathbf{s} + \mathbf{n}_{\text{n\_rec}} \right), \tag{5.8}$$

$$\text{Fig. 5.4:} \quad \mathbf{y} = \mathbf{C} \left(\mathbf{H}_{\text{ant}} \ \mathbf{s} + \mathbf{n}_{\text{n\_rec}} \right), \tag{5.9}$$

$$\text{Fig. 5.5:} \quad \mathbf{y} = \mathbf{C} \left(\mathbf{H}_{\beta} \ \mathbf{H}_{\text{ch}} \ \mathbf{H}_{\alpha} \ \mathbf{s} + \mathbf{n}_{\text{n\_rec}} \right). \tag{5.10}$$

5.3.2 Block Diagrams Employing Downlink Shared Channel Processing (DLSCH)

This chapter depicts the block diagrams of all transmission systems including DLSCH employed in the numerical validations and depicts the transmission equations.
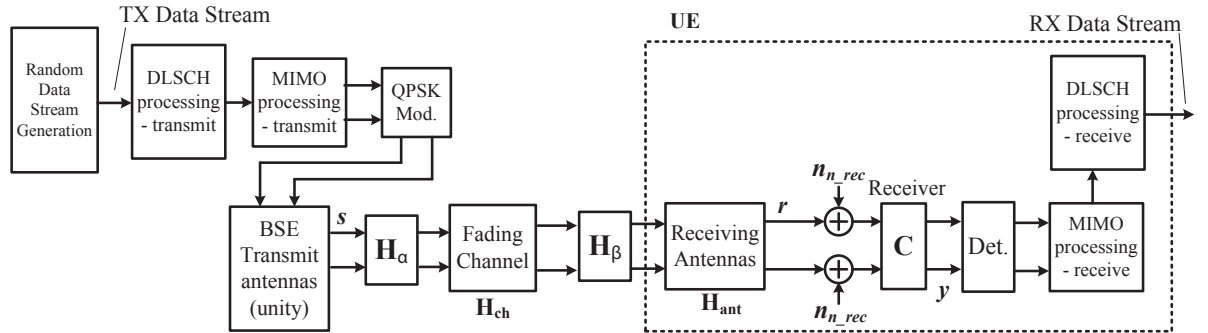
FIGURE 5.6: Wireless transmission system block diagram for the "Overall" simulation including DLSCH processing
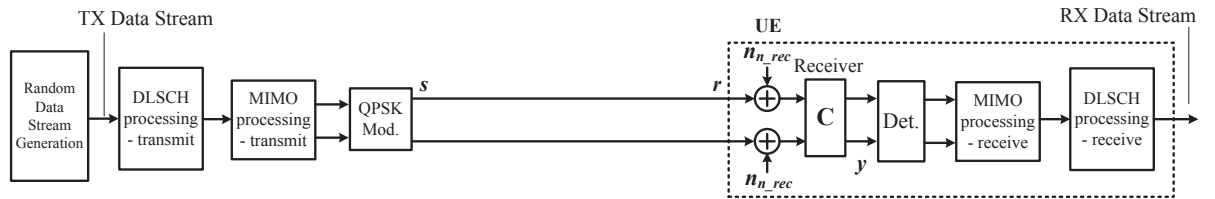
FIGURE 5.7: Wireless transmission system block diagram for the "Baseline" simulation including DLSCH processing
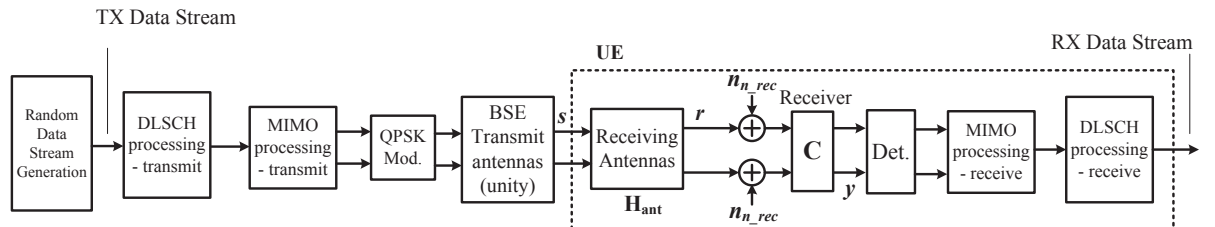
FIGURE 5.8: Wireless transmission system block diagram for the "Antenna" simulation including DLSCH processing

Again, the transmission systems depicted in Fig. 5.6 to Fig. 5.9 can be described by the detector input signal

$$\text{Fig. 5.6:} \qquad \mathbf{y} = \mathbf{C} \left(\mathbf{H}_{\text{ant}} \, \mathbf{H}_\beta \, \mathbf{H}_{\text{ch}} \, \mathbf{H}_\alpha \, \mathbf{s} + \mathbf{n}_{\text{n\_rec}} \right), \qquad (5.11)$$
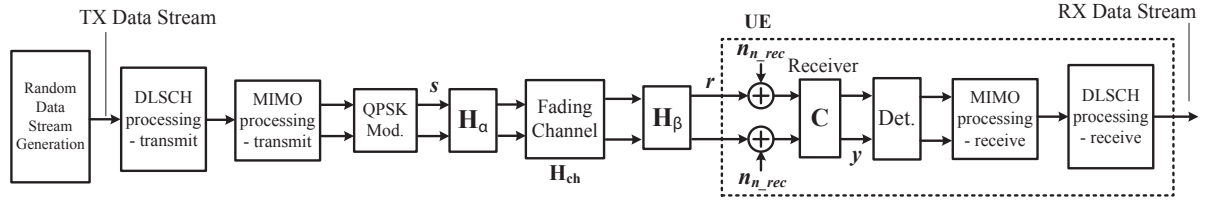
FIGURE 5.9: Wireless transmission system block diagram for the "Channel" simulation including DLSCH processing

$$\text{Fig. 5.7:} \quad \mathbf{y} = \mathbf{C} \ (\ \mathbf{s} + \mathbf{n}_{\text{n\_rec}}), \tag{5.12}$$

$$\text{Fig. 5.8:} \quad \mathbf{y} = \mathbf{C} \ (\mathbf{H}_{\text{ant}} \ \mathbf{s} + \mathbf{n}_{\text{n\_rec}}), \tag{5.13}$$

$$\text{Fig. 5.9:} \quad \mathbf{y} = \mathbf{C} \ (\ \mathbf{H}_{\beta} \ \mathbf{H}_{\text{ch}} \ \mathbf{H}_{\alpha} \ \mathbf{s} + \mathbf{n}_{\text{n\_rec}}). \tag{5.14}$$

5.4 Matrix Models for the Transmission Channels

In general, transmission channels with frequency flat fading have been applied. This results in 2×2 channel matrices, where each channel element h_{ij} simply represents the complex transmission gain. The channel matrix elements have complex normal distributions, independent from each other. This means that the amplitude is Rayleigh distributed and the phase is *independent and identically distributed* (IID). It has been assumed that no intersymbol interference (ISI) is taking place. The author employs the following channel matrices $\mathbf{H}_{\text{ch}}$:

- identity matrix $\mathbf{H}_{\text{ch}} = \begin{bmatrix} 1 & 0 \\ 0 & 1 \end{bmatrix}$ for the "Baseline" result.

- fading channel $\mathbf{H}_{\text{ch}}$ with no line of sight component (NLOS) with complex Gaussian distribution of its channel matrix elements $h_{\text{ch},i,j}$, where $i,j \in \{1,2\}$. The complex Gaussian distribution leads to a Rayleigh amplitude distribution. The angles are identically and independently distributed (IID). The basis channel matrix follows the distribution $\tilde{\mathbf{H}}_{\text{ch}} = \mathbb{C}\mathcal{N}(0|1)$. The amplitude scaled version of the channel matrix is $\mathbf{H}_{\text{ch}} = A \ \tilde{\mathbf{H}}_{\text{ch}} = \begin{bmatrix} h_{\text{ch},11} & h_{\text{ch},12} \\ h_{\text{ch},21} & h_{\text{ch},22} \end{bmatrix}$ for the "Channel" and "Overall" simulations.

The author employs the mentioned factor A to scale the channel matrix $\tilde{\mathbf{H}}_{\mathrm{ch}}$. This scaling represents the fact that the channel matrix $\mathbf{H}_{\mathrm{ch}}$ has lower transmission gain than the identity matrix $\begin{bmatrix} 1 & 0 \\ 0 & 1 \end{bmatrix}$. All channel power gains are average channel power gains. The channel power gain is represented by the expectation value of the squared Frobenius norm of the channel matrix, which is denoted by the $\|.\|_F^2$ [71]

$$\mathscr{E}\left\{\|\mathbf{H}_{\mathrm{ch}}\|_F^2\right\} = \mathscr{E}\left\{\sum_{i=1}^{2}\sum_{j=1}^{2}|h_{\mathrm{ch},i,j}|^2\right\} = \sum_{i=1}^{2}\sum_{j=1}^{2}\mathscr{E}\left\{|h_{\mathrm{ch},i,j}|^2\right\} \tag{5.15}$$

The average power gain of the identity matrix is

$$\mathscr{E}\left\{\left\|\begin{bmatrix} 1 & 0 \\ 0 & 1 \end{bmatrix}\right\|_F^2\right\} = \left\|\begin{bmatrix} 1 & 0 \\ 0 & 1 \end{bmatrix}\right\|_F^2 = 2 \tag{5.16}$$

The average power gain of the Rayleigh fading channel has to be smaller than 2, which reflects the fact that the passive transmission channel has less power gain than the identity channel matrix. The identity channel matrix is physically represented by a wired connection between BSE and UE.

The author sets the average power gain of the Rayleigh fading channel to ν

$$\mathscr{E}\left\{\|\mathbf{H}_{\mathrm{ch}}\|_F^2\right\} = \nu, \tag{5.17}$$

where the condition $\nu < 2$ has to be fulfilled, the author chooses $\nu = 0.4096$ arbitrarily. The second moment for a complex gaussian distribution [72] is

$$\Sigma^2 = |h_{\mathrm{ch},i,j}|^2 = 2\sigma^2, \tag{5.18}$$

where σ is the standard deviation of the complex Gaussian distributed channel parameters $h_{\mathrm{ch},i,j}$

$$\mathscr{E}\left\{\|\mathbf{H}_{\mathrm{ch}}\|_F^2\right\} = \sum_{i=1}^{2}\sum_{j=1}^{2}\mathscr{E}\left\{|h_{\mathrm{ch},i,j}|^2\right\} = \sum_{i=1}^{2}\sum_{j=1}^{2}2\sigma^2 A^2 = \nu \tag{5.19}$$

With the standard deviation $\sigma = 1$, the scaling factor is

$$A = 0.2263. \tag{5.20}$$

All simulations in Chap. 6 and Chap. 7 employ $\mathbf{H}_{\text{ch}}$ including the scaling factor A and a complex Gaussian distributed channel with $\sigma = 1$.

5.4.1 Kronecker Channel Model

The numerical simulations in Chap. 7 go further in detail than the validation using the MIMO channel capacity formula in Chap. 6. They include a correlation based channel model with flat fading, the so-called **Kronecker channel model** [73], [74]. The correlation between the elements of a general correlated channel matrix $\mathbf{H}_{\text{ch,corr}}$

$$\mathbf{H}_{\text{ch,corr}} = \begin{bmatrix} h_{\text{ch,corr,11}} & h_{\text{ch,corr,12}} \\ h_{\text{ch,corr,21}} & h_{\text{ch,corr,22}} \end{bmatrix} \tag{5.21}$$

can be denoted in its correlation matrix

$$\mathbf{R} = \mathscr{E}\{\text{vec}(\mathbf{H}_{\text{ch,corr}})\text{vec}(\mathbf{H}_{\text{ch,corr}})^{\text{H}}\} \tag{5.22}$$

which is calculated using the vec($\mathbf{H}$) function of the general correlated channel matrix. The vector function *vec* stacks the columns of the matrix $\mathbf{H}_{\text{ch,corr}}$ in a single column vector

$$\text{vec}(\mathbf{H}_{\text{ch,corr}}) = \begin{bmatrix} h_{ch,corr,11} \\ h_{ch,corr,21} \\ h_{ch,corr,12} \\ h_{ch,corr,22} \end{bmatrix} \tag{5.23}$$

A practical way is to "split" the correlation matrix $\mathbf{R}$ in the two parts called $\mathbf{R}_\alpha$ and $\mathbf{R}_\beta$, a transmitter and a receiver side correlation part. These parts can be combined again to $\mathbf{R}$ by the use of the *Kronecker matrix product* [74]

$$\mathbf{R} = \mathbf{R}_\alpha \otimes \mathbf{R}_\beta. \tag{5.24}$$
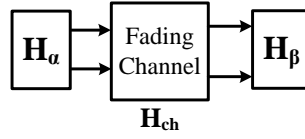
FIGURE 5.10: Kronecker channel model with flat fading employing the uncorrelated channel matrix $\mathbf{H}_{\text{ch}}$, the base station correlation matrix $\mathbf{H}_\alpha$ and the UE correlation matrix $\mathbf{H}_\beta$

The use of the Kronecker product is the reason for Kronecker being the titular saint for the name of the channel model. The channel matrix with its uncorrelated complex-normal distributed elements is

$$\mathbf{H}_{\text{ch}} = \begin{bmatrix} h_{\text{ch},11} & h_{\text{ch},12} \\ h_{\text{ch},21} & h_{\text{ch},22} \end{bmatrix}. \tag{5.25}$$

The correlation matrices $\mathbf{R}_\alpha$ and $\mathbf{R}_\beta$ can be employed effectively to calculate the correlated channel matrix by using the square root of the matrices $\mathbf{R}_\alpha$ and $\mathbf{R}_\beta$ [74]

$$\mathbf{H}_{\text{ch,corr}} = \mathbf{R}_\beta^{1/2} \mathbf{H}_{\text{ch}} \mathbf{R}_\alpha^{1/2} = \mathbf{H}_\beta \mathbf{H}_{\text{ch}} \mathbf{H}_\alpha. \tag{5.26}$$

$\mathbf{H}_\alpha$ represents the correlation of the base station antennas, $\mathbf{H}_\beta$ corresponds to the correlation on the UE side, additionally to the intrinsic correlation of the UE antenna system. Both have the following form to be used in transmission equations [74]

$$\mathbf{H}_\alpha = \sqrt{\mathbf{R}_\alpha} = \sqrt{\begin{bmatrix} 1 & \alpha \\ \alpha & 1 \end{bmatrix}} \qquad \mathbf{H}_\beta = \sqrt{\mathbf{R}_\beta} = \sqrt{\begin{bmatrix} 1 & \beta \\ \beta & 1 \end{bmatrix}}, \tag{5.27}$$

where the off-diagonal elements α and β are a measure for the cross coupling between the data paths. Fig. 5.10 shows the three matrices, namely $\mathbf{H}_\alpha$, $\mathbf{H}_{\text{ch}}$ and $\mathbf{H}_\beta$. This is the form the correlated channels are used in the following simulations. [73] and [75] propose to employ three different combinations for $\mathbf{H}_\alpha$ and $\mathbf{H}_\beta$ called:

- Low correlation:

$$\mathbf{H}_\alpha = \sqrt{\begin{bmatrix} 1 & 0 \\ 0 & 1 \end{bmatrix}}, \quad \mathbf{H}_\beta = \sqrt{\begin{bmatrix} 1 & 0 \\ 0 & 1 \end{bmatrix}}$$

- Medium correlation: $\mathbf{H}_\alpha = \sqrt{\begin{bmatrix} 1 & 0.3 \\ 0.3 & 1 \end{bmatrix}}, \quad \mathbf{H}_\beta = \sqrt{\begin{bmatrix} 1 & 0.9 \\ 0.9 & 1 \end{bmatrix}}$

- High correlation: $\mathbf{H}_\alpha = \sqrt{\begin{bmatrix} 1 & 0.9 \\ 0.9 & 1 \end{bmatrix}}, \quad \mathbf{H}_\beta = \sqrt{\begin{bmatrix} 1 & 0.9 \\ 0.9 & 1 \end{bmatrix}}$

5.4.2 Antenna Matrices

The base station antennas are represented by an identity matrix of the dimension 2×2, they do not have influence on the transmission and are not represented in the equations. The matrix $\mathbf{H}_{\text{ant}}$ is calculated with the complex E-field pattern of the receiving antennas of the UE [61].

$$\mathbf{H}_{\text{ant}} = \begin{bmatrix} h_{\text{ant},11} & h_{\text{ant},12} \\ h_{\text{ant},21} & h_{\text{ant},22} \end{bmatrix} = \begin{bmatrix} R_{p1}(\Omega_1) & R_{q1}(\Omega_2) \\ R_{p2}(\Omega_1) & R_{q2}(\Omega_2) \end{bmatrix} \quad \{p, q \in \Theta, \Phi\} \tag{5.28}$$

R denotes the complex E-field pattern of the receiving antenna 1 or 2. The author denotes the polarizations of the test antennas with $\{p, q\}$. These polarizations $\{p, q\}$ can be in the Φ- or in the Θ-plane, denoted by Φ and Θ. The exemplarily taken matrices $\mathbf{H}_{\text{ant}}$ shown in Tab. 5.1 represent the E-field pattern imaginary antennas with certain condition numbers $\kappa_{\log}$. The antenna matrix $\mathbf{H}_{\text{ant}}$ is normalized to a squared Frobenius Norm (SQFN) of 2

$$\|\mathbf{H}_{\text{ant}}\|_F^2 = \sum_{i=1}^{2} \sum_{j=1}^{2} |h_{\text{ant},ij}|^2 = 2, \tag{5.29}$$

which corresponds to the power gain of an identity matrix, shown in (5.16). The reason is that results can be compared easily, if the power gain is the same for all $\mathbf{H}_{\text{ant}}$. The antenna condition number in linear terms

$$\kappa_{\text{lin}} = \frac{\sigma_{\max}}{\sigma_{\min}} \tag{5.30}$$

is the ratio of the largest to the smallest eigenvalue of the antenna matrix $\mathbf{H}_{\text{ant}}(\Omega_1, \Omega_2)$ (5.30). The bigger it is, the worse is the matrix conditioning. For the definition of the constellations Ω please revise Chap. 3.2.

$\mathbf{H}_{\mathrm{ant}}$	κ_{log} /dB	coupling between signal paths
$\begin{bmatrix} 1 & 0 \\ 0 & 1 \end{bmatrix}$	0	no coupling
$0.8874 \begin{bmatrix} 1 & 0.51949 \\ 0.51949 & 1 \end{bmatrix}$	10	light coupling
$0.71414 \begin{bmatrix} 1 & 0.9802 \\ 0.9802 & 1 \end{bmatrix}$	40	strong coupling

TABLE 5.1: Antenna matrices with different coupling and condition number

For visualization purposes the author defines

$$\kappa_{\mathrm{log}} = 20 \, \log_{10}(\kappa_{\mathrm{lin}}). \qquad (5.31)$$

The identity antenna matrix corresponds to fully decoupled antennas, with $\kappa_{\mathrm{log}} = 0 \, \mathrm{dB}$. Increasing coupling between the antennas provide antenna matrices with higher condition numbers. Tab. 5.1 shows examples of different antenna matrices, for fully decoupled antennas ($\kappa = 0 \, \mathrm{dB}$) to strongly coupled antennas ($\kappa = 40 \, \mathrm{dB}$).

5.5 LTE as a Show Case for MIMO Enabled Communication Standards

The wireless mobile communication standard Long Term Evolution (LTE) is a common use case for the application of the Decomposition Method. Therefore a short description of LTE follows. It is a state of the art standard for wireless data communication technology. One of the major goals for its specification was to increase the data transmission capacity and the speed of the wireless networks in comparison to GSM and UMTS. These goals can mainly be reached by applying new digital signal processing (DSP) techniques and advanced modulation and coding schemes, which became available around the year 2000. The specification of LTE (Release 8) was finished in 2009 and from then on many mobile network operators started tests [76].

LTE allows data throughput rates up to 326.4 Mbit/s for the downlink and 86.4 MBit/s

for the uplink, employing a 4×4 MIMO antenna system [77]. LTE has an average latency around 50 ms in the Radio Access Network (RAN) [78]. It has the ability to manage fast moving UEs and supports broadcast and multicast-streams. It employs carriers with scalable bandwidth, from 1.4 MHz to 20 MHz. It allows Frequency Division Duplex (FDD), as well as Time Division Duplex (TDD). Its Internet Protocol (IP) based network architecture Evolved Package Core (EPC) will replace old General Packet Radio Service (GPRS) networks. Seamless handovers of voice and data services for base stations using older technology like the Global System for Mobile Communications (GSM), the Universal Mobile Telecommunications System (UMTS) and the Code Division Multiple Access (CDMA) 2000 system are possible. The overall architecture is simpler than of its predecessors, as an Evolved UMTS Terrestrial Radio Access (E-UTRA) cell can support four times the amount of users of an High Speed Package access (HSPA) cell [76].

LTE makes use of eight different powerful transmission modes like *transmit diversity, open loop single user MIMO, closed loop single user MIMO* and *beamforming modes*, to name the most important ones.

5.5.1   OFDM (Orthogonal Frequency Division Multiplexing)

OFDM and the uplink pendant SC-FDM (Single Carrier Frequency Division Multiplexing) are used in LTE. The main reasons are:

- robustness of the transmission system to frequency-dependent fading channels

- high spectral efficiency

OFDM is a multi-carrier scheme, which divides the occupied frequency band in many small sub-bands. It distributes the information on orthogonal subcarriers. As the bandwidth of a single sub-carrier is small, the single sub-channels can be seen as if they were flat fading, even in presence of small and large scale fading. The channel frequency response can easily be estimated by using pilot signals. With such estimates the frequency selective propagation effects can be equalized and the transmit signal can be recovered. The block diagram of the signal chain for OFDM can be seen in Fig. 5.11.
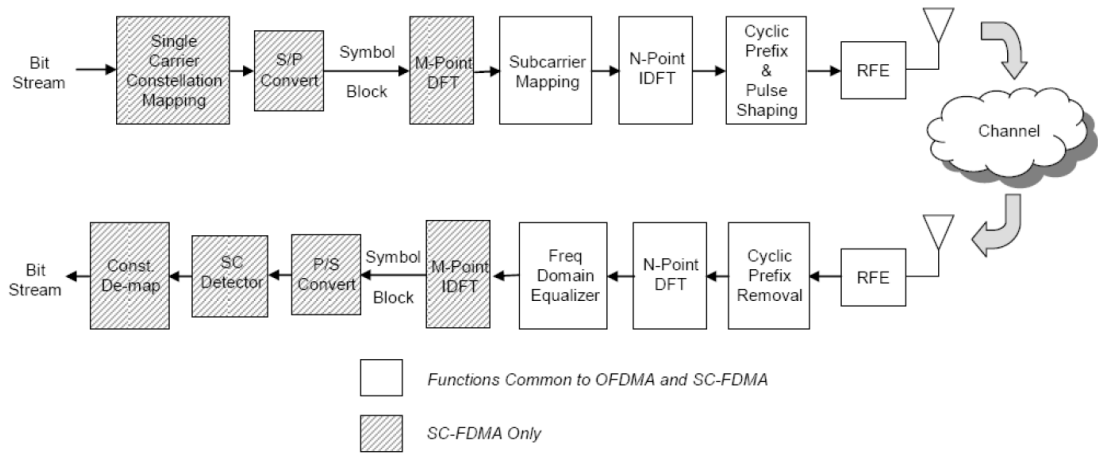
FIGURE 5.11: SC-FDM and OFDM signal chains have a high degree of functional commonality [10]

5.5.2 Single Carrier Frequency Division Multiplexing (SC-FDM)

OFDM multicarrier signals have the drawback of high peak to average power ratio (PAPR), resulting in low efficiencies of the power amplifiers. SC-FDM decreases this drawback by using a regular OFDM system and combining it with precoding based on the Discrete Fourier Transform (DFT). The block diagram is depicted in Fig. 5.11. SC-FDM employs more blocks than OFDM, these blocks are shaded in the figure. Still most of the advantages of OFDM can be used, such as low complexity frequency equalization and frequency domain scheduling. Requirements for power amplifiers can be softened. It is used for the uplink, as efficiency concerns in the UE are even harder than in base stations [12].

5.5.3 Multiple Input Multiple Output (MIMO) transmission

The MIMO antenna technology is a very important technique for the LTE standard. As mentioned in Chap. 2, it can boost the transmission in two ways, either by enhancing the channel capacity or by stabilizing the connection. Four main categories can be distinguished in the LTE transmission modes:

- receive diversity

- transmit diversity

- beam forming

- spatial multiplexing

For diversity transmissions redundant data is transferred on mathematically separated channels. This does not enhance the channel capacity but results in a more robust transmission channel.

The spatial multiplexing mode transmits independent data streams over the antennas, hence it increases the reachable data throughput. The enhancement depends linearly on the number of employed antennas. LTE allows up to four transmit antennas, LTE-A (Long Term Evolution - Advanced) allows up to eight in the downlink case [12].

5.5.4 Turbo Channel Coding

The concept of *Turbo Codes*, also called *parallel concatenated convolutional codes*, was proposed in 1993 by *Berrou, Glavieux* and *Thitimajshima* and has been deployed in 3G UMTS and HSPA systems. In these systems it is an optional way to enhance performance, while in LTE it is the only channel coding mechanism [11], [12]. Turbo coding allows an impressive throughput performance close to the known physical limit, the Shannon bound.

A turbo encoder is a recursive systematic encoder that uses two parallel recursive convolutional encoders, as shown in Fig. 5.12. An interleaver, which shuffles the input bits in a pseudo random order is placed before the second encoder. The LTE turbo encoders come with many improvements, to make the implementation more efficient. As in previous wireless transmission standards, a *Cyclic Redundancy Check* (CRC) is implemented. This allows the turbo decoder to execute an earlier stop of the iterative sequences, if the CRC routine does not detect anymore errors. This extension reduces the computational complexity.

An algorithm with very good performance close to the theoretical bound predicted by Shannon is known as *turbo decoding algorithm*. It was also proposed by *Berrou et al* in 1993. It is based on the a Posteriori Probability (APP) algorithms, also known as Bahl, Cocke, Jelinek and Raviv (BCJR) algorithm [79] with its derivatives the Logarithmic a Posteriori Probability (APP) and the Max-Log-APP algorithms [11].
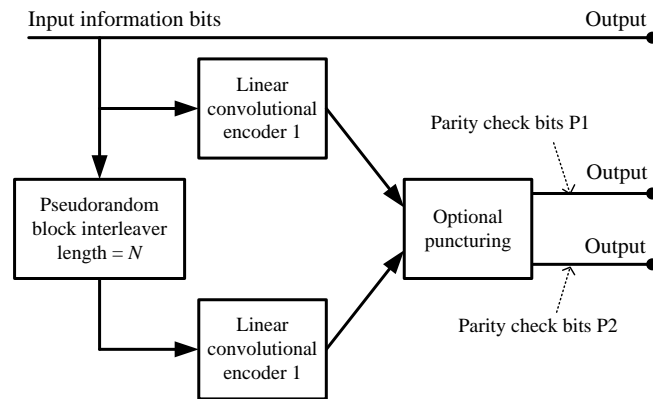
FIGURE 5.12: Encoder for parallel concatenated code (turbo encoder) [11]

5.5.5 Link Adaptation

To provide the best transmission quality to the user (e.g. data throughput, connectivity quality), transmission system parameters can be changed according to the wireless channel state. These parameters are *modulation and coding scheme, numbers of used antennas, transmission mode* and *channel bandwidth.* Seen from a higher perspective, the wireless service provider wants to achieve most efficient resource utilization. Depending on the priority and content of the user, scheduling is done in accordance to the channel parameters [12].

5.5.6 Modeling of the Physical Layer (PHY) for Downlink / Transmitter Side

Figure 5.13 shows a block diagram of an LTE transmitter [12]. User payload is segmented into blocks, then channel coding with *rate matching* is applied. LTE employs turbo coding for channel coding, code blocks are concatenated to create codewords. The user data is *scrambled*, which is an operation, where the user data is convolved with a pseudo random sequence resulting in the scrambled bit stream. One of the reasons for scrambling is that by the use of different sequences in every cell, the neighbour cells interpret the interference as noise.

In the *modulation mapper* the bit stream is mapped to a certain complex *in phase / quadrature phase* (I/Q) modulation scheme, like
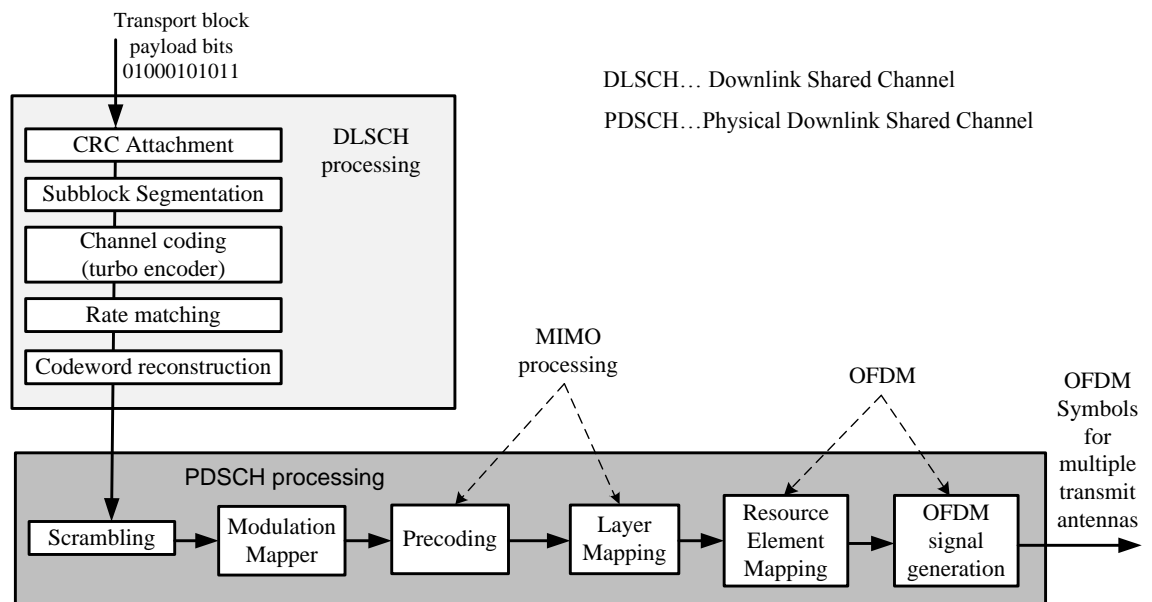
FIGURE 5.13: LTE Signal processing block diagram for transmit diversity and spatial multiplexing (MIMO) [12] in the transmitter

- QPSK (*Quadrature Phase Shift Keying*) - mapping 2 bits to one symbol

- 16QAM (*16 Quadrature Amplitude Modulation*) - mapping 4 bits to one symbol

- 64QAM (*64 Quadrature Amplitude Modulation*). - mapping 8 bits to one symbol

The more bits one symbol contains, the more sensible to noise is the transmission system. The distances between the symbol states in the I/Q constellation diagram become smaller, noise interference can easier deceive the receiver.

In the *MIMO processing* the complex modulated data are shaped for the different MIMO sub-channels according to the available antennas and the transmit mode. The *OFDM* processing takes care of the data placement in the domains frequency and time (*Resource Element Mapping* and *OFDM signal generation*. The data are amplified and transmitted by the multiple antennas.

The receiver takes all these actions back, and delivers the transport block payload bits again.

5.6   Channel Estimation Errors

Another part of the investigations is to have a closer look on **channel estimation errors**. In normal considerations of receiver types like the ICD/ZF or the *Minimum Mean Square Error* Detector (MMSE), it is assumed that the transmission channel is perfectly known. The following investigations also consider imperfect knowledge of the channel taking into account the length of the pilot signals that are used for channel estimation. *Mengali et al* proposed a method to compute the variance of the estimation error for QPSK. The error follows a normal distribution with a first moment equaling zero and variance

$$\sigma^2_{\text{est-err}} = \frac{1}{L} \frac{1}{\epsilon_s/N_0},$$
(5.32)

where L is the length of the pilot sequence [80]. The channel estimation in LTE is executed over 19 OFDM subcarriers and 10 subframes, each containing 2 slots. Every slot contains one symbol for estimation. This results in

$$L = 19 \text{ subcarriers} \times 10 \text{ subframes} \times 2 \text{ slots} \times 1 \text{ symbol} = 380 \text{ symbols}$$
(5.33)

symbols per estimation [4], [75]. With (5.32) and (5.33), the channel estimation error variance $\sigma^2_{\text{est-err}}$ can be calculated as

$$\sigma^2_{\text{est-err}} = \frac{1}{380} \frac{1}{\epsilon_s/N_0}.$$
(5.34)

Equation (5.34) shows the dependency of the estimation error on the symbol energy to noise energy ϵ_s/N_0. The equation is valid for flat fading and time invariant channels. This calculation neglects the fact, that the channel estimation at the edges of the carrier bandwidth window is done with less than 19 subcarrier numbers. However, the author expects that this does not influence the general results.

In case the channel estimation error is present in a simulation, all channel parameters used in the receiver have the Gaussian distributed channel estimation error signal characterized by the variance $\sigma^2_{\text{est\_err}}$ superimposed.

Chapter 6

Decomposition Method Validation - MIMO Channel Capacity Approach

6.1 Validation procedure

The author employs the MIMO channel capacity expression, therefore a generic view can be achieved in the investigations. This approach imposes the use of a receiver of general type working close to or at the Shannon bound. For the shown investigations a 2×2 MIMO transmission system with two uncorrelated data streams and symbol energy of $\epsilon_\mathrm{s}/N_\mathrm{T}$ is chosen. The symbol energy is equally distributed over the two transmission paths. The signal covariance matrix of the symbols

$$\mathbf{R}_\mathrm{ss} = \frac{\epsilon_s}{N_\mathrm{T}} \mathbf{I}_{N_\mathrm{T}} \tag{6.1}$$

is a diagonal matrix in this case [11], where N_T is the number of transmit antennas and ϵ_s/N_0 is the symbol energy to the noise energy (SNR). The sum of the main diagonal elements of $\mathbf{R}_\mathrm{ss}$ is [11]

$$\mathrm{trace}\ \mathbf{R}_\mathrm{ss} = \epsilon_\mathrm{s}\ . \tag{6.2}$$

Using these assumptions, the capacity of the MIMO channel C simplifies to [11]

$$C = \mathscr{E} \left\{ \log_2 \det(\mathbf{I}_{N_\mathrm{R}} + \frac{\epsilon_\mathrm{s}}{N_\mathrm{T} N_0} \mathbf{H} \mathbf{H}^\mathrm{H}) \right\},$$ (6.3)

where N_R is the number of receiving antennas, N_T is the number of transmitting antennas, $\mathbf{H}$ is the channel matrix, $\mathbf{H}^\mathrm{H}$ is the hermitian transposition of the channel matrix $\mathbf{H}$, the *trace* function denotes the sum of the main diagonal elements of a matrix, $\mathbf{I}_{\mathbf{N_R}}$ the identity matrix with dimension $N_\mathrm{R} \times N_\mathrm{R}$, $\mathscr{E}$ is the expectation value and det is the determinant, respectively.

The capacity formula can also be expressed in terms of the eigenvalues of $\mathbf{H} \mathbf{H}^\mathrm{H}$ employing the Eigendecomposition [81]

$$C = \mathscr{E} \left\{ \log_2 \det(\mathbf{I}_{N_\mathrm{R}} + \frac{\epsilon_\mathrm{s}}{N_\mathrm{T} N_0} \mathbf{Q} \mathbf{\Lambda} \mathbf{Q}^\mathrm{H}) \right\}$$ (6.4)

where C reduces to the following equation with $\mathbf{\Lambda}$, which contains the non-negative Eigenvalues on its main diagonal [11], [82], due to calculation of the determinant

$$C = \mathscr{E} \left\{ \log_2 \det(\mathbf{I}_{N_\mathrm{R}} + \frac{\epsilon_\mathrm{s}}{N_\mathrm{T} N_0} \mathbf{\Lambda}) \right\}.$$ (6.5)

Using the Eigenvalue matrix $\mathbf{\Lambda}$ and its elements λ_i, the expectation value of the channel capacity can also be written as [82]

$$C = \mathscr{E} \left\{ \sum_{i=1}^{N_\mathrm{R}} log_2 \left(1 + \frac{\epsilon_s}{N_\mathrm{T} N_0} \lambda_i \right) \right\}$$ (6.6)

The Eigenvalues λ_i can be seen as the gain of the separated MIMO channels. The author calculates the expectation value of the channel capacity C (6.3) for the scenarios in Fig. 5.1 for different $\mathbf{H}$:

1. "Overall" transmission scenario Fig. 5.1(a) incorporating the complete transmission chain: $\mathbf{H} = \mathbf{H}_\mathrm{ant} \cdot \mathbf{H}_\mathrm{ch}$

2. "Antenna" transmission scenario (Fig. 5.1(b)): $\mathbf{H} = \mathbf{H}_\mathrm{ant} = \begin{bmatrix} h_\mathrm{ant,11} & h_\mathrm{ant,12} \\ h_\mathrm{ant,21} & h_\mathrm{ant,22} \end{bmatrix}$

3. "Channel" transmission scenario (Fig. 5.1(c)) incorporating a complex normal distributed channel matrix: $\mathbf{H} = \mathbf{H}_\mathrm{ch} = \begin{bmatrix} h_\mathrm{ch,11} & h_\mathrm{ch,12} \\ h_\mathrm{ch,21} & h_\mathrm{ch,22} \end{bmatrix}$

4. "Baseline" transmission scenario (Fig. 5.1(d)): $\mathbf{H} = \begin{bmatrix} 1 & 0 \\ 0 & 1 \end{bmatrix}$

The channel capacity of the "Overall" transmission system capacity (Fig. 5.1(a)) is

$$C_{\mathrm{oa}} = \mathscr{E}\left\{\log_2 \det(\mathbf{I}_{N_{\mathrm{R}}} + \frac{\epsilon_{\mathrm{s}}}{N_{\mathrm{T}}N_0}\mathbf{H}_{\mathrm{oa}}\mathbf{H}_{\mathrm{oa}}^{\mathrm{H}})\right\}. \tag{6.7}$$

The channel capacity of the "Baseline" transmission system (Fig. 5.1(b)) is

$$C_{\mathrm{bl}} = \mathscr{E}\left\{\log_2 \det(\mathbf{I}_{N_{\mathrm{R}}} + \frac{\epsilon_{\mathrm{s}}}{N_{\mathrm{T}}N_0}\mathbf{H}_{\mathrm{bl}}\mathbf{H}_{\mathrm{bl}}^{\mathrm{H}})\right\}. \tag{6.8}$$

The channel capacity of the "Antenna" transmission system (Fig. 5.1(c)) is

$$C_{\mathrm{ant}} = \mathscr{E}\left\{\log_2 \det(\mathbf{I}_{N_{\mathrm{R}}} + \frac{\epsilon_{\mathrm{s}}}{N_{\mathrm{T}}N_0}\mathbf{H}_{\mathrm{ant}}\mathbf{H}_{\mathrm{ant}}^{\mathrm{H}})\right\}. \tag{6.9}$$

The channel capacity of the "Channel" transmission system (Fig. 5.1(c)) is

$$C_{\mathrm{ch}} = \mathscr{E}\left\{\log_2 \det(\mathbf{I}_{N_{\mathrm{R}}} + \frac{\epsilon_{\mathrm{s}}}{N_{\mathrm{T}}N_0}\mathbf{H}_{\mathrm{ch}}\mathbf{H}_{\mathrm{ch}}^{\mathrm{H}})\right\}. \tag{6.10}$$

The author chooses to investigate the Decomposition Method from the view point of *MIMO channel capacity* as it delivers a very generic sight, as the use of a general receiver type working close to or at the Shannon bound is assumed.

The Decomposition Method is applied as shown in Chap. 4.2.4.1. The symbol energy versus the noise energy $\epsilon_{\mathrm{s}}/N_0$ is a function of the channel capacity C, where the application of the Decomposition Method leads to

$$\left.\frac{\epsilon_{\mathrm{s}}}{N_0}\right|_{C_{\mathrm{dc,log}}} = \left.\frac{\epsilon_{\mathrm{s}}}{N_0}\right|_{C_{\mathrm{ant,log}}} + \left.\frac{\epsilon_{\mathrm{s}}}{N_0}\right|_{C_{\mathrm{ch,log}}} - \left.\frac{\epsilon_{\mathrm{s}}}{N_0}\right|_{C_{\mathrm{bl,log}}}. \tag{6.11}$$

The subscript $_{log}$ denotes logarithmic values. The deviation d is calculated by

$$d = \left.\frac{\epsilon_{\mathrm{s}}}{N_0}\right|_{C_{\mathrm{dc,log}}} - \left.\frac{\epsilon_{\mathrm{s}}}{N_0}\right|_{C_{\mathrm{oa,log}}}. \tag{6.12}$$

Ideally the deviation $d = 0$. In general this goal can be reached with small limitations.

The following graphs (Fig. 6.1, Fig. 6.2, Fig. 6.3) exhibit the channel capacity C versus $\epsilon_{\mathrm{s}}/N_0$ for different channel condition numbers ($\kappa \in \{0\,\mathrm{dB}, 10\,\mathrm{dB}, 40\,\mathrm{dB}\}$). In general, the

channel capacity C rises with increasing ϵ_s/N_0. In theory, the channel capacity C does not have a limit, as long as ϵ_s/N_0 is rising. In practical systems the throughput will always saturate at the maximum data rate related to the chosen modulation and coding scheme of a wireless transmission. Figure 6.1, Fig. 6.2 and Fig. 6.3 show, that the Decomposition Method result does not deviate at $\kappa = 0$. The deviation d is increasing with rising κ and is also depending on the symbol to noise energy ϵ_s/N_0.
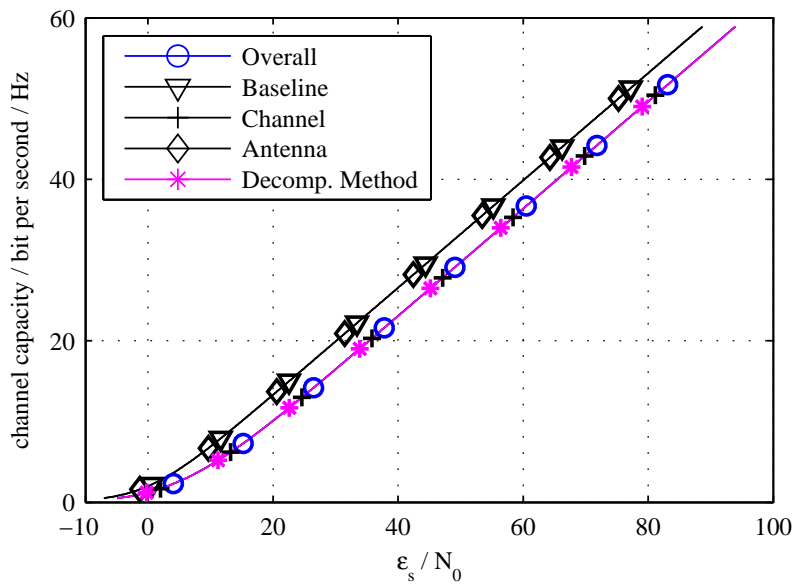

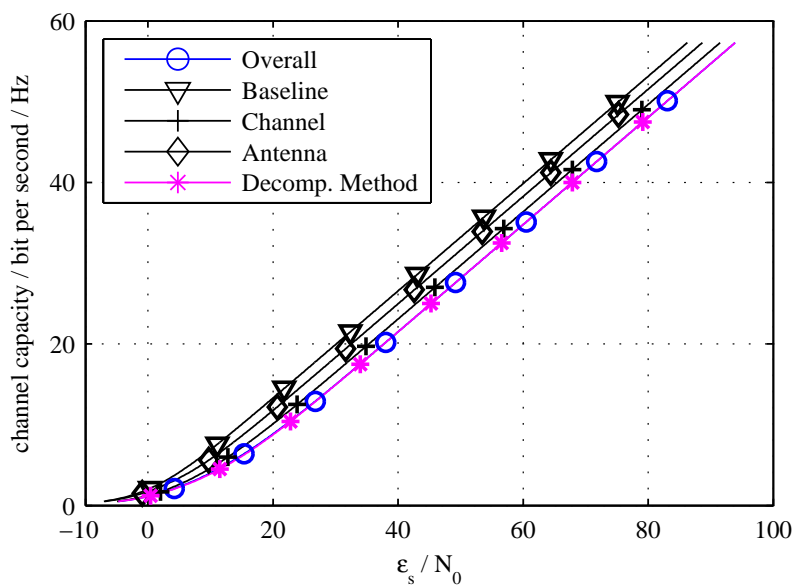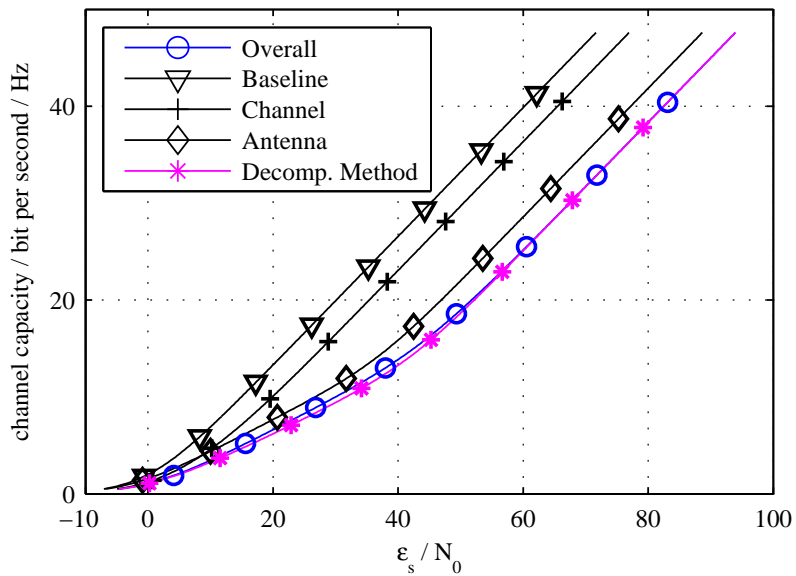FIGURE 6.1: Channel capacity vs. ϵ_s/N_0 using decomposition method; $\kappa_{\mathbf{H}_{\mathrm{ant}}} = 0\,\mathrm{dB}$

FIGURE 6.2: Channel capacity vs. ϵ_s/N_0 using decomposition method; $\kappa_{\mathbf{H}_{\mathrm{ant}}} = 10\,\mathrm{dB}$

FIGURE 6.3: Channel capacity vs. ϵ_s/N_0 using decomposition method; $\kappa_{\mathbf{H}_\mathrm{ant}} = 40\,\mathrm{dB}$
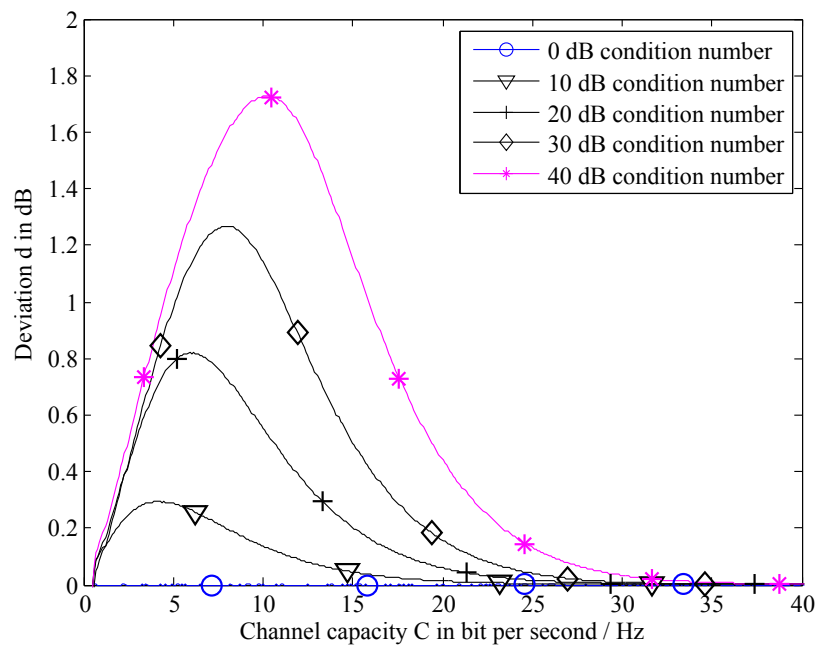
FIGURE 6.4: Channel capacity vs. ϵ_s/N_0 using Decomposition Method; $\kappa_{\mathbf{H}_\mathrm{ant}} = 40\,\mathrm{dB}$

For better visibility, the deviation d versus the channel capacity C is depicted in Fig. 6.4. The plots show d over C for $\kappa \in \{0\,\mathrm{dB}, 10\,\mathrm{dB}, 20\,\mathrm{dB}, 30\,\mathrm{dB}, 40\,\mathrm{dB}\}$. For $\kappa = 0\,\mathrm{dB}$, the deviation d is zero, the Decomposition Method works perfectly. For rising κ, d is increasing and the maximum of d shifts towards bigger ϵ_s/N_0 and decreases slower than at lower values of κ. Nevertheless, even at a very bad conditioned antenna matrix with $\kappa = 40\,\mathrm{dB}$, the maximum deviation d is below $1.72\,\mathrm{dB}$.

6.2   Conclusion

The author validates the Decomposition Method by using the MIMO channel capacity formula. MIMO channel capacity curves are simulated and overlayed using the Decomposition Method. This chapter compares the "Overall" results to the "Decomposition Method" results by showing the occuring deviations d. For the given antenna condition numbers the Decomposition Method works within the error margin given in Fig. 6.4. This error margin of d lies in the error margin given by measurement uncertainties in practical OTA measurements [83]. Dozens of measurement uncertainty sources are listed in [84], [85]: mismatch of transmitter chain, insertion loss of transmitter chain, influence of the probe antenna, uncertainty of BSE power level, statistical uncertainty of throughput measurement, fading flatness within the LTE band, uncertainty of the network analyzer, instability of cable connections just to name a few.

Chapter 7

Decomposition Method Validation - Numerical Analysis Approach

7.1   Introduction

To validate the Decomposition Method from another perspective, the author chooses the numerical link level simulation of a wireless MIMO transmission system. The Decomposition Method is intended for testing general UEs employing MIMO antenna technology. An important point is to investigate the validity of the Decomposition Method for the use with LTE devices. It will be a main application of the method. As the number of employed signal processing elements for LTE is high, this thesis focuses on the most important blocks of the transmission in the PHY layer for the simulation and numerical validation.

The author employs the block diagrams introduced in Chap. 5.3 for the numerical simulation of the transmission. He discusses the results of this transmission system and presents the validation of the Decomposition Method under the given conditions.

7.2 Concept of the Numerical Simulations

As LTE is a complex transmission protocol containing a lot of different functionality blocks, it is necessary to focus on the blocks that might be influential on the Decomposition Method. All investigations are done with flat fading wireless transmission channels. If problems show up already with the simple model of flat fading channels, all scenarios containing more complex transmission models including tapped delay channel models and OFDM schemes will also have a problem.

A wireless system employing an OFDM scheme, splits the complete channel bandwidth of the frequency dependent channel in many narrow-band channels that are assumed to be of flat fading nature. In the following investigations, the author deals with one of these small flat fading OFDM channels. This has the consequence, that it is not necessary to simulate all the OFDM channels. All steps in the DLSCH block (Fig. 5.13) are implemented, as well as the *modulation mapper* and the *MIMO processing blocks*. The elements in the *Physical Downlink Shared Channel* (PDSCH) like scrambling, RE mapping and OFDM processing have been omitted, as the author expects minor influence on the results when employing frequency flat transmission channels.

7.3 Simulation Setup Configuration and Figures of Merit

The parameters for the simulation setup and the necessary figures of merit (FOM) are introduced in this section, as well as how they can be calculated. The block diagrams of the transmission systems in Chap. 5.3 ease the understanding of the parameters and the FOMs.

Transmission Data Block Size and Subframe Error Rate (SFER)

The transmitted data streams have a length of 2^8 bits per realization of the channel matrix $\mathbf{H}_{\text{ant}}$. The transmitted (TX) bit stream is compared to the received bit stream (RX). This is done with a test window size of 2^4 bits, so-called *subframes* (SF). If the RX subframe completely matches the TX subframe, it is recognized as correct. If there are one or more bits wrong, the complete subframe is rated to be incorrect. The mathematical formulation of the Subframe Error Rate (SFER) is

$$\text{SFER} = \frac{\text{number of correctly received SF}}{\text{number of all transmitted SF}} \tag{7.1}$$

it ranges from 1 (no subframe transmitted correctly) to 0 (all subframes transmitted correctly).

Relative Throughput (RTP)

The relative throughput is calculated by subtracting the SFER from 1.

$$\text{RTP} = 1 - \text{SFER} \tag{7.2}$$

It ranges from 0 (no subframe transferred correctly) to 1 (all data transferred correctly).

Downlink Power, Bandwidth and Noise

The downlink power used for the simulation ranges from -130 dBm to -50 dBm. It is always related to a subcarrier bandwidth of 15 kHz.

The noise signals are added after the antenna matrices. Noise energies are always related to the channel bandwidth (15 kHz). The noise figure of the UE was assumed to be 5.2 dB, as this is a characteristic number of a user equipment employed in the CTIA round robin measurement campaign.

Simulation Parameters and Number of Realizations

The numerical simulations employ a variation of settings:

1. Detector type: ICD/ZF or MMSE

2. Ideal or non-ideal channel estimation

3. DLSCH processing enabled / disabled

4. Low, medium or high correlation matrices $\mathbf{H}_\alpha$ and $\mathbf{H}_\beta$

5. Receive antenna condition number κ

The author employed the block diagrams in Chap. 5.3.1 for the simulations without DLSCH processing, and the block diagrams in Chap. 5.3.2 for simulations with DLSCH processing.

A *realization* is a certain transmission system instance employing one set of stochastic parameters, like channel parameters or channel estimation errors. The author executed all simulations with 5000 realizations of the channel matrix $\mathbf{H}_{\mathrm{ch}}$, allowing that the results lie within a confidence interval with reasonable limits. He averaged the throughput of all realizations linearly for each downlink power value throughout this thesis. This averaged throughput is displayed in the result throughput vs. downlink power curves.

Every realization employs a new set of transmission data blocks, where every block contains with 2^4 bits. In total, 2^8 bits are simulated.

The simulation assumes flat fading channels with a bandwith of $15\,\mathrm{kHz}$ and a noise figure of the UE of $5.2\,\mathrm{dB}$.

7.4 Results

7.4.1 Relative Throughput vs. Downlink Power Curves

Figure 7.1 exhibits an example for a set of simulation result curves with relative throughput over downlink power. The mentioned result figure employs an antenna condition numbers of $\kappa = 40\,\mathrm{dB}$ and other different transmission parameters, as mentioned in the caption of the figures.

The examplarily taken graph shows all three necessary curves to calculate the "Decomposition Method" result: the "Baseline", "Channel" and "Antenna" curves. The "Decomposition Method" result and the "Overall" result are also depicted. If the Decomposition Method works well within the given parameters, the "Decomposition Method" result and the "Overall" result overlap, as it is the case in Fig. 7.1. The quantitative measure how well the Decomposition Method works, is the deviation d. It shows the difference between the actual value ("Decomposition Method" result) and the ideal value ("Overall" result)

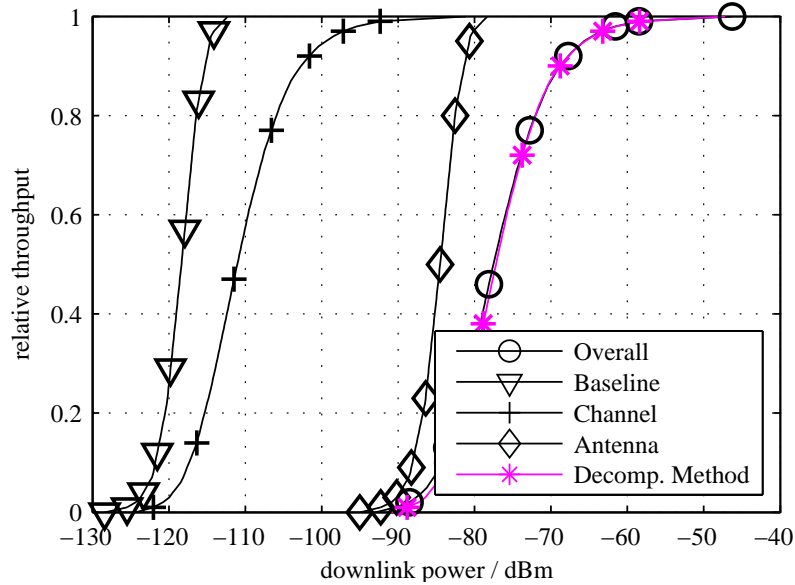$$d = P_{\mathrm{dc,log}}(y) - P_{\mathrm{oa,log}}(y) \tag{7.3}$$

FIGURE 7.1: Simulation result example: downlink power versus relative throughput; ICD/ZF receiver, DLSCH processing on, ideal channel estimation, correlation low, antenna condition number 40 dB

The author simulated the different transmission scenarios for a wide range of parameters. For the compactness of the thesis he shifted the result figures to Appendix 4. Nevertheless, the discussion of them will take place here.

All figures show the same "Baseline" result curve, which exhibits the best performance a transmission system can reach. The higher the performance, a certain throughput can be received with less downlink power. The BSE is directly connected to the receiver (Fig. 5.3). The slope of the "Channel" curve is less steep in comparison to the "Baseline" curve, because of the complex normal distribution of the channel parameters.

In the case that the receiving antenna matrix is unity and uncorrelated ($\kappa = 0\,\mathrm{dB}$), the "Antenna" result overlaps with the "Baseline" result (e.g. Fig. A.1(a)). The block diagram for the "Antenna" simulations is shown in Fig. 5.4. The overlapping of the "Overall" curve and the "Decomposition Method" curve is the ideal case, the Decomposition Method works perfectly. As the antenna elements starts to be correlated (condition number κ of the antenna matrix $\mathbf{H}_{\mathrm{ant}} > 0\,\mathrm{dB}$), the receiver performance is degraded. This degradation leads to a result curve (the "Antenna" result curve) that is a right shifted version of the "Baseline" result curve, as shown in Fig. 7.1. This right-shift means that the receiver needs more signal downlink power to reach the same throughput as with an uncorrelated channel. The reason for this behavior is that the receiver cancels the influence of the channel, but it also enhances the existing intrinsic noise,

generated by the RF frontend of the UE. The more the receiving antennas are coupled, the worse is the conditioning of the antenna matrix (indicated by κ).

Looking at Fig. 7.1, the antenna matrix condition number $\kappa = 40\,\text{dB}$. For a relative throughput of 0.7, the "Baseline" setup needs a downlink power of $-117\,\text{dBm}$, while the "Antenna" setup needs $-83\,\text{dBm}$, which is a difference of $34\,\text{dB}$. So to say, the degradation through the correlation of the receiving antennas results in a degraded performance of the whole transmission system.

All simulation results with the variation of parameters is shown in Appendix A by graphs and a result summary table. The influence of the different simulation parameters will be discussed in the following section.

7.4.2 Influence of the Transmission System Parameters on the Deviation d

The author shows the influence of the simulation parameters on the deviation d. These results are exhibited in the following graphs and the author will discuss them elaborately. The different simulation parameters are

- DLSCH processing on/off

- Ideal/non-ideal channel estimation

- Low, medium and highly correlated channel parameters

The figures Fig. 7.2 - Fig. 7.8 show the investigation of the deviation d versus the antenna condition number κ for this set of parameters. They are arranged in different ways to highlight certain ways of behaviour. Certain curves are exemplarily taken to explain a certain way of behaviour. Some facts are mentioned twice, to ease to understandability. Please note that the depicted deviations d are *maximum* values that will not be reached in practice, when a real antenna system is employed.

Influence of the Condition Number κ

Generally speaking, the absolute deviation $|d|$ rises with rising antenna condition number κ. Figure 7.2 is taken exemplarily to show this behaviour, which appears in all simulations. The absolute deviation starts to grow rapidly and settles more or less at $\kappa = 20\,\text{dB}$. The employed simulation parameters for the deviation results in Fig. 7.2 for are: DLSCH processing on, non-ideal channel estimation; low, medium and high channel correlation; ICD/ZF and MMSE receiver.
It is interesting to see that the Decomposition Method works almost perfectly for low correlation and the ICD/ZF receiver. In comparison, the MMSE receiver causes an approximate maximum deviation $d = -1\,\text{dB}$ at low correlation. With rising correlation, both receiver types, MMSE and ICD/ZF, cause bigger absolute deviation $|d|$. The value of $|d|$ is greater for MMSE than for ICD/ZF in general.
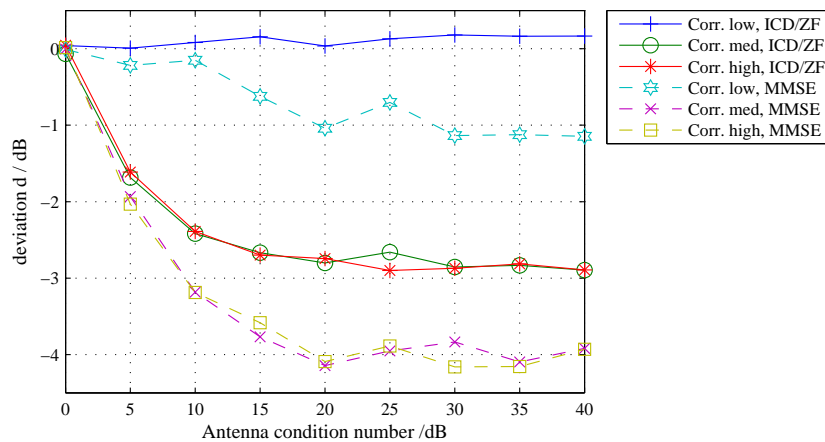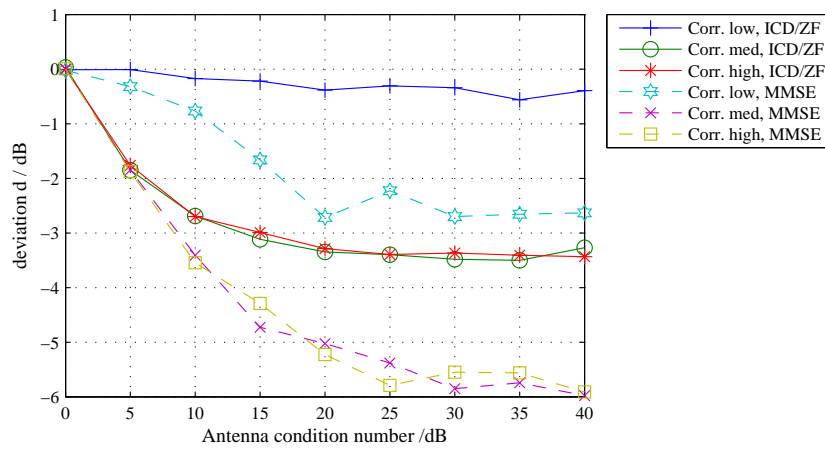
FIGURE 7.2: Deviation d versus antenna condition number for DLSCH processing on, non-ideal channel estimation; low, medium and high channel correlation; ICD/ZF and MMSE receiver
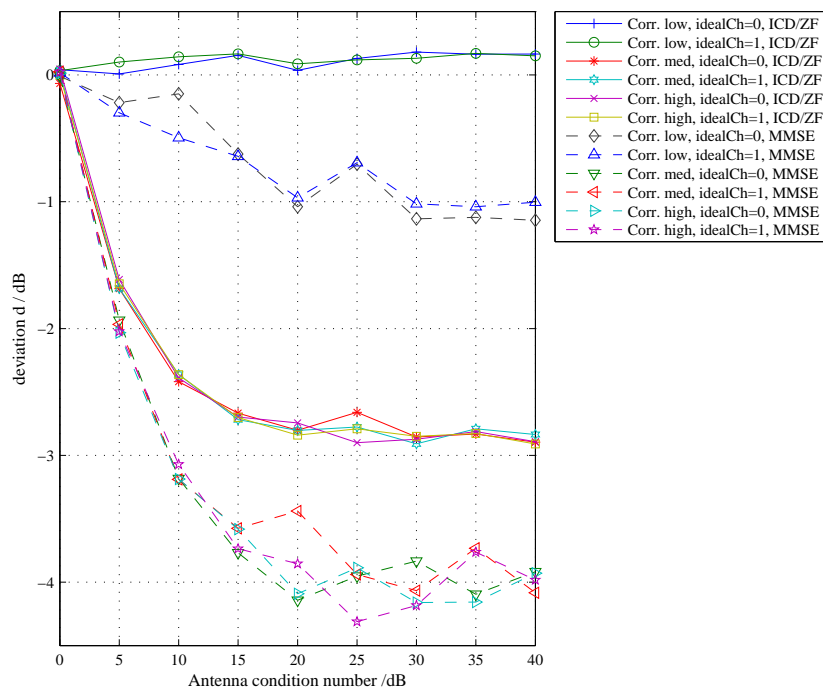
Influence of the Channel Correlation

Figure 7.2 also points out the differences of the different channel correlations *low, medium* and *high*. DLSCH processing is applied and the channel estimation is non-ideal. The Decomposition Method works almost perfect for ICD/ZF receivers at low correlations. In contrast, the receiver Type MMSE delivers mentionable deviations already at low channel correlations. As soon as channel correlation becomes medium or high, the absolute deviation $|d|$ increases. The deviation $|d|$ is always bigger for the MMSE receiver than for the ICD/ZF receiver.

Figure 7.3 shows the same trends but with higher absolute deviation $|d|$ (no DLSCH processing is applied).

Influence of Ideal / Non-Ideal Channel Estimation

The author exhibits the results for simulations employing non-ideal channel estimation (Fig. 7.3) in comparison to ideal channel estimation (Fig. 7.4). The LTE pilot sequence length is long enough for a stable and exact channel estimation process. It is interesting to see that for all correlations the absolute deviation $|d|$ is smaller for ICD/ZF receiver than for MMSE receivers. The used parameters are low, medium and highly correlated channel, MMSE and ICD/ZF receiver. Simulations with non-ideal and ideal channel estimations deliver similar results. The similarity between the results of non-ideal and ideal channel estimation holds for all parameter sets, as depicted in Fig. 7.5 and Fig.

FIGURE 7.3: Deviation d versus antenna condition number for DLSCH processing off, non-ideal channel estimation; low, medium and high channel correlation; ICD/ZF and MMSE receiver
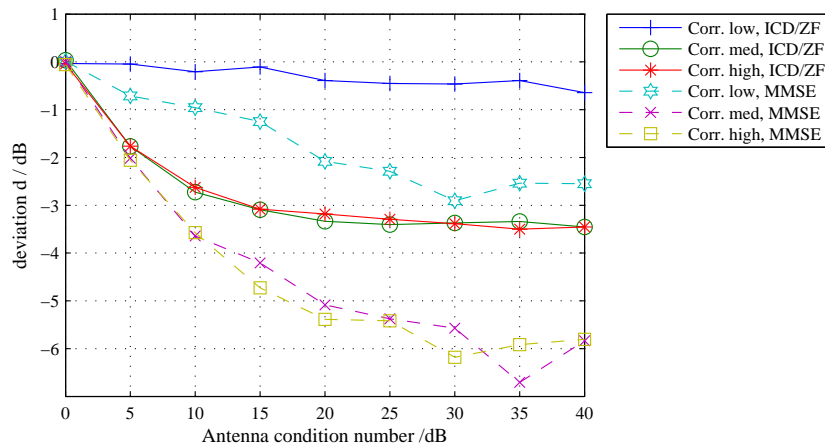
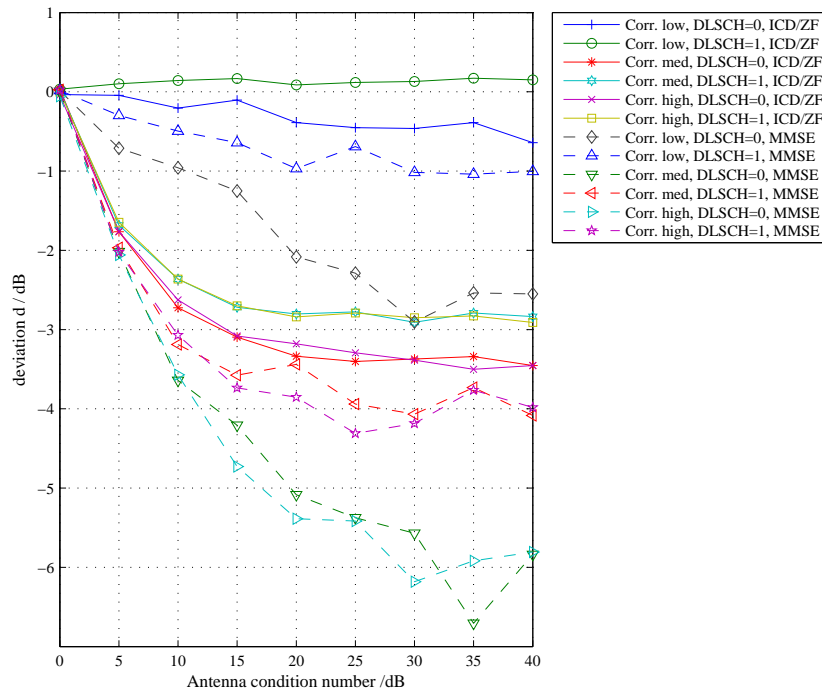

FIGURE 7.4: Deviation d versus antenna condition number for DLSCH processing off, ideal channel estimation; low, medium and high channel correlation; ICD/ZF and MMSE receiver

7.6. Figure 7.5 exhibits the deviation d for transmission system with DLSCH processing turned off, and Fig. 7.6 for DLSCH processing turned on.

The effect of the channel estimation error on the system is negligible, as the employed pilot sequence length of $L = 380$ is long enough for good channel estimation.
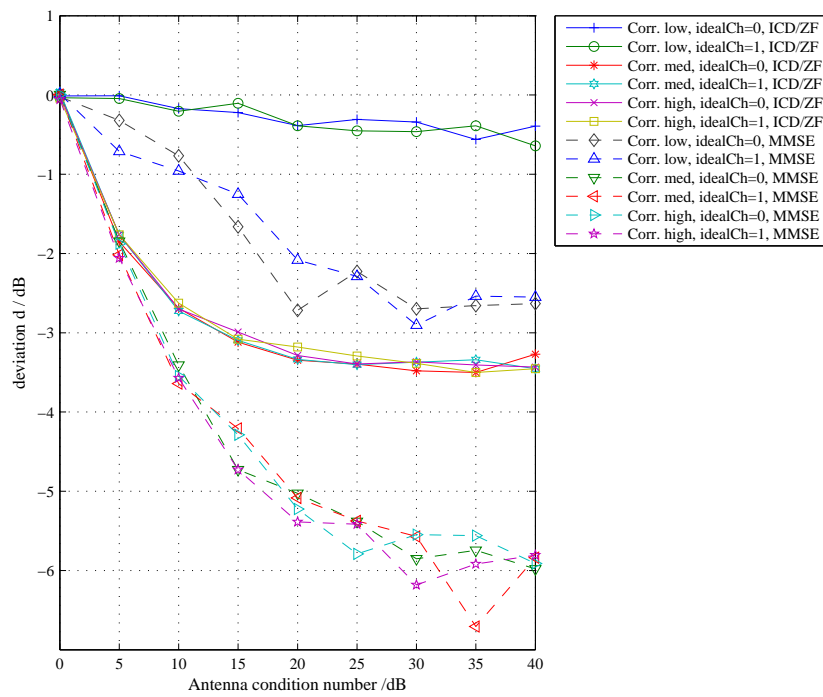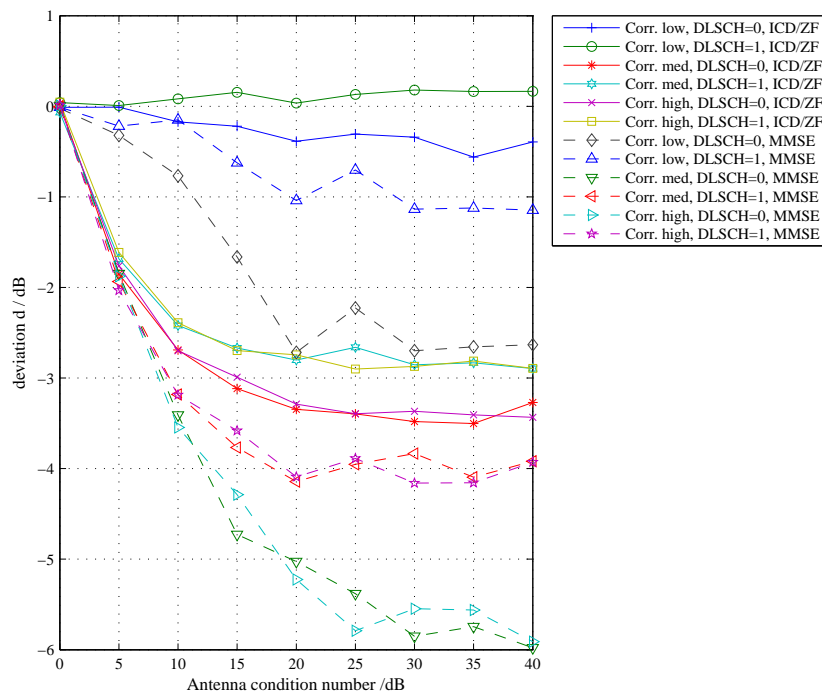
FIGURE 7.5: Deviation d versus antenna condition number for DLSCH processing off, non-ideal/ideal channel estimation; low, medium and high channel correlation; ICD/ZF and MMSE receiver

FIGURE 7.6: Deviation d versus antenna condition number for DLSCH processing on, non-ideal/ideal channel estimation; low, medium and high channel correlation; ICD/ZF and MMSE receiver

Influence of DLSCH processing on / DLSCH processing off

Figure 7.7 depicts the differences of the deviation D, between DLSCH processing being turned on and off for ideal channel estimation. The channel correlations are again low, medium and high. In contrast, Fig. 7.8 exhibits the results for DLSCH processing being turned on and off for non-ideal channel estimations.

FIGURE 7.7: Deviation d versus antenna condition number for DLSCH processing on/off, ideal channel estimation; low, medium and high channel correlation; ICD/ZF and MMSE receiver

The main message of both graphs is that if DLSCH processing is turned on, the abs. deviation $|d|$ becomes smaller for all three correlation types and two receiver types (MMSE and ICD/ZF), in comparison to DLSCH processing turned off. This is true for all channel correlation types: low, medium and high. This is the reason why the Decomposition Method is very suitable for LTE performance tests, as LTE *always* uses DLSCH processing. The influence of the channel estimation on the results of d is very small.

Summarizing, the following facts can be pointed out:

FIGURE 7.8: Deviation d versus antenna condition number for DLSCH processing on/off, non-ideal channel estimation; low, medium and high channel correlation; ICD/ZF and MMSE receiver

- The Decomposition Method suits well its purpose, the performance testing of MIMO enabled wireless UEs, especially for low correlation channels, it delivers small deviations d for both receiver types: ICD/ZF and MMSE.

- In general, if the antenna condition number κ is rising, the absolute deviation $|d|$ rises.

- If channels correlations are medium or high, the absolute deviation $|d|$ is bigger than for low correlation channels.

- The Decomposition Method delivers better results with the ICD/ZF receiver in comparison to the MMSE receiver for all channel correlations.

- The influence of the channel estimation error is negligible in the case of an LTE pilot sequence length as a reference example.

- If a transmission system employs DLSCH processing, the Decomposition Method performs better as without it. This behaviour makes it very suitable for performance tests with LTE, as it always uses DLSCH processing.

- Rising deviation occurs for antennas with very poor behaviour, but manufacturers will strongly avoid such poor designs as it results in a significantly reduced MIMO system performance.

All diagrams with deviation d versus antenna condition number κ show *maximum* errors, which will not occure in practice. The reason is that the condition number of the antenna matrix $\mathbf{H}_{\mathrm{ant}}$ is different for every constellation. Therefore the author executes investigations with a practical antenna set and the mean deviation $\bar{d}$ in the following chapter.

7.4.3 Investigating the Deviation d Employing LTE Reference Antennas

The deviation d versus condition number κ graphs tend to overestimate practically arising deviations, as UE manufacturers do not intentionally build very poor performing antenna systems. For the reason of better visualization the author investigated the distribution of the deviation d if LTE reference antennas are used.

The company *Motorola Mobility* designed LTE reference antennas for the purpose of inter-laboratory measurement campaigns executed in the COST 1004 actions [13]. The printed circuit board contains the antennas and a metal housing. Different UEs can be placed inside the metal cavity. The UE can be connected to the external reference antenna elements with coaxial cables, the internal antennas are deactivated. A picture of the reference antenna is exhibited in Fig. 7.9.

It is available in three different performance types:

- "Good" performance

- "Nominal" performance

- "Bad" performance
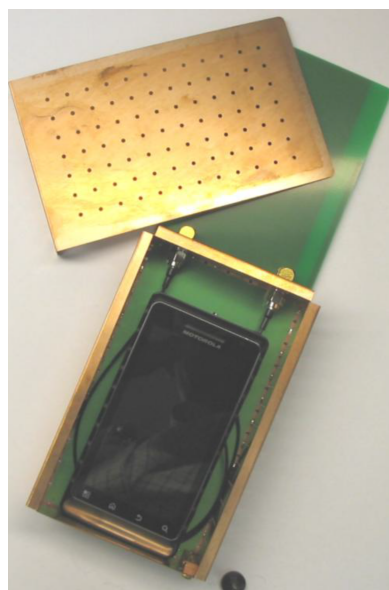
FIGURE 7.9: LTE reference antenna for a UE with two antennas designed by Motorola Mobility for band 13 (751 MHz), with a printed circuit board carrying a closed metal cavity for the UE, two printed antennas and connection cables [13]

The performance naming refers to the coupling of the antenna elements in the different reference antenna versions. This coupling is expressed with condition number κ, which is different for every constellation. A constellation contains test antenna positions and polarizations, as well as UE placement. The author uses the 128 constellations shown in Fig. 4.14 for statistical investigations on the logarithmic antenna condition numbers κ. Every single constellation delivers a certain κ, which can be calculated employing the E-field antenna pattern as shown in Chap. 5.4.2. Figure 7.10 shows the distribution of κ for the 128 constellations for all three antenna types. Also the mean logarithmic value

$$\bar{\kappa} = \frac{\sum\limits_{i=1}^{N} \kappa_i}{N} \tag{7.4}$$

is shown in the graphs, where N is the number of constellations (e.g. $N = 128$), κ_i is the logarithmic antenna condition number of a constellation i.

The reference antennas behave as they are named. Going from "Good" to "Bad", $\bar{\kappa}$ rises:

- "Good" antenna: 15.86 dB

- "Nominal" antenna: 16.6 dB

- "Bad" antenna: 18.72 dB

The table 7.1 summarizes the *mean logarithmic deviations* for the same parameter variation as in Chap. 7.4.2 for a relative throughput of 70 %:

- DLSCH processing on/off

- Ideal/non-ideal channel estimation

- Low, medium and high channel correlations

The mean logarithmic deviation is

$$\bar{d} = \frac{\sum\limits_{i=1}^{N} d_i}{N}, \tag{7.5}$$

where N again is the total number of constellations, and d_i is the deviation at the constellation i. The Decomposition Method can be validated for all three types of antennas
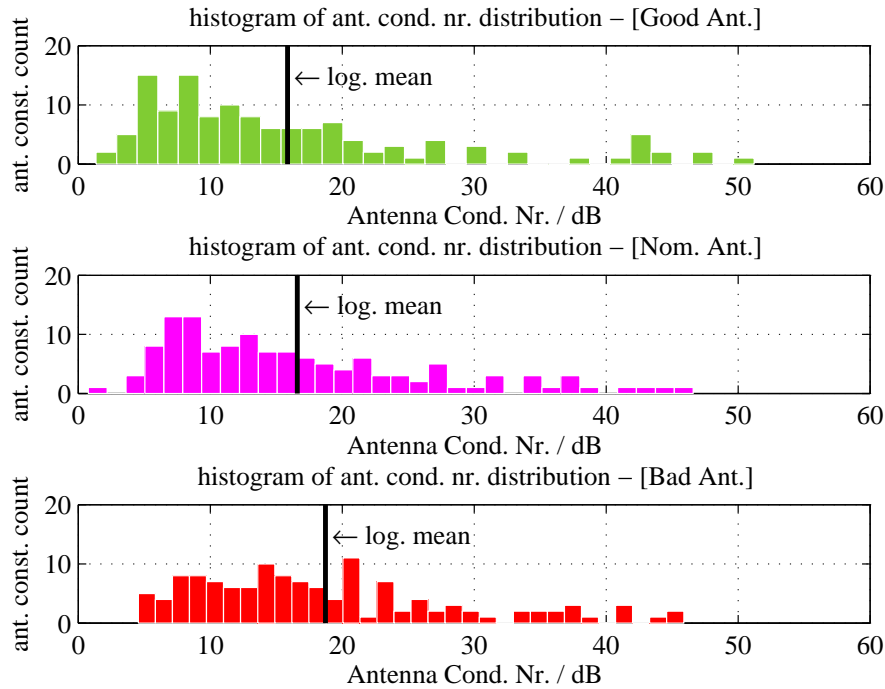
FIGURE 7.10: Distribution of the antenna condition number and mean logarithmic condition number of the "Good", "Nominal" and "Bad" reference antennas

within a $|\bar{d}|$ of 4.69 dB. This maximum of the averaged values of $\bar{d}$ lies below the peak value of $|d|$, as shown in Fig. 7.5. In the case a UE employs LTE, DLSCH processing is always applied. In this case the absolute mean logarithmic deviation $|\bar{d}|$ will always be below 3.57 dB for all antenna condition numbers. If LTE UEs are tested only with low correlation of channels, the method works almost perfectly with $|\bar{d}|$ below 0.29 dB.

The histograms of the deviation d and the mean logarithmic deviations $\bar{d}$ over all constellations for all reference antenna types ("Good", "Nominal" and "Bad") are shown in Appendix B. Table 7.1 exhibits the mean deviations $\bar{d}$ for all parameter variations.

Finally, it can be pointed out that:

- The mean deviation $|\bar{d}|$ is *always* below the maximum of the absolute deviations $|d|$. In the case of ICD/ZF receiver, low correlated channel, DLSCH processing and non-ideal channel measurement even for the "Bad" antenna it will be only 0.1 dB.

- In the practical case of rather well conditioned antenna matrices and DLSCH processing applied, the method works very well.

TABLE 7.1: Mean logarithmic deviations $\bar{d}$ at 70% relative throughput using LTE reference antennas "Good", "Nominal" and "Bad" with parameters: channel correlation type, DLSCH processing, channel estimation

receiver type	corr.	DLSCH proc.	ch. est.	deviation $\bar{d}$ for ref. ant. /dB		
				"Good"	"Nominal"	"Bad"
ICD/ZF	low	off	ideal	-0.26	-0.26	-0.29
ICD/ZF	low	off	non-ideal	-0.19	-0.23	-0.26
ICD/ZF	low	on	ideal	0.12	0.13	0.13
ICD/ZF	low	on	non-ideal	0.09	0.10	0.10
ICD/ZF	med	off	ideal	-2.73	-2.86	-3.02
ICD/ZF	med	off	non-ideal	-2.71	-2.86	-3.02
ICD/ZF	med	on	ideal	-2.37	-2.47	-2.59
ICD/ZF	med	on	non-ideal	-2.38	-2.47	-2.58
ICD/ZF	high	off	ideal	-2.67	-2.81	-2.96
ICD/ZF	high	off	non-ideal	-2.69	-2.82	-2.98
ICD/ZF	high	on	ideal	-2.37	-2.47	-2.59
ICD/ZF	high	on	non-ideal	-2.36	-2.47	-2.59
MMSE	low	off	ideal	-1.39	-1.49	-1.65
MMSE	low	off	non-ideal	-1.39	-1.52	-1.77
MMSE	low	on	ideal	-0.61	-0.64	-0.71
MMSE	low	on	non-ideal	-0.53	-0.56	-0.66
MMSE	med	off	ideal	-3.82	-4.14	-4.46
MMSE	med	off	non-ideal	-3.90	-4.14	-4.51
MMSE	med	on	ideal	-3.13	-3.26	-3.43
MMSE	med	on	non-ideal	-3.18	-3.37	-3.58
MMSE	high	off	ideal	-4.00	-4.27	-4.63
MMSE	high	off	non-ideal	-3.9	-4.14	-4.49
MMSE	high	on	ideal	-3.2	-3.36	-3.57
MMSE	high	on	non-ideal	-3.17	-3.36	-3.55

- Comparing the receiver types, the MMSE receiver causes higher mean deviations $\bar{d}$ than the ICD/ZF receiver.

- The investigations exhibit that the mean deviation $\bar{d}$ decreases when going from antenna type "Bad"' to "Good".

- If a very poor antenna systems is measured, there is a possibility of calibrating the system, as the deviation d is static. The author shows this process in Chap. 7.4.4.

- The Decomposition Method is an innovative method to deliver fast and reliable performance test results.

7.4.4 Calibration/Error Correction Procedure

In practice, as the wireless equipment manufacturers will try to design MIMO antennas for the UE with lowest possible correlation, the Decomposition Method works with sufficient precision, as there are many sources of other measurement uncertainties (see Chap. 6.2). Nevertheless, it is also possible to perform an error compensation for deviation-free results. The deviation d and mean logarithmic deviation $|\bar{d}|$ are static values, depending mainly on four things:

- DLSCH processing is used or not?

- Which channel model and channel correlation is used?

- Which receiver type is used?

- Which antenna condition number is present in the actually measured constellation?

An error correction term can be calculated, because all parameters are known from the measurement settings, only the antenna condition number can be a little bit more tricky. The reason is that the antenna system of a UE has to be accessible by RF ports. It is important for the error correction to know the antenna condition number. Therefore the antenna patterns of all constellations have to be known. The patterns can be measured in two ways:

- The antennas are accessible by physical ports: the antenna patterns can easily be measured for all constellations with a vector network analyzer

- The antennas are not accessible: the UE has to provide a measurement mode for providing its antenna parameters in amplitude and phase

The user is able to determine the error correction term to employ the Decomposition Method results without any deviation.

The deviation d_i has to be calculated for every constellation i. The variable $i = \{1, ..., N\}$ denotes the actual constellation, N is the total number of constellations. The error term, the deviation d_i in logarithmic terms, has to be subtracted from all Decomposition Method results $P_{\mathrm{dc},i,\log}(y)$ for every constellation. The corrected result is

$$P^c_{\mathrm{dc,i,log}}(y) = P_{\mathrm{dc},i,\log}(y) - d_i \ . \tag{7.6}$$

The corrected values $P^c_{\mathrm{dc,i,log}}(y)$ can be employed to calculate the averaged performance result.

Chapter 8

Validation of the Decomposition Method by OTA Measurements of a UE

8.1 Measurements

This thesis originates from a cooperation with our industrial partner Rohde & Schwarz. Our partners conducted measurements with a commercial LTE device, namely the *Sony Xperia* smart-phone, for a round-robin campaign for *radio area network group 4* (RAN4) of 3GPP. They tested the UE in an anechoic chamber using the "Good" antenna, employing the setup in Chap. 4.2.4.2 at 128 constellations [86]. They placed the UE in the center of the quiet zone. This is a certain volume in the anechoic chamber, where the operator has to place the UE he wants to test. Ideally, the anechoic chamber does not have reflections at all. In practice, some do exist. The quiet zone defines the volume where the reflections are below a certain level. The partners at Rohde & Schwarz measured the "Decomposition Method" results and the "Overall" results of the Sony Xperia smartphone with different transmission channel models than in the simulation to calculate the deviation d.

Figure 8.1 show the experimental results of the distribution of the deviation d. The partners of the author determined the deviation d for the different transmission channel

models for all 128 constellations. The results of d for the different channel models are color coded in the diagram.
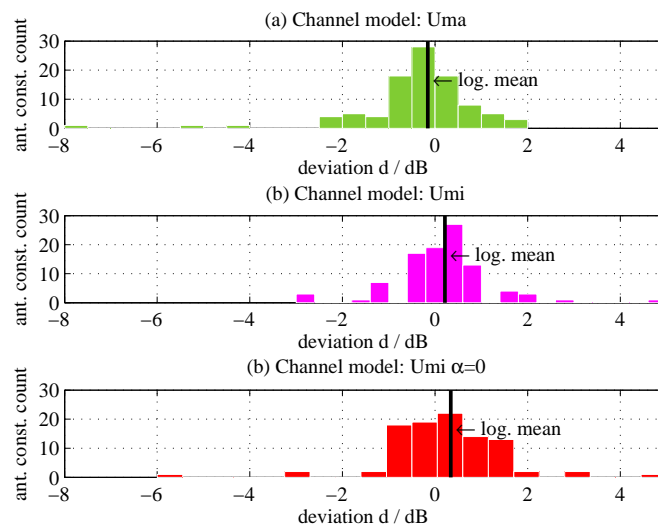
FIGURE 8.1: Distribution of the log. deviations d between the "Decomposition Method" and "Overall" measurement results for different channel models (Uma, Umi, Umi_alpha=0) and different base station correlation coefficient for the smartphone *Sony Xperia* as UE with "Good" reference antenna

The measurement setup employs a full LTE transmission containing tapped delay channel models, OFDM and resource block allocation [7]. These tapped delay models were used: Urban Micro (Umi), Urban Micro (Umi) with all tap correlations $\alpha = 0$ and Urban Macro (Uma). These models are proposed for OTA testing of UEs by 3rd Generation Partnership Project (3GPP) [87].

In comparison to the measurements, the simulations in Chap. 7 use a simplified setup. Nevertheless, a comparison is valid, as the Decomposition Method is validated by simulation for a single OFDM subcarriers that has a bandwidth of 15 kHz, in the LTE case. This narrow bandwidth allows a treatment of the channel as frequency flat fading ones. The Decomposition Method is validated for the smallest element, the single OFDM channel. Therefore it is also valid for the complete fading channel, which consists of many small OFDM carriers.

Figure 8.1 points out that the deviation d between the measured "Overall" and "Decomposition Method" results are distributed around a mean values from -0.16 dB to 0.34 dB for all employed channel models, which is very low regarding all other uncertainty sources [84], [85]. The approximately Gaussian shaped distribution of the deviation d is resulting from the mentioned measurement uncertainties.

8.2 Comparison of Measurements to the Simulations

As the partners of the author did the measurements in Chap. 8.1 with a slightly different set of parameters as proposed by 3GPP [73], [75], the author presents another set of simulations, as close as possible to the measurements. The channel models presented in Appendix C employ tapped delay models, they were used in the measurements. The taps have different correlation values α, while β is always zero. To be able to use the different correlations of the taps for the simplified model, the author employs a linear power related averaging of α. This averaging results in these values of α:

1. Channel model Uma: $\alpha = 0.1172$ (light correlation)

2. Channel model Umi with ($\alpha = 0$): the mean value also is $\alpha = 0$ (all taps are zero; as defined in Appendix C; uncorrelated)

3. Channel model Umi: $\alpha = 0.9474$ (strong correlation)

Results are summarized in Tab. A.1. The mean deviation $\bar{d}$ is given for the measurements and the closest possible simulations for several channel models. The mean deviation $\bar{d}$ is very close to zero. **So to say, both, simulation results and measurement results (Tab. 8.1), point in the same direction: the validity of the Decomposition Method. The mean value of the deviation d is within the given limits for all employed channel models.**
Appendix C presents all the used parameters for the measurements including the used channel models (*Umi, Umi ($\alpha = 0$)* and *Uma*). The full simulation results are depicted in Appendix B.2.

TABLE 8.1: Comparison of the deviation $\bar{d}$ between measurement and simulations

	deviation $\bar{d}$ in dB for		
Channel model	Measurement Sony Xperia	Simulation ICD/ZF	Simulation MMSE
Uma	-0.16	0.1	-0.57
Umi	0.21	0.05	-0.43
Umi $\alpha = 0$	0.34	-0.42	-0.52

Chapter 9

Conclusion

This thesis covers performance testing of Multiple Input Multiple Output (MIMO) enabled wireless user equipment. It is divided into two parts. The first part deals with performance investigations for MIMO antenna systems employing scattering parameters. An antenna system using two planar Long Term Evolution (LTE) reference antennas is investigated towards its Envelope Correlation Coefficent (ECC). This figure of merit can be quantified using normal laboratory equipment like vector network analyzers. A base station emulator is not necessary.

The second part of the thesis deals with Over The Air (OTA) performance tests for complete MIMO enabled User Equipment (UE), including antennas, front-end and algorithmic performance. The author emblazes different methods and investigates a very promising one, the Decomposition Method. This powerful method splits the performance tests into two parts: a static test for the antenna performance and a faded test for the algorithmic performance. The results from the separated measurements are combined and deliver accurate and repeatable results. By applying this split, the measurements can be speeded up by a factor of 36 in comparison to the combined measurements.

This thesis deals with the validation of this split of the measurements. The author validates the Decomposition Method by treading two differing paths.

As many MIMO enabled devices also use Orthogonal Frequency Division Multiplexing (OFDM), the single orthogonal frequency bands have small bandwidths. The thesis exploits this fact by simplifying the employed models from generic tapped delay channel models to frequency-flat response channels, without loosing validity.

In the first path, the author employs the channel capacity formulas to reveal the validity of the Decomposition Method in a generic way, with a receiver working close to the Shannon bound. In the second path, he also validates the method by numerical means, simulating a complete transmission system with Kronecker channel models with frequency flat fading. He shows that the applicability of the Decomposition Method is given for most use cases. Low correlated channels deliver an absolute deviation of the Decomposition Method result lower than $0.7\,\mathrm{dB}$. For very accurate results in all test cases, the author also proposes a deviation correction method.

To round up the picture, the validity of the method is shown by measurement results for the *Sony Xperia* smartphone. The mean deviation $\bar{d}$ is within the interval { $-0.16\,\mathrm{dB}$ to $0.34\,\mathrm{dB}$}.

This thesis provides a thorough scientific investigation of the Decomposition Method, demonstrating that it is a powerful and quick method to rate the performance of a MIMO enabled wireless UE. The author validates this method that is able to speed up tests by a factor of 36 and still delivers accurate and reliable results with reasonable equipment effort.

Appendix A

Throughput vs. Downlink Power Curves

The result curves for the numerical investigations of the Decomposition Method are given here. The graphs show the relative throughput over downlink power for different parameters:

- Receiver type: ICD/ZF and MMSE

- DLSCH processing on/off

- ideal/non-ideal channel estimation

- different channel correlations

Three types of channel correlation are investigated using the Kronecker channel model (Fig. 5.10):

- "Low" correlation: $\mathbf{H}_\alpha = \begin{bmatrix} 1 & 0 \\ 0 & 1 \end{bmatrix}, \quad \mathbf{H}_\beta = \begin{bmatrix} 1 & 0 \\ 0 & 1 \end{bmatrix}$

- "Medium" correlation: $\mathbf{H}_\alpha = \sqrt{\begin{bmatrix} 1 & 0.3 \\ 0.3 & 1 \end{bmatrix}}, \quad \mathbf{H}_\beta = \sqrt{\begin{bmatrix} 1 & 0.9 \\ 0.9 & 1 \end{bmatrix}}$

- "High" correlation: $\mathbf{H}_\alpha = \sqrt{\begin{bmatrix} 1 & 0.9 \\ 0.9 & 1 \end{bmatrix}}, \quad \mathbf{H}_\beta = \sqrt{\begin{bmatrix} 1 & 0.9 \\ 0.9 & 1 \end{bmatrix}}$

TABLE A.1: Overview of relative throughput vs. downlink power simulations employing different receiver types, correlation grade, DLSCH processing and channel estimation error presence including figure numbers

receiver type	corr.	DLSCH proc.	ch. est. err. present	Fig. number
ICD/ZF	low	off	no	A.1(a), A.1(b), A.2(a)
ICD/ZF	low	off	yes	A.2(b), A.3(a), A.3(b)
ICD/ZF	low	on	no	A.4(a), A.4(b), A.5(a)
ICD/ZF	low	on	yes	A.5(b), A.6(a), A.6(b)
ICD/ZF	med	off	no	A.7(a), A.7(b), A.8(a)
ICD/ZF	med	off	yes	A.8(b), A.9(a), A.9(b)
ICD/ZF	med	on	no	A.10(a), A.10(b), A.11(a)
ICD/ZF	med	on	yes	A.11(b), A.12(a), A.12(b)
ICD/ZF	high	off	no	A.13(a), A.13(b), A.14(a)
ICD/ZF	high	off	yes	A.14(b), A.15(a), A.15(b)
ICD/ZF	high	on	no	A.16(a), A.16(b), A.17(a)
ICD/ZF	high	on	yes	A.17(b), A.18(a), A.18(b)
MMSE	low	off	no	A.19(a), A.19(b), A.20(a)
MMSE	low	off	yes	A.20(b), A.21(a), A.21(b)
MMSE	low	on	no	A.22(a), A.22(b), A.23(a)
MMSE	low	on	yes	A.23(b), A.24(a), A.24(b)
MMSE	med	off	no	A.25(a), A.25(b), A.26(a)
MMSE	med	off	yes	A.26(b), A.27(a), A.27(b)
MMSE	med	on	no	A.28(a), A.28(b), A.29(a)
MMSE	med	on	yes	A.29(b), A.30(a), A.30(b)
MMSE	high	off	no	A.31(a), A.31(b), A.32(a)
MMSE	high	off	yes	A.32(b), A.33(a), A.33(b)
MMSE	high	on	no	A.34(a), A.34(b), A.35(a)
MMSE	high	on	yes	A.35(b), A.36(a), A.36(b)

Table A.1 exhibits the parameter variations for the simulations with the corresponding result figures. Every set of parameters is simulated for an antenna condition number κ of $0\,\mathrm{dB}$ (no antenna correlation), $10\,\mathrm{dB}$ (weak antenna correlation) and $40\,\mathrm{dB}$ (strong antenna correlation). This chapter depicts all result curves for Chap. 7.4.1.
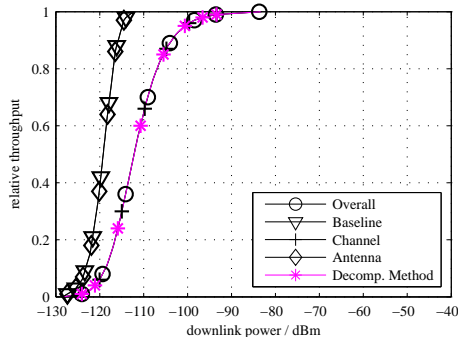
(a) Cond. number $\kappa = 0$ dB, low corr., no DLSCH proc. applied, no channel estim. error present
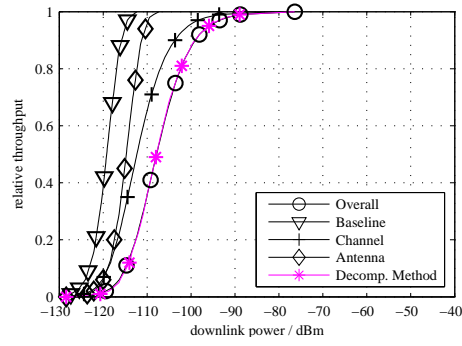
(b) Cond. number $\kappa = 10$ dB, low corr., no DLSCH proc. applied, no channel estim. error present

FIGURE A.1: "Decomposition Method" results compared to "Overall" results - rel. throughput vs. downlink power; low correlation, ICD/ZF receiving algorithm
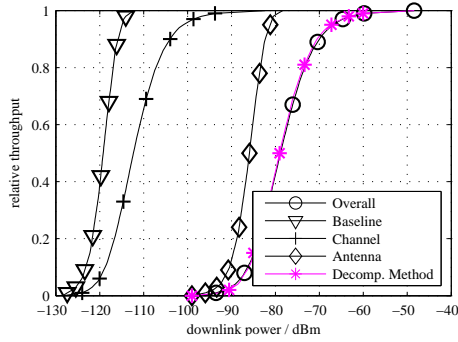
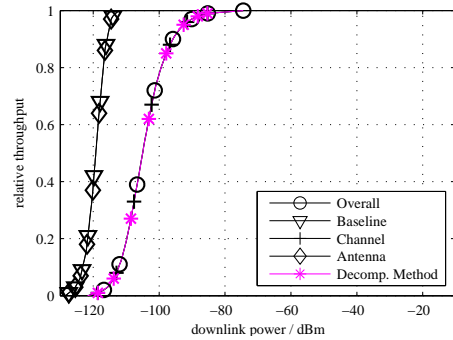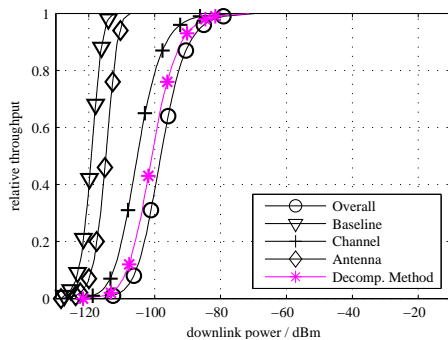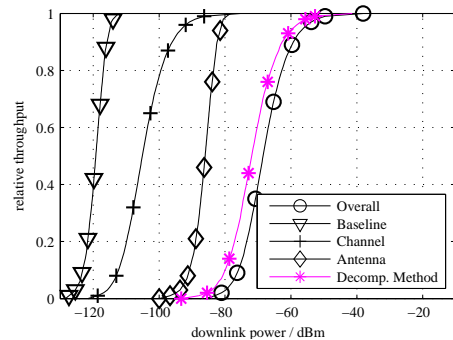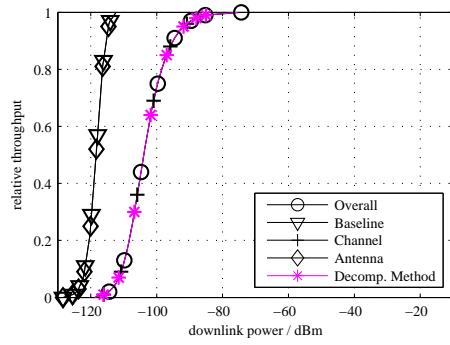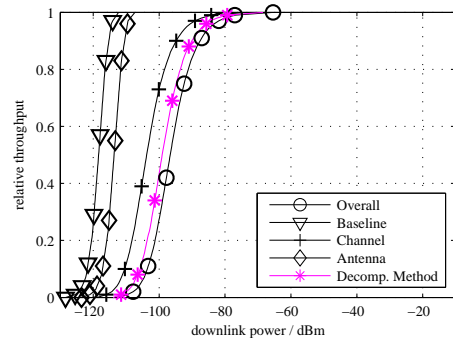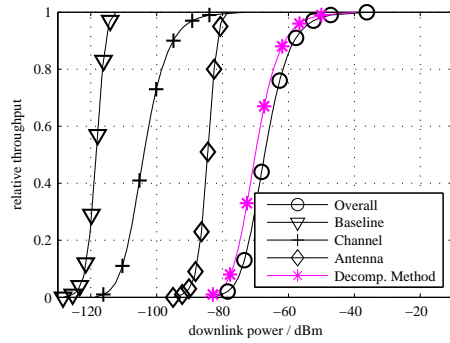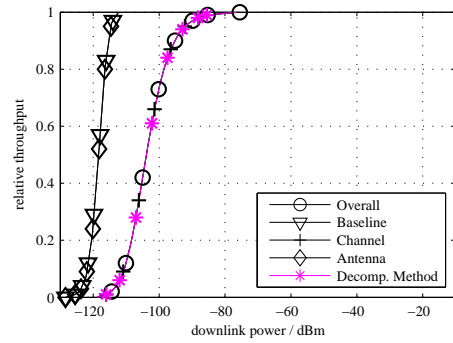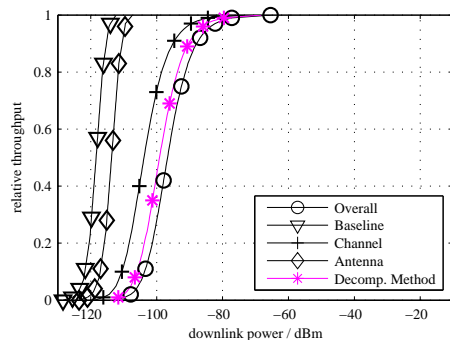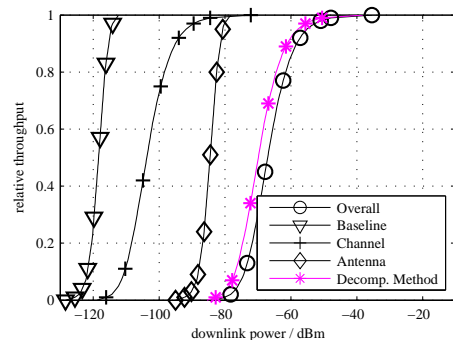(a) Cond. number $\kappa = 40$ dB, low corr., no DLSCH proc. applied, no channel estim. error present
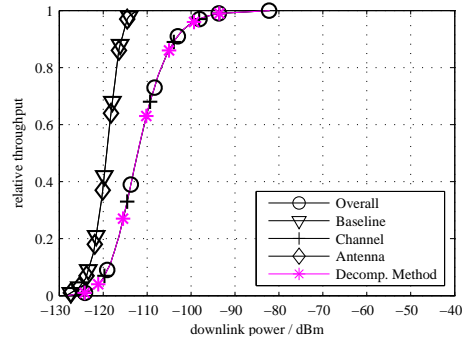
(b) Cond. number $\kappa = 0$ dB, low corr., no DLSCH proc. applied, channel estim. error present

FIGURE A.2: "Decomposition Method" results compared to "Overall" results - rel. throughput vs. downlink power; low correlation, ICD/ZF receiving algorithm
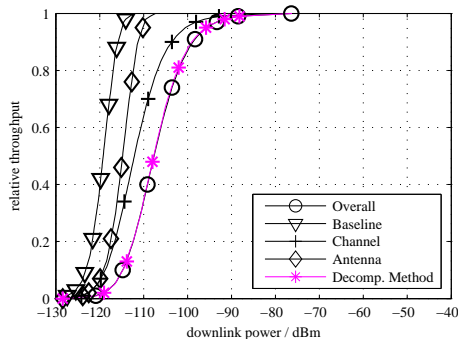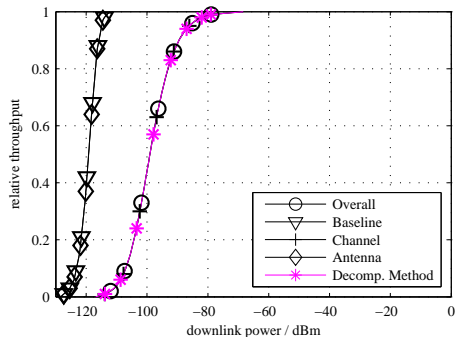

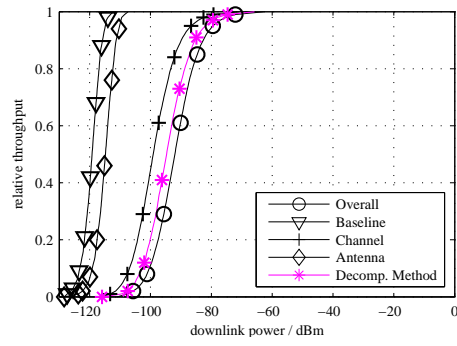(a) Cond. number $\kappa = 10$ dB, low corr., no DLSCH proc. applied, channel estim. error present
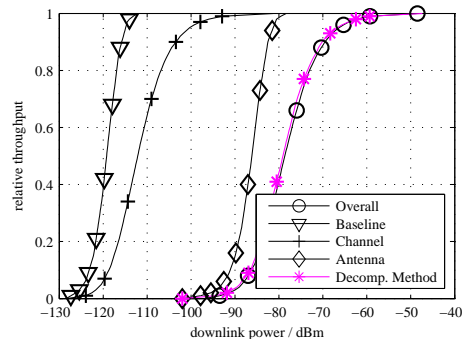
(b) Cond. number $\kappa = 40$ dB, low corr., no DLSCH proc. applied, channel estim. error present

FIGURE A.3: "Decomposition Method" results compared to "Overall" results - rel. throughput vs. downlink power; low correlation, ICD/ZF receiving algorithm
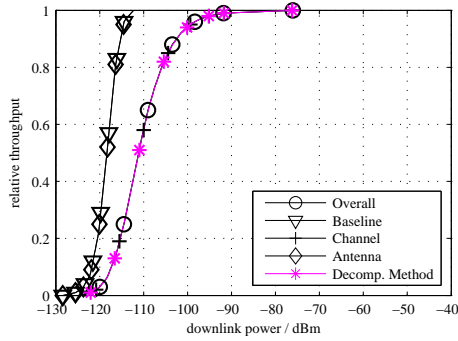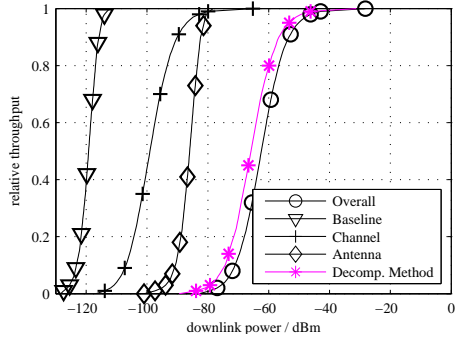
(a) Cond. number $\kappa = 0$ dB, low corr., DLSCH proc. applied, no channel estim. error present
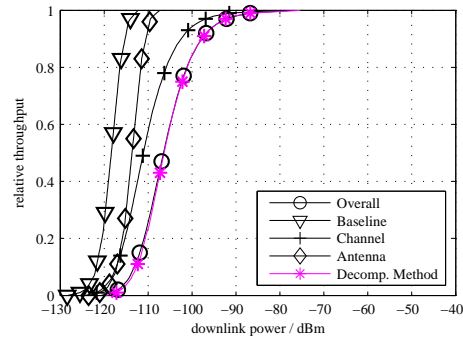
(b) Cond. number $\kappa = 10$ dB, low corr., DLSCH proc. applied, no channel estim. error present

FIGURE A.4: "Decomposition Method" results compared to "Overall" results - rel. throughput vs. downlink power; low correlation, ICD/ZF receiving algorithm
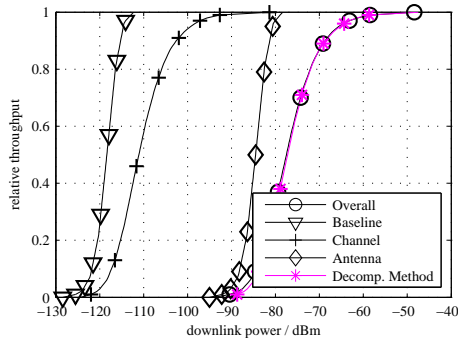
(a) Cond. number $\kappa = 40$ dB, low corr., DLSCH proc. applied, no channel estim. error present
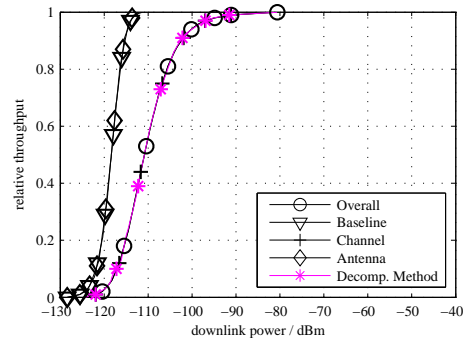
(b) Cond. number $\kappa = 0$ dB, low corr., DLSCH proc. applied, channel estim. error present

FIGURE A.5: "Decomposition Method" results compared to "Overall" results - rel. throughput vs. downlink power; low correlation, ICD/ZF receiving algorithm
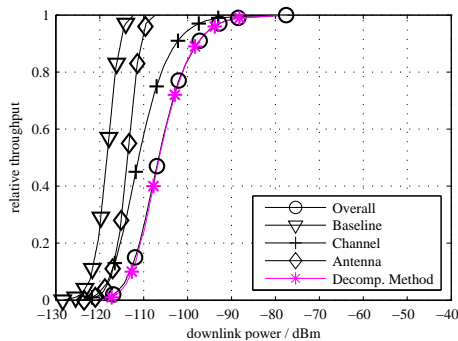
(a) Cond. number $\kappa = 10$ dB, low corr., DLSCH proc. applied, channel estim. error present
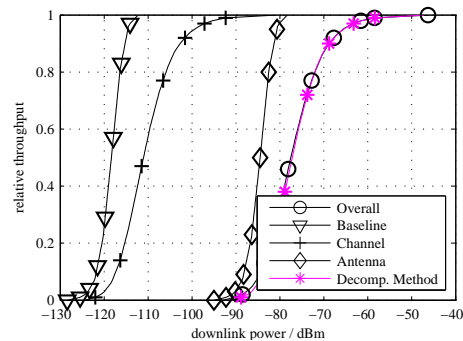
(b) Cond. number $\kappa = 40$ dB, low corr., DLSCH proc. applied, channel estim. error present

FIGURE A.6: "Decomposition Method" results compared to "Overall" results - rel. throughput vs. downlink power; low correlation, ICD/ZF receiving algorithm
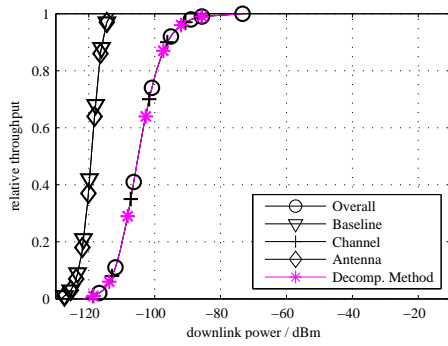
(a) Cond. number $\kappa = 0$ dB, low corr., no DLSCH proc. applied, no channel estim. error present
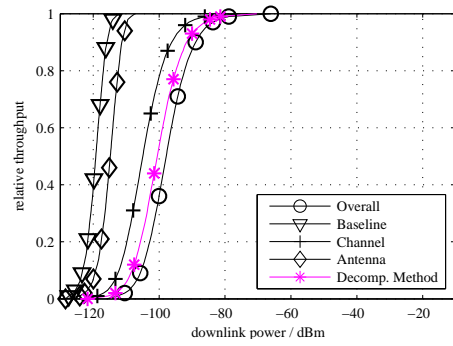
(b) Cond. number $\kappa = 10$ dB, low corr., no DLSCH proc. applied, no channel estim. error present

FIGURE A.7: "Decomposition Method" results compared to "Overall" results - rel. throughput vs. downlink power; medium correlation, ICD/ZF receiver
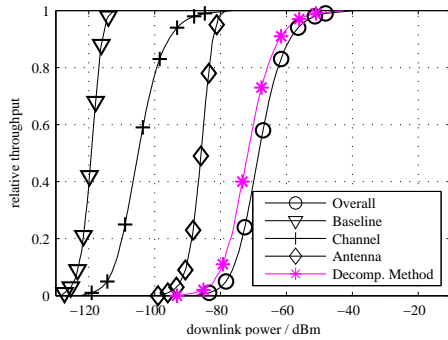
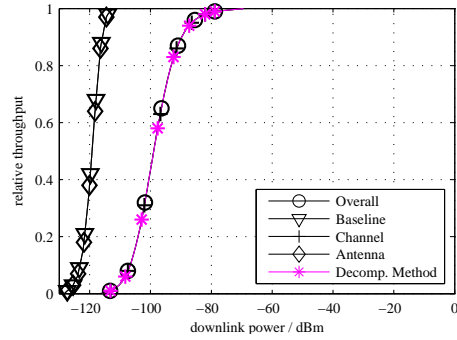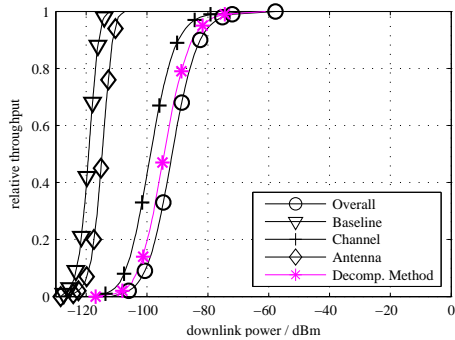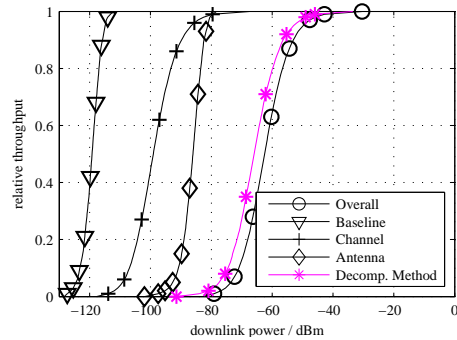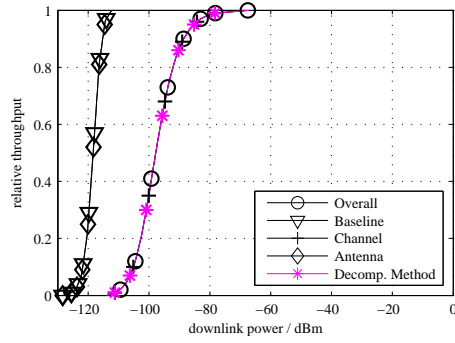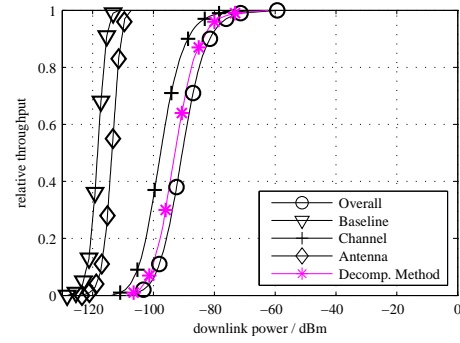(a) Cond. number $\kappa = 40$ dB, low corr., no DLSCH proc. applied, no channel estim. error present

(b) Cond. number $\kappa = 0$ dB, low corr., no DLSCH proc. applied, channel estim. error present

FIGURE A.8: "Decomposition Method" results compared to "Overall" results - rel. throughput vs. downlink power; medium correlation, ICD/ZF receiver

(a) Cond. number $\kappa = 10$ dB, low corr., no DLSCH proc. applied, channel estim. error present

(b) Cond. number $\kappa = 40$ dB, low corr., no DLSCH proc. applied, channel estim. error present

FIGURE A.9: "Decomposition Method" results compared to "Overall" results - rel. throughput vs. downlink power; medium correlation, ICD/ZF receiver
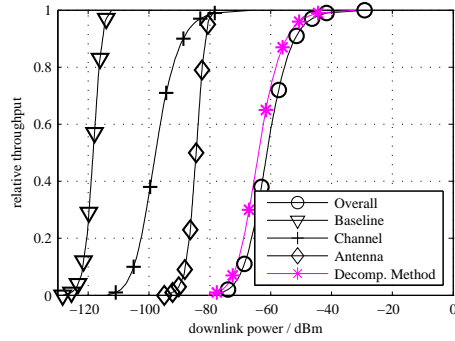
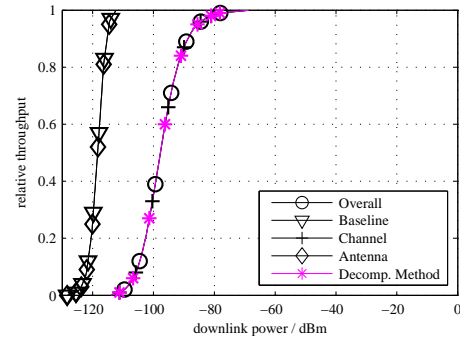(a) Cond. number $\kappa = 0$ dB, low corr., DLSCH proc. applied, no channel estim. error present

(b) Cond. number $\kappa = 10$ dB, low corr., DLSCH proc. applied, no channel estim. error present

FIGURE A.10: "Decomposition Method" results compared to "Overall" results - rel. throughput vs. downlink power; medium correlation, ICD/ZF receiver

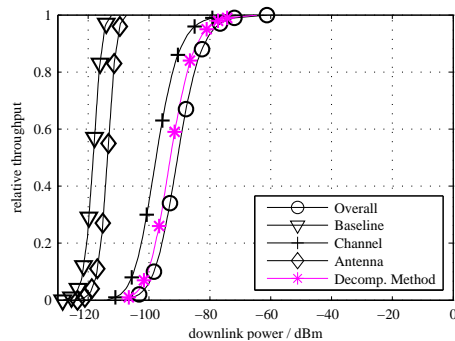(a) Cond. number $\kappa = 40$ dB, low corr., DLSCH proc. applied, no channel estim. error present
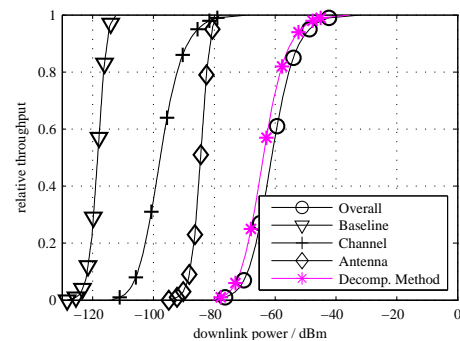
(b) Cond. number $\kappa = 0$ dB, low corr., DLSCH proc. applied, channel estim. error present

FIGURE A.11: "Decomposition Method" results compared to "Overall" results - rel. throughput vs. downlink power; medium correlation, ICD/ZF receiver
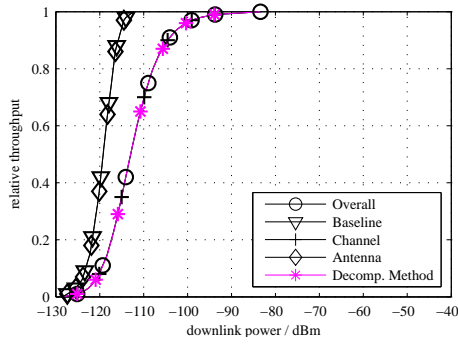

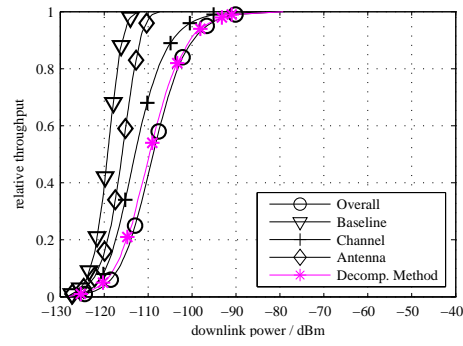(a) Cond. number $\kappa = 10$ dB, low corr., DLSCH proc. applied, channel estim. error present

(b) Cond. number $\kappa = 40$ dB, low corr., DLSCH proc. applied, channel estim. error present

FIGURE A.12: "Decomposition Method" results compared to "Overall" results - rel. throughput vs. downlink power; medium correlation, ICD/ZF receiver

(a) Cond. number $\kappa = 0$ dB, low corr., no DLSCH proc. applied, no channel estim. error present

(b) Cond. number $\kappa = 10$ dB, low corr., no DLSCH proc. applied, no channel estim. error present

FIGURE A.13: "Decomposition Method" results compared to "Overall" results - rel. throughput vs. downlink power; high correlation, ICD/ZF receiver
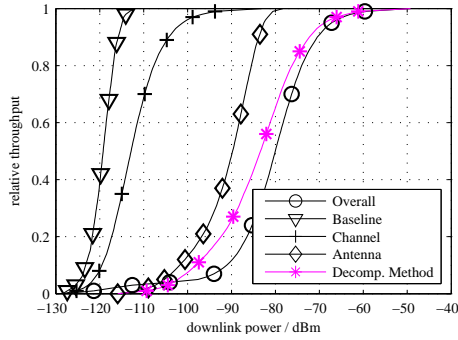

(a) Cond. number $\kappa = 40$ dB, low corr., no DLSCH proc. applied, no channel estim. error present

(b) Cond. number $\kappa = 0$ dB, low corr., no DLSCH proc. applied, channel estim. error present

FIGURE A.14: "Decomposition Method" results compared to "Overall" results - rel. throughput vs. downlink power; high correlation, ICD/ZF receiver

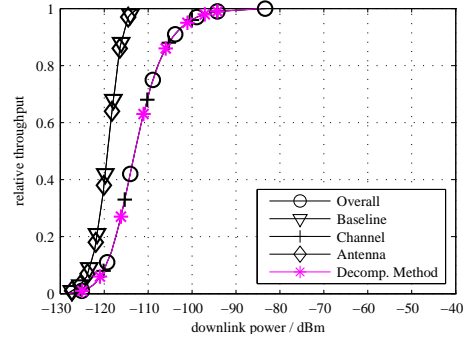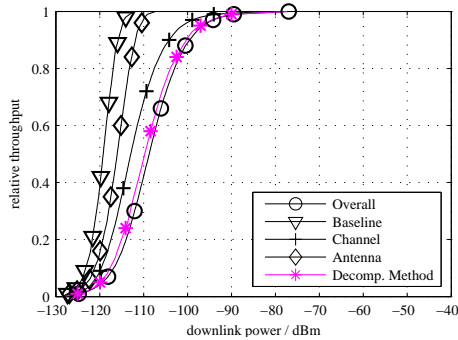(a) Cond. number $\kappa = 10$ dB, low corr., no DLSCH proc. applied, channel estim. error present

(b) Cond. number $\kappa = 40$ dB, low corr., no DLSCH proc. applied, channel estim. error present

FIGURE A.15: "Decomposition Method" results compared to "Overall" results - rel. throughput vs. downlink power; high correlation, ICD/ZF receiver

(a) Cond. number $\kappa = 0$ dB, low corr., DLSCH proc. applied, no channel estim. error present

(b) Cond. number $\kappa = 10$ dB, low corr., DLSCH proc. applied, no channel estim. error present

FIGURE A.16: "Decomposition Method" results compared to "Overall" results - rel. throughput vs. downlink power; high correlation, ICD/ZF receiver

(a) Cond. number $\kappa = 40$ dB, low corr., DLSCH proc. applied, no channel estim. error present

(b) Cond. number $\kappa = 0$ dB, low corr., DLSCH proc. applied, channel estim. error present

FIGURE A.17: "Decomposition Method" results compared to "Overall" results - rel. throughput vs. downlink power; high correlation, ICD/ZF receiver

(a) Cond. number $\kappa = 10$ dB, low corr., DLSCH proc. applied, channel estim. error present

(b) Cond. number $\kappa = 40$ dB, low corr., DLSCH proc. applied, channel estim. error present

FIGURE A.18: "Decomposition Method" results compared to "Overall" results - rel. throughput vs. downlink power; high correlation, ICD/ZF receiver

(a) Cond. number $\kappa = 0$ dB, low corr., no DLSCH proc. applied, no channel estim. error present

(b) Cond. number $\kappa = 10$ dB, low corr., no DLSCH proc. applied, no channel estim. error present

FIGURE A.19: "Decomposition Method" results compared to "Overall" results - rel. throughput vs. downlink power; low correlation, MMSE receiving algorithm

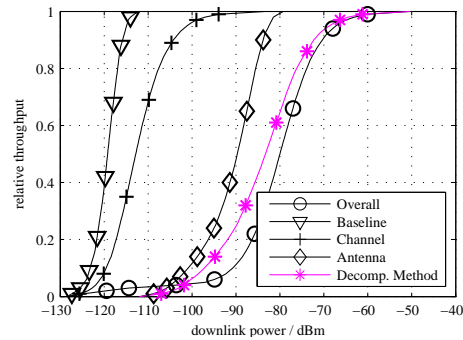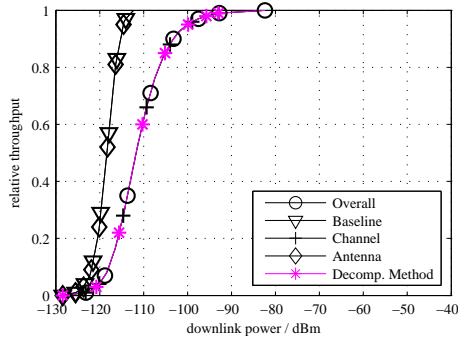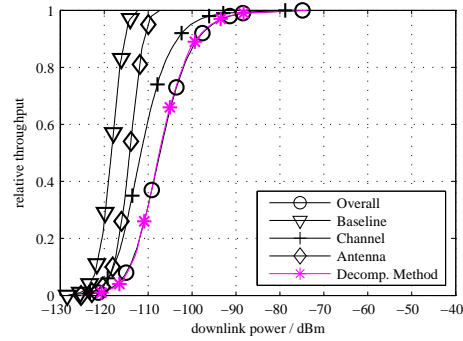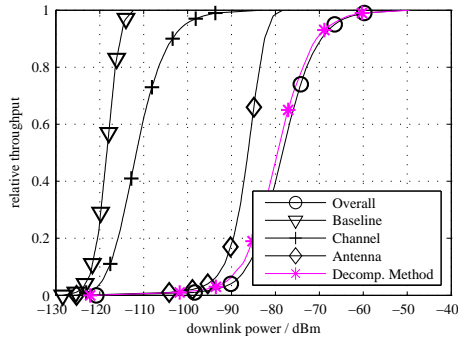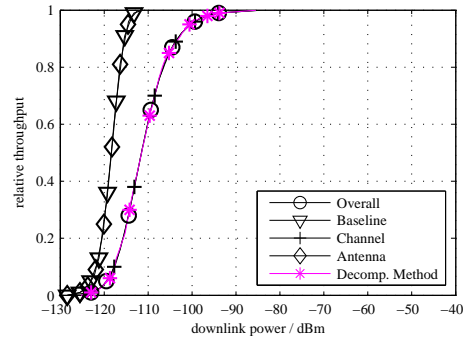(a) Cond. number $\kappa = 40$ dB, low corr., no DLSCH proc. applied, no channel estim. error present

(b) Cond. number $\kappa = 0$ dB, low corr., no DLSCH proc. applied, channel estim. error present

FIGURE A.20: "Decomposition Method" results compared to "Overall" results - rel. throughput vs. downlink power; low correlation, MMSE receiving algorithm
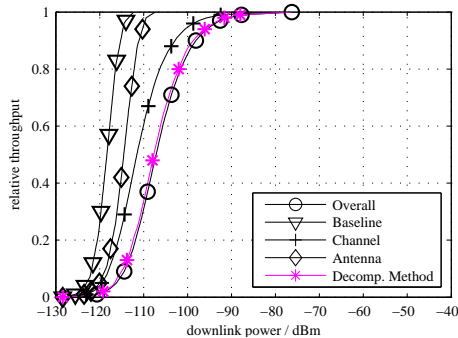

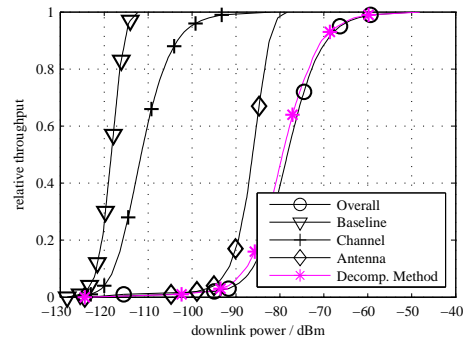(a) Cond. number $\kappa = 10$ dB, low corr., no DLSCH proc. applied, channel estim. error present

(b) Cond. number $\kappa = 40$ dB, low corr., no DLSCH proc. applied, channel estim. error present

FIGURE A.21: "Decomposition Method" results compared to "Overall" results - rel. throughput vs. downlink power; low correlation, MMSE receiving algorithm
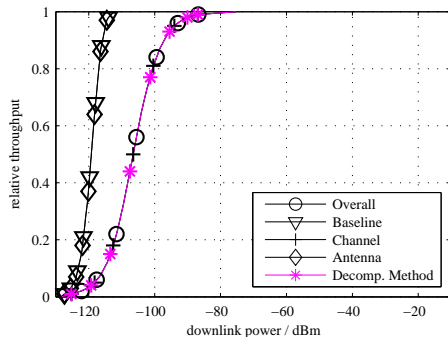
(a) Cond. number $\kappa = 0$ dB, low corr., DLSCH proc. applied, no channel estim. error present

(b) Cond. number $\kappa = 10$ dB, low corr., DLSCH proc. applied, no channel estim. error present

FIGURE A.22: "Decomposition Method" results compared to "Overall" results - rel. throughput vs. downlink power; low correlation, MMSE receiving algorithm

(a) Cond. number $\kappa = 40$ dB, low corr., DLSCH proc. applied, no channel estim. error present
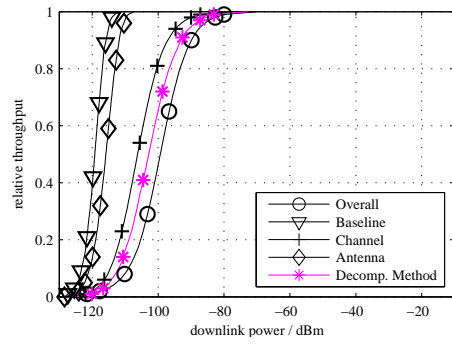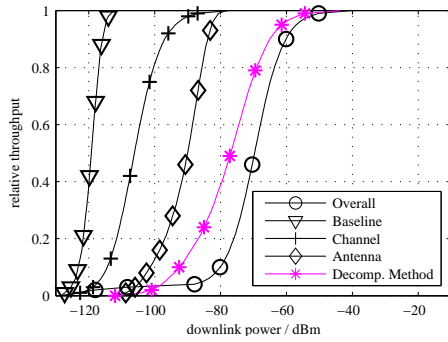
(b) Cond. number $\kappa = 0$ dB, low corr., DLSCH proc. applied, channel estim. error present

FIGURE A.23: "Decomposition Method" results compared to "Overall" results - rel. throughput vs. downlink power; low correlation, MMSE receiving algorithm

(a) Cond. number $\kappa = 10$ dB, low corr., DLSCH proc. applied, channel estim. error present

(b) Cond. number $\kappa = 40$ dB, low corr., DLSCH proc. applied, channel estim. error present

FIGURE A.24: "Decomposition Method" results compared to "Overall" results - rel. throughput vs. downlink power; low correlation, MMSE receiving algorithm

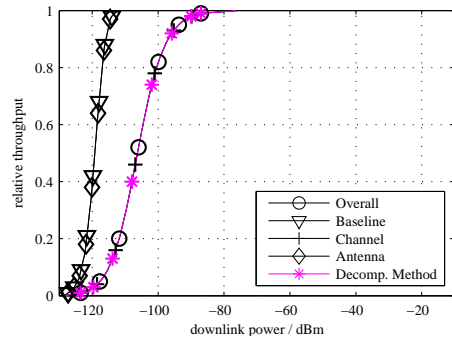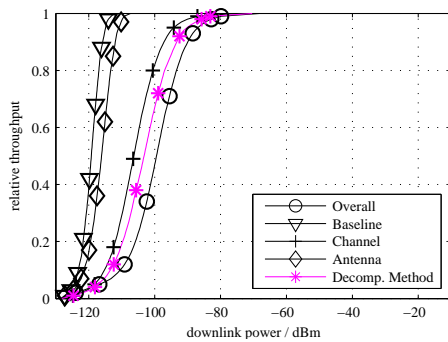(a) Cond. number $\kappa = 0$ dB, low corr., no DLSCH proc. applied, no channel estim. error present

(b) Cond. number $\kappa = 10$ dB, low corr., no DLSCH proc. applied, no channel estim. error present

FIGURE A.25: "Decomposition Method" results compared to "Overall" results - rel. throughput vs. downlink power; medium correlation, MMSE receiver

(a) Cond. number $\kappa = 40$ dB, low corr., no DLSCH proc. applied, no channel estim. error present
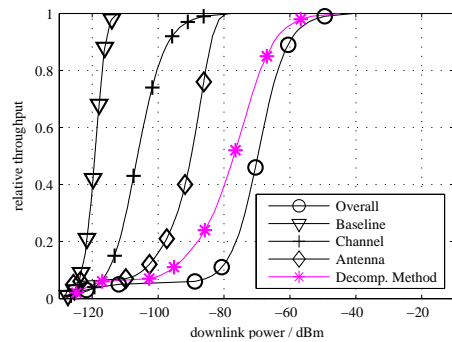
(b) Cond. number $\kappa = 0$ dB, low corr., no DLSCH proc. applied, channel estim. error present

FIGURE A.26: "Decomposition Method" results compared to "Overall" results - rel. throughput vs. downlink power; medium correlation, MMSE receiver
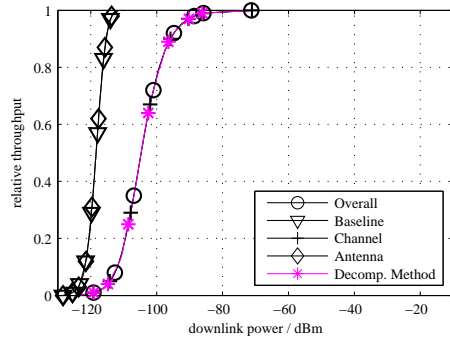

(a) Cond. number $\kappa = 10$ dB, low corr., no DLSCH proc. applied, channel estim. error present
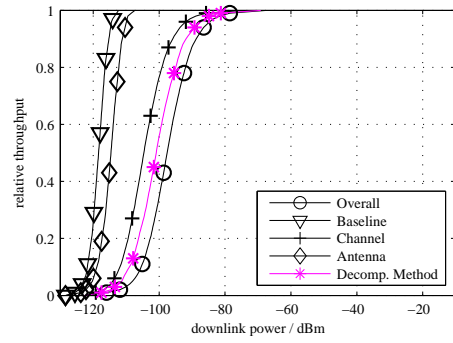
(b) Cond. number $\kappa = 40$ dB, low corr., no DLSCH proc. applied, channel estim. error present

FIGURE A.27: "Decomposition Method" results compared to "Overall" results - rel. throughput vs. downlink power; medium correlation, MMSE receiver

(a) Cond. number $\kappa = 0$ dB, low corr., DLSCH proc. applied, no channel estim. error present

(b) Cond. number $\kappa = 10$ dB, low corr., DLSCH proc. applied, no channel estim. error present

FIGURE A.28: "Decomposition Method" results compared to "Overall" results - rel. throughput vs. downlink power; medium correlation, MMSE receiver
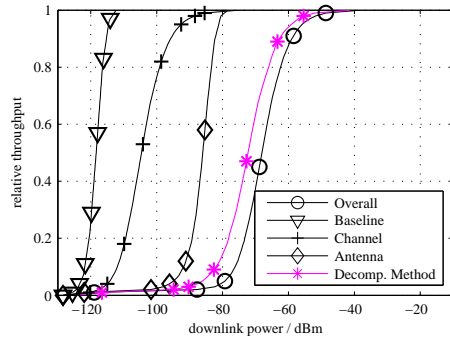

(a) Cond. number $\kappa = 40$ dB, low corr., DLSCH proc. applied, no channel estim. error present
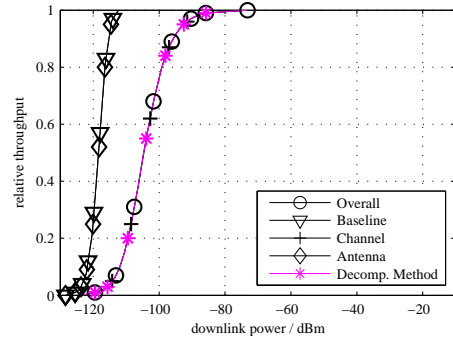
(b) Cond. number $\kappa = 0$ dB, low corr., DLSCH proc. applied, channel estim. error present

FIGURE A.29: "Decomposition Method" results compared to "Overall" results - rel. throughput vs. downlink power; medium correlation, MMSE receiver
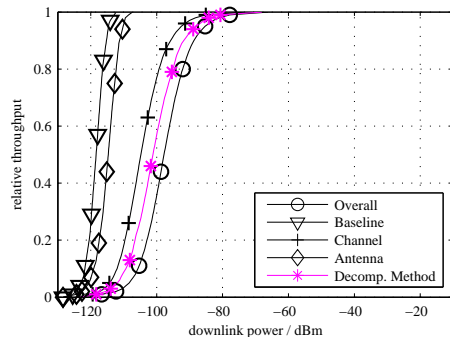

(a) Cond. number $\kappa = 10$ dB, low corr., DLSCH proc. applied, channel estim. error present

(b) Cond. number $\kappa = 40$ dB, low corr., DLSCH proc. applied, channel estim. error present

FIGURE A.30: "Decomposition Method" results compared to "Overall" results - rel. throughput vs. downlink power; medium correlation, MMSE receiver

(a) Cond. number $\kappa = 0$ dB, low corr., no DLSCH proc. applied, no channel estim. error present
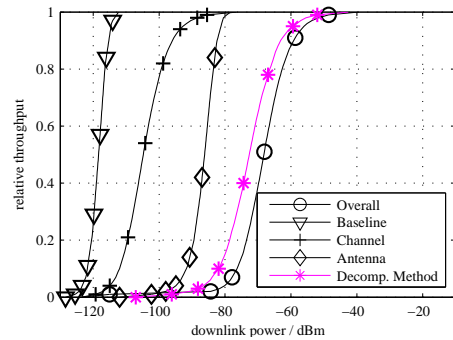
(b) Cond. number $\kappa = 10$ dB, low corr., no DLSCH proc. applied, no channel estim. error present

FIGURE A.31: "Decomposition Method" results compared to "Overall" results - rel. throughput vs. downlink power; high correlation, MMSE receiver

(a) Cond. number $\kappa = 40$ dB, low corr., no DLSCH proc. applied, no channel estim. error present

(b) Cond. number $\kappa = 0$ dB, low corr., no DLSCH proc. applied, channel estim. error present

FIGURE A.32: "Decomposition Method" results compared to "Overall" results - rel. throughput vs. downlink power; high correlation, MMSE receiver
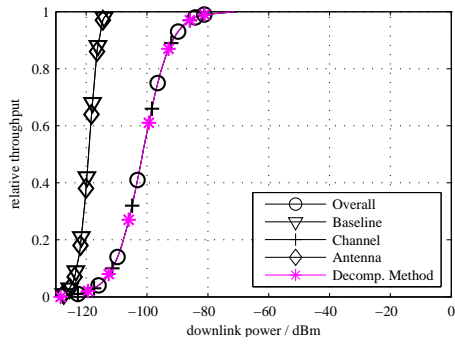

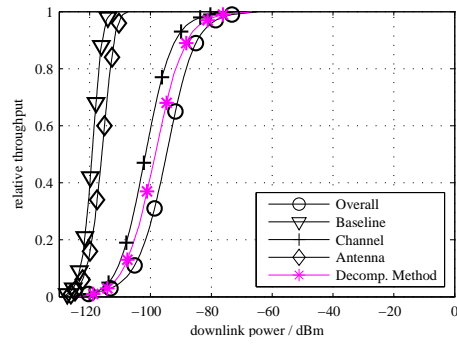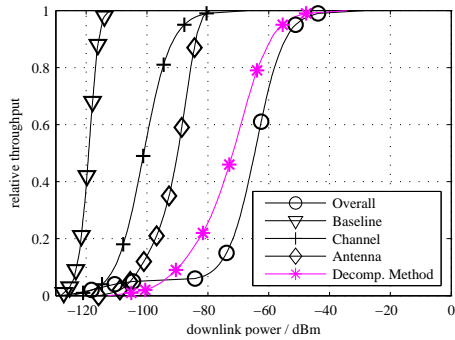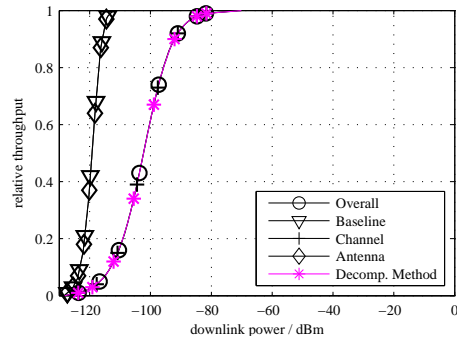(a) Cond. number $\kappa = 10$ dB, low corr., no DLSCH proc. applied, channel estim. error present

(b) Cond. number $\kappa = 40$ dB, low corr., no DLSCH proc. applied, channel estim. error present

FIGURE A.33: "Decomposition Method" results compared to "Overall" results - rel. throughput vs. downlink power; high correlation, MMSE receiver

(a) Cond. number $\kappa = 0$ dB, low corr., DLSCH proc. applied, no channel estim. error present

(b) Cond. number $\kappa = 10$ dB, low corr., DLSCH proc. applied, no channel estim. error present

FIGURE A.34: "Decomposition Method" results compared to "Overall" results - rel. throughput vs. downlink power; high correlation, MMSE receiver
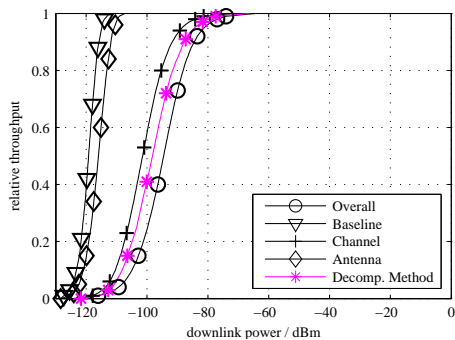

(a) Cond. number $\kappa = 40$ dB, low corr., DLSCH proc. applied, no channel estim. error present

(b) Cond. number $\kappa = 0$ dB, low corr., DLSCH proc. applied, channel estim. error present

FIGURE A.35: "Decomposition Method" results compared to "Overall" results - rel. throughput vs. downlink power; high correlation, MMSE receiver

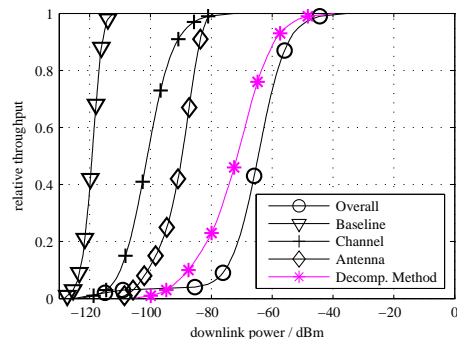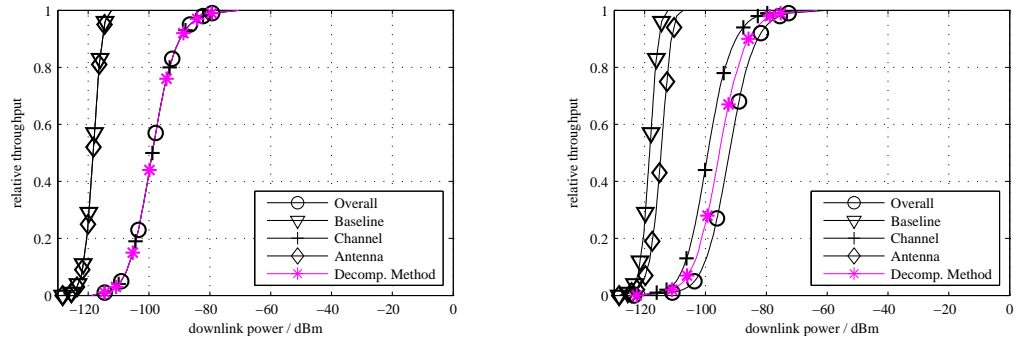(a) Cond. number $\kappa = 10$ dB, low corr., DLSCH proc. applied, channel estim. error present
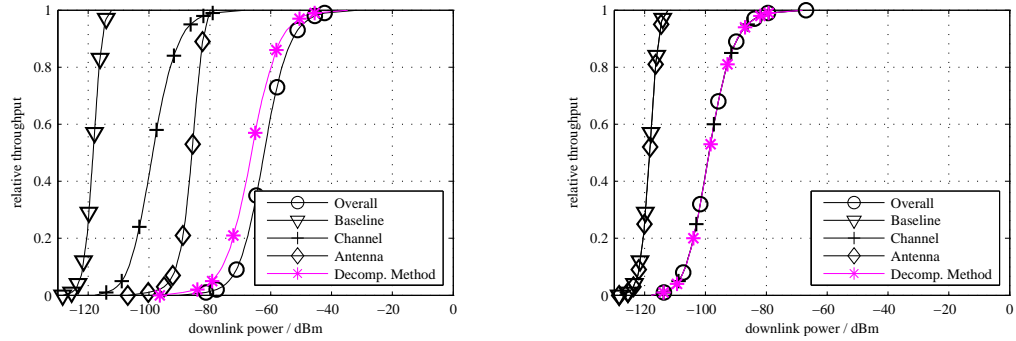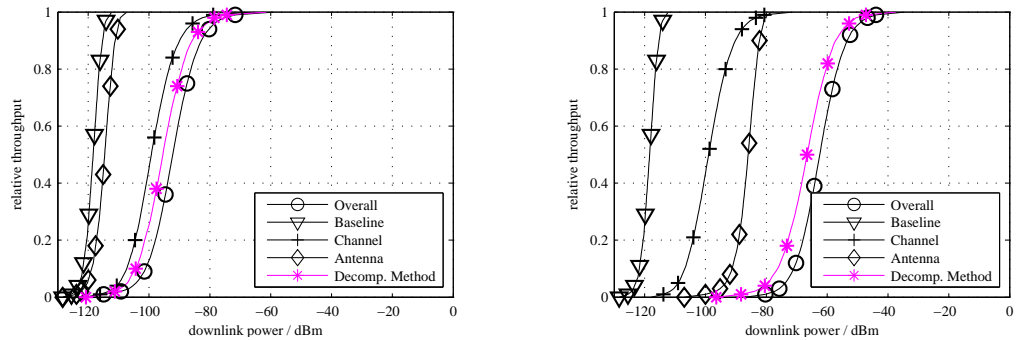
(b) Cond. number $\kappa = 40$ dB, low corr., DLSCH proc. applied, channel estim. error present

FIGURE A.36: "Decomposition Method" results compared to "Overall" results - rel. throughput vs. downlink power; high correlation, MMSE receiver

Appendix B

Deviation Histograms Using Reference Antennas

B.1 Simulations employing the Kronecker Channel Model

This part of the Appendix contains all histograms of the deviation d and the mean logarithmic deviation $\bar{d}$ for all constellations and the variation of the parameter set, as described in Chap. 7.4.3:

- Receiver type: ICD/ZF or MMSE

- DLSCH processing on/off

- ideal/non-ideal channel estimation

- low, medium or highly correlated channel

- reference antenna type: "Good", "Nominal" and "Bad"

Table B.1 shows these parameter variations and its associated figures.

The correlation factors of the Kronecker channel model follow the values proposed in [73], [75].

TABLE B.1: Overview of relative throughput vs. downlink power simulations employing different receiver types, correlation grade, DLSCH processing and channel estimation error presence including figure numbers

receiver type	corr.	DLSCH proc.	ch. est. err. present	Fig. number
ICD/ZF	low	off	no	B.1
ICD/ZF	low	off	yes	B.2
ICD/ZF	low	on	no	B.3
ICD/ZF	low	on	yes	B.4
ICD/ZF	med	off	no	B.5
ICD/ZF	med	off	yes	B.6
ICD/ZF	med	on	no	B.7
ICD/ZF	med	on	yes	B.8
ICD/ZF	high	off	no	B.9
ICD/ZF	high	off	yes	B.10
ICD/ZF	high	on	no	B.11
ICD/ZF	high	on	yes	B.12
MMSE	low	off	no	B.13
MMSE	low	off	yes	B.14
MMSE	low	on	no	B.15
MMSE	low	on	yes	B.16
MMSE	med	off	no	B.17
MMSE	med	off	yes	B.18
MMSE	med	on	no	B.19
MMSE	med	on	yes	B.20
MMSE	high	off	no	B.21
MMSE	high	off	yes	B.22
MMSE	high	on	no	B.23
MMSE	high	on	yes	B.24

FIGURE B.1: Histogram of the deviation d using correlation low, DLSCH processing off, no channel estimation error; ICD/ZF receiver

FIGURE B.2: Histogram of the deviation d using correlation low, DLSCH processing off, channel estimation error present; ICD/ZF receiver

FIGURE B.3: Histogram of the deviation d using correlation low, DLSCH processing on, no channel estimation error; ICD/ZF receiver

FIGURE B.4: Histogram of the deviation d using correlation low, DLSCH processing on, channel estimation error present; ICD/ZF receiver
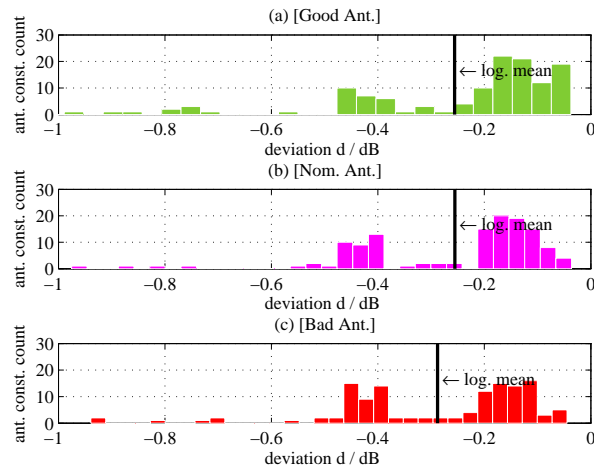

FIGURE B.5: Histogram of the deviation d using correlation medium, DLSCH processing off, no channel estimation error; ICD/ZF receiver

FIGURE B.6: Histogram of the deviation d using correlation medium, DLSCH processing off, channel estimation error present; ICD/ZF receiver

FIGURE B.7: Histogram of the deviation d using correlation medium, DLSCH processing on, no channel estimation error present; ICD/ZF receiver

FIGURE B.8: Histogram of the deviation d using correlation medium, DLSCH processing on, channel estimation error present; ICD/ZF receiver

FIGURE B.9: Histogram of the deviation d using correlation high, DLSCH processing off, no channel estimation error present; ICD/ZF receiver
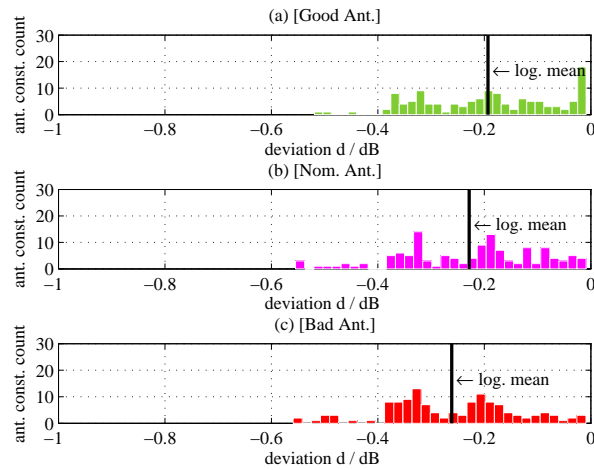
FIGURE B.10: Histogram of the deviation d using correlation high, DLSCH processing off, channel estimation error present; ICD/ZF receiver
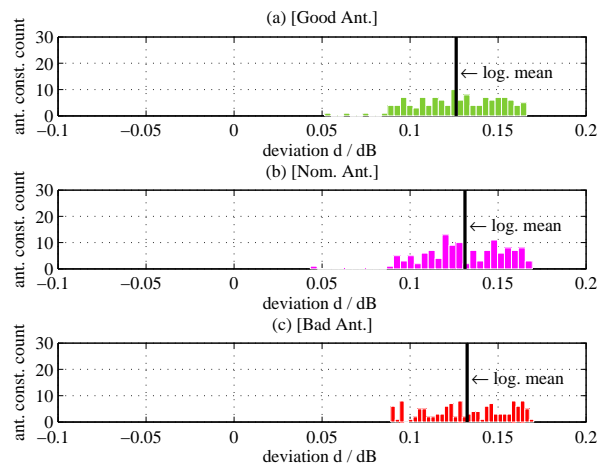

FIGURE B.11: Histogram of the deviation d using correlation high, DLSCH processing on, no channel estimation error present; ICD/ZF receiver
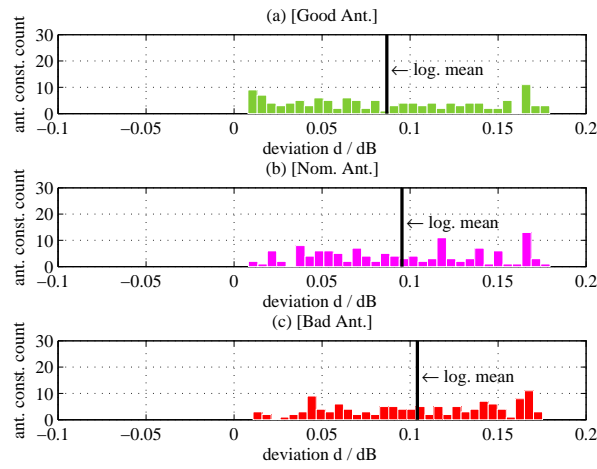

FIGURE B.12: Histogram of the deviation d using correlation high, DLSCH processing on, channel estimation error present; ICD/ZF receiver

FIGURE B.13: Histogram of the deviation d using correlation low, DLSCH processing off, no channel estimation error present; MMSE receiver

FIGURE B.14: Histogram of the deviation d using correlation low, DLSCH processing off, channel estimation error present; MMSE receiver
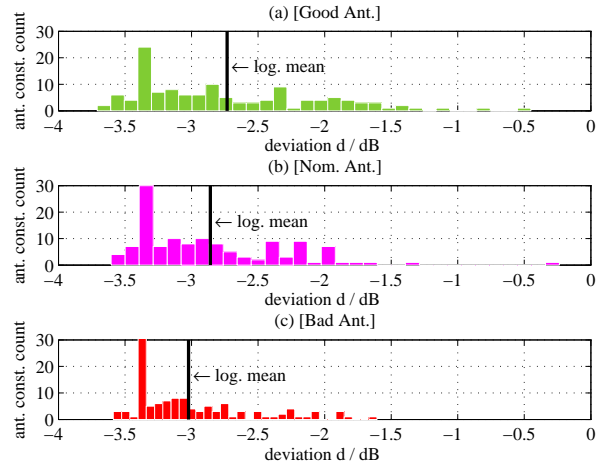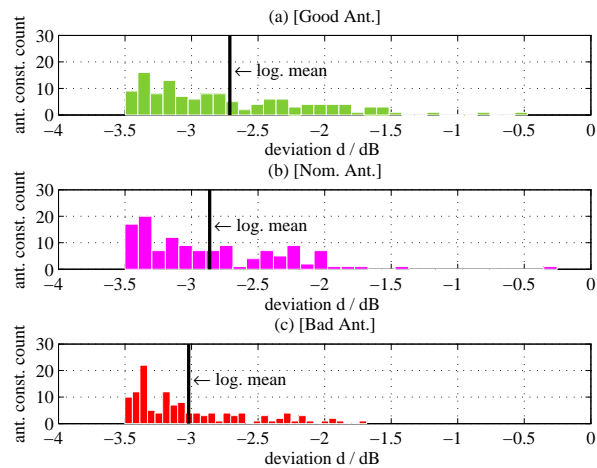

FIGURE B.15: Histogram of the deviation d using correlation low, DLSCH processing on, no channel estimation error present; MMSE receiver

FIGURE B.16: Histogram of the deviation d using correlation low, DLSCH processing on, channel estimation error present; MMSE receiver

FIGURE B.17: Histogram of the deviation d using correlation medium, DLSCH processing off, no channel estimation error present; MMSE receiver

FIGURE B.18: Histogram of the deviation d using correlation medium, DLSCH processing off, channel estimation error present; MMSE receiver
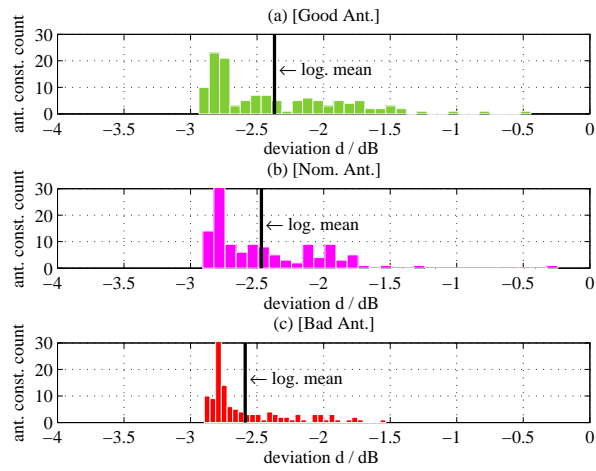
FIGURE B.19: Histogram of the deviation d using correlation medium, DLSCH processing on, no channel estimation error present; MMSE receiver
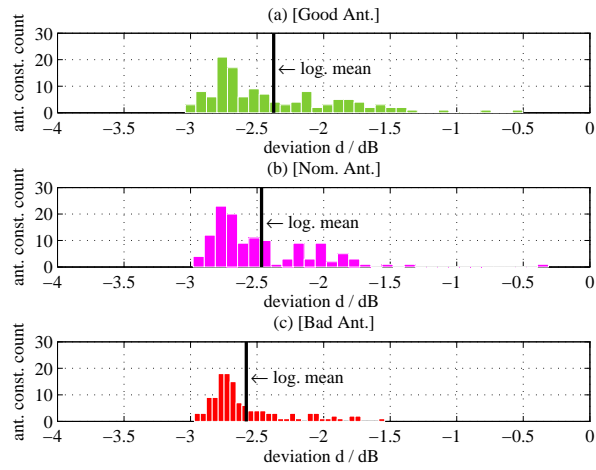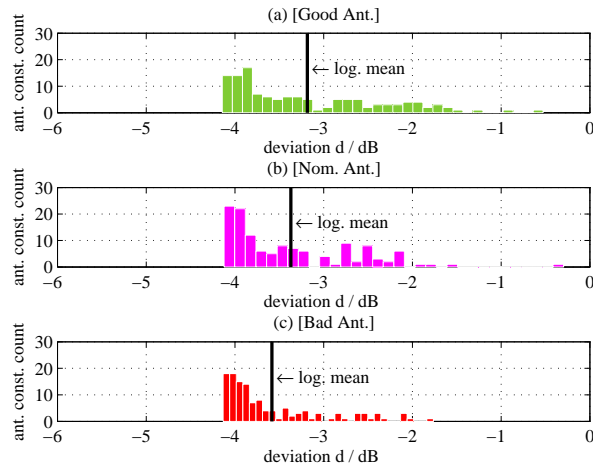

FIGURE B.20: Histogram of the deviation d using correlation medium, DLSCH processing on, channel estimation error present; MMSE receiver
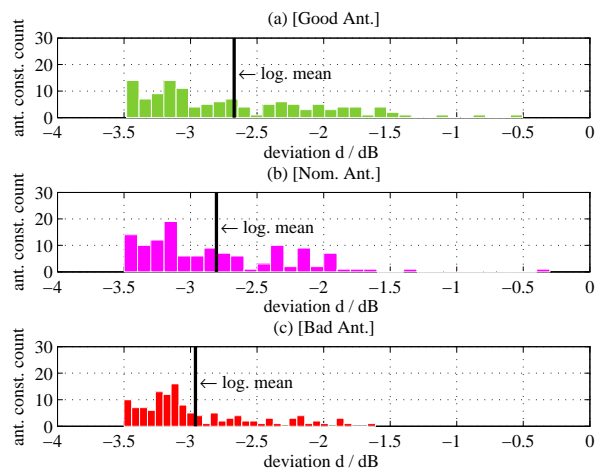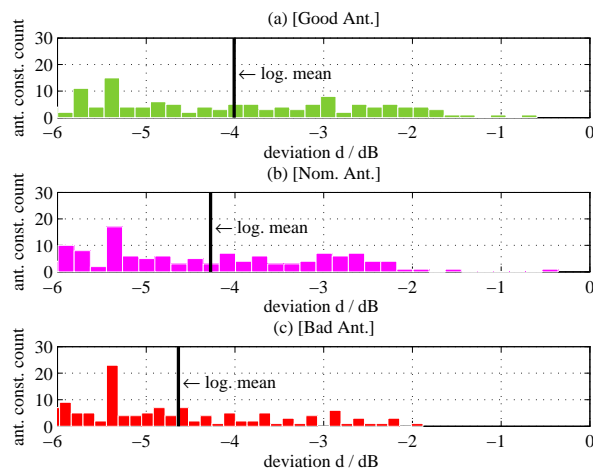

FIGURE B.21: Histogram of the deviation d using correlation high, DLSCH processing off, no channel estimation error present; MMSE receiver
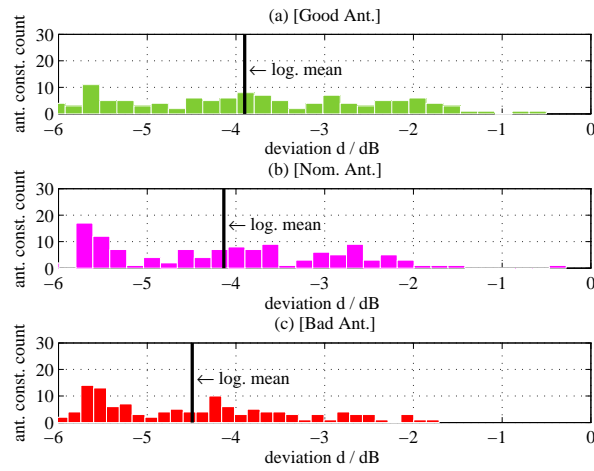
FIGURE B.22: Histogram of the deviation d using correlation high, DLSCH processing off, channel estimation error present; MMSE receiver
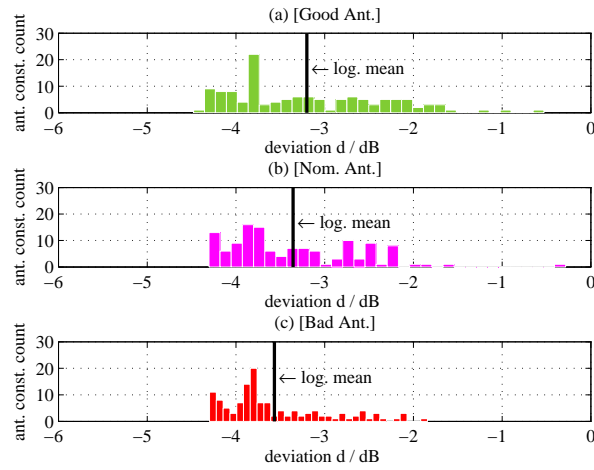
FIGURE B.23: Histogram of the deviation d using correlation high, DLSCH processing on, no channel estimation error present; MMSE receiver
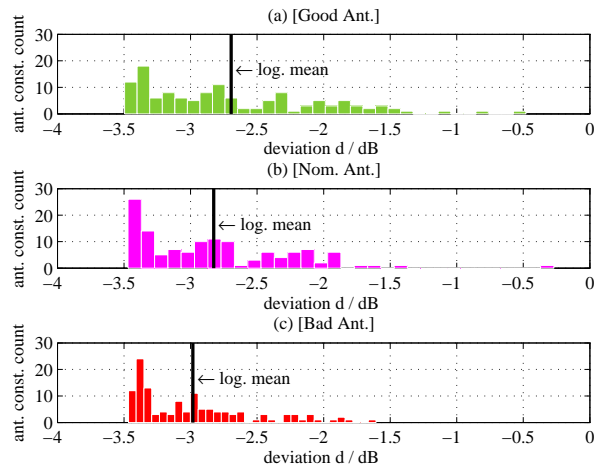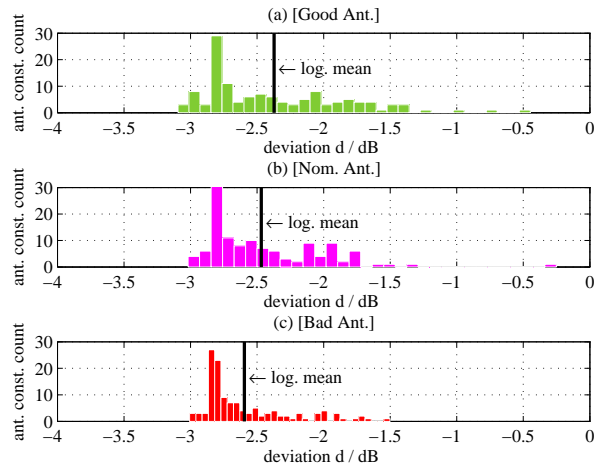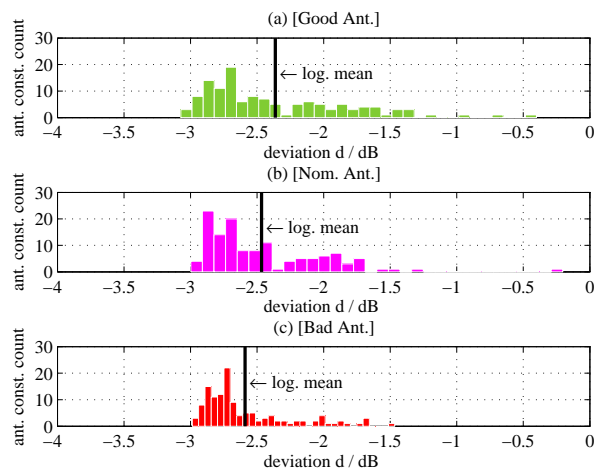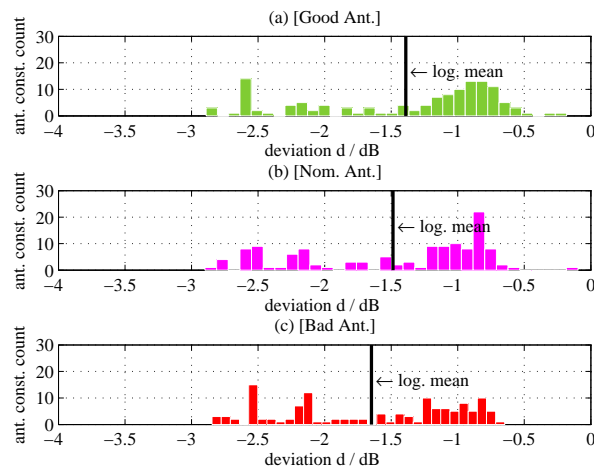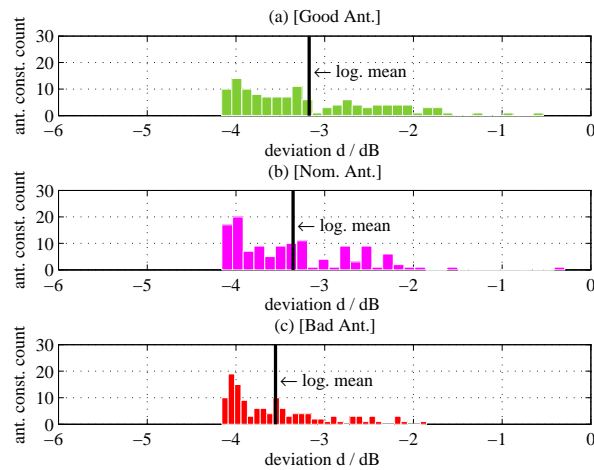

FIGURE B.24: Histogram of the deviation d using correlation high, DLSCH processing on, channel estimation error present; MMSE receiver

B.2   Simulations for Comparison to the Measurements
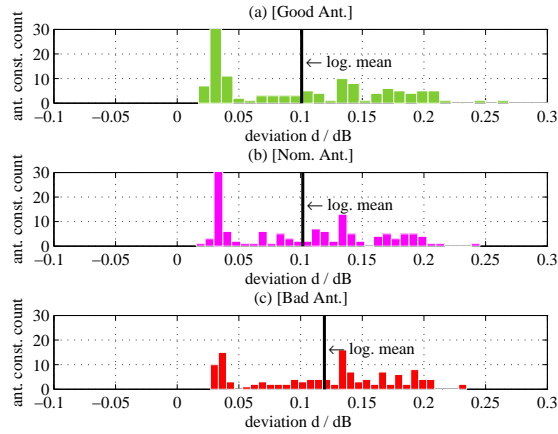
FIGURE B.25: Histogram of the deviation d using $\alpha = 0.1172$, DLSCH processing on, channel estimation error present; ICD/ZF receiver
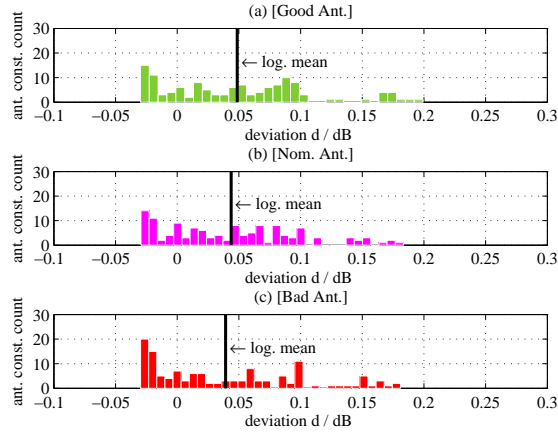
FIGURE B.26:   Histogram of the deviation d using $\alpha = 0$, DLSCH processing on, channel estimation error present; ICD/ZF receiver
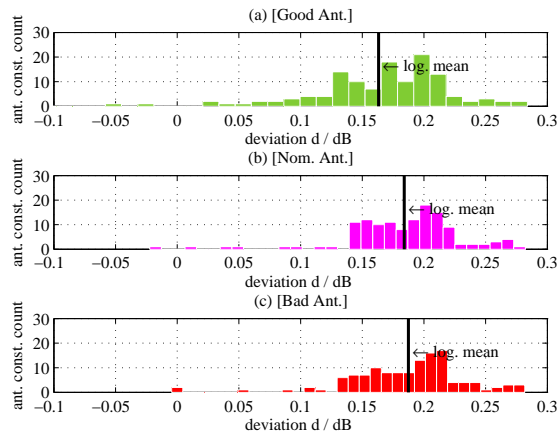
FIGURE B.27: Histogram of the deviation d using $\alpha = 0.9474$, DLSCH processing on, channel estimation error present; ICD/ZF receiver
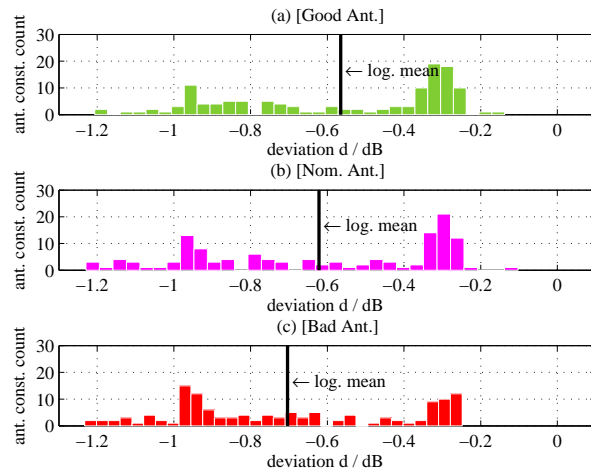
FIGURE B.28: Histogram of the deviation d using $\alpha = 0.1172$, DLSCH processing on, channel estimation error present; MMSE receiver
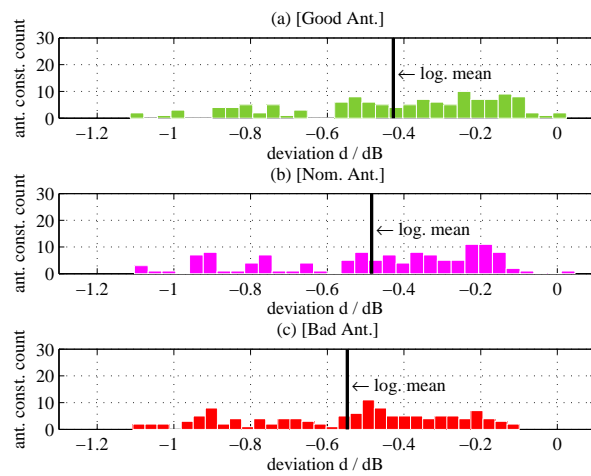
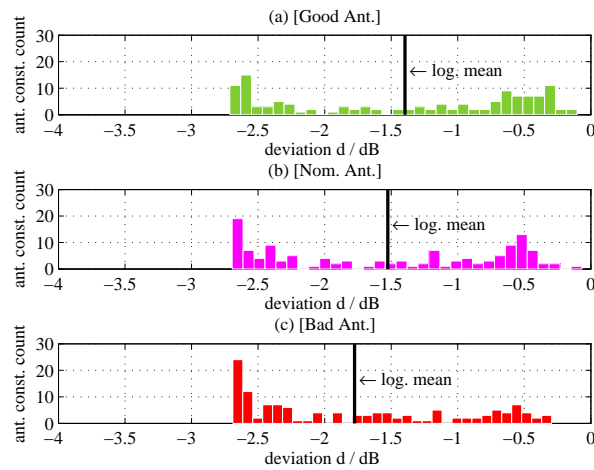FIGURE B.29: Histogram of the deviation d using $\alpha = 0$, DLSCH processing on, channel estimation error present; MMSE receiver
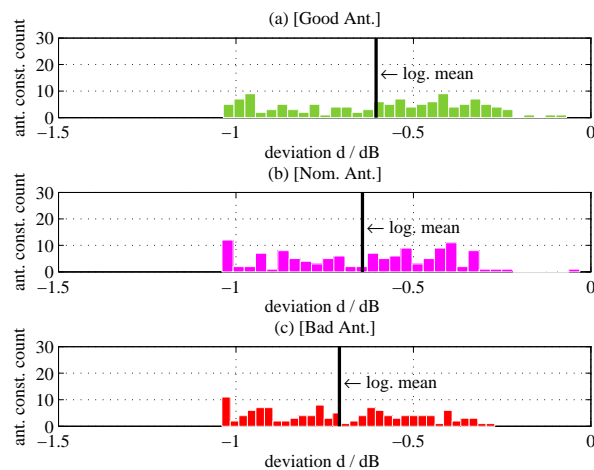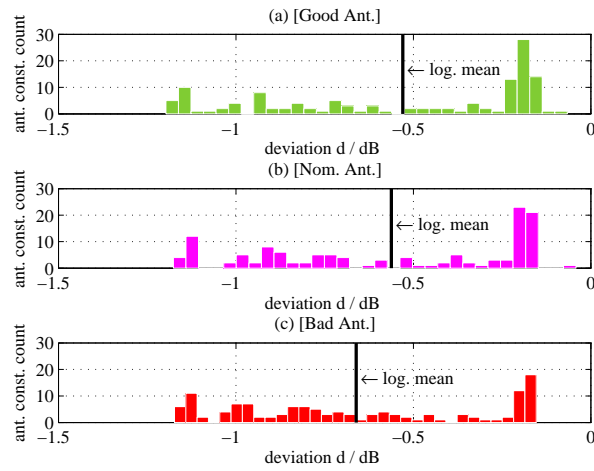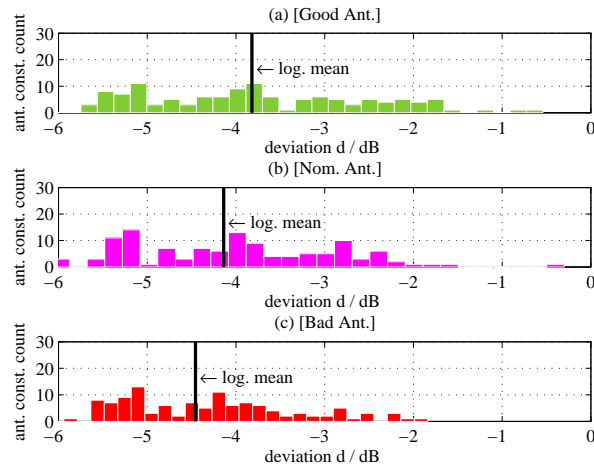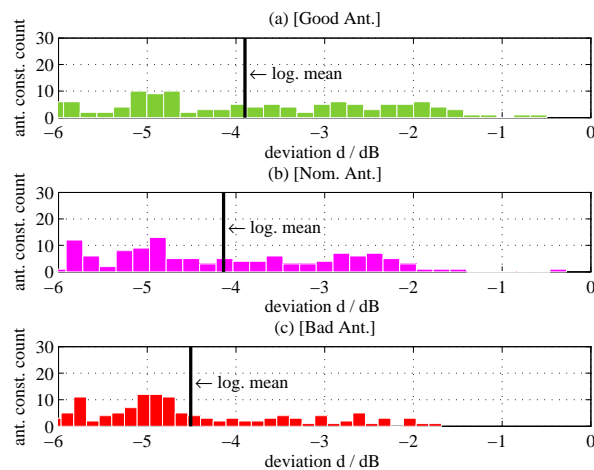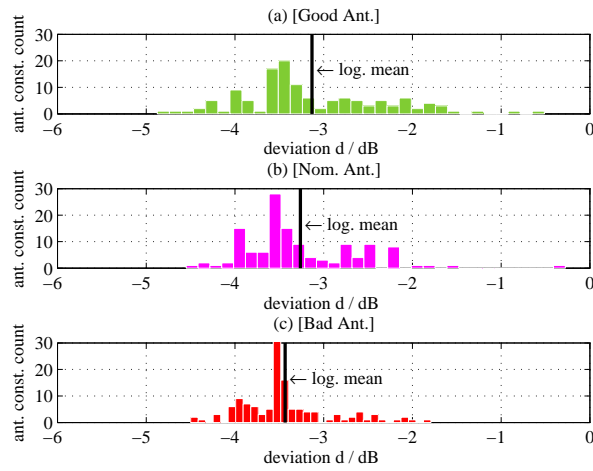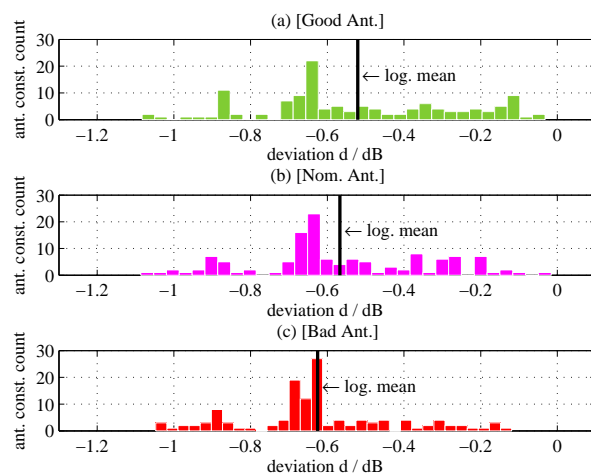

FIGURE B.30: Histogram of the deviation d using $\alpha = 0.9474$, DLSCH processing on, channel estimation error present; MMSE receiver

Appendix C

Parameters for the Measurements

This Appendix contains parameters for the measurement of the UE including the three channel models used for the measurements in Chap. 8. Measurements were done with CMW 500 base station emulator and an SMW 200 channel emulator.

The measurement setup and configuration is:

- UE: Sony Xperia smartphone

- LTE Band: FDD7 (frequency division duplex (FDD))

- Tranmsission mode: open loop spatial multiplexing (OLSM)

- Fixed reference channel: R.35

- Modulation scheme: 64QAM

- Throughput level: 70 %

The following tables C.1, C.2 and C.3 are extensively discussed in [88], a brief summary to the channel parameters is given. The relative UE velocities for each mth cluster $v_{\text{ue},m}$ are calculated according the mth *angle of arrival* (AoA_m),

$$v_{\text{UE},m} = |v_{\text{UE}} \ cos(AoA_m - DoT)| \qquad (\text{C}.1)$$

v_{UE} is the speed of the UE and DoT is the *direction of travel*. The variables α_m denote the correlation coefficient of the base station antennas, and β_m stand for the correlation

TABLE C.1: tSCME Umi (urban micro cell) MC/A channel model parameter table

delay / ns	power P_m / dB	speed $v_{\text{ue},m}$/ km/h	alpha α_m	beta β_m
0	-3.0	14.68	0.007	0
5	-5.2	14.68	0.007	0
10	-7.2	14.68	0.007	0
205	-5.7	26.94	0.429	0
210	-7.9	26.94	0.429	0
215	-9.7	26.94	0.429	0
285	-4.3	20.54	0.031	0
290	-6.5	20.54	0.031	0
295	-8.3	20.54	0.031	0
660	-7.3	26.11	0.239	0
665	-9.5	26.11	0.239	0
670	-11.3	26.11	0.239	0
805	-9.0	19.84	0.007	0
810	-11.2	19.84	0.007	0
815	-13	19.84	0.007	0
925	-11.4	15.50	0.265	0
930	-13.6	15.50	0.265	0
935	-15.4	15.50	0.265	0

coefficient of the UE antennas, both for the mth path [88]. The delay refers to the time delay of one signal of several multipath components arriving at the sink. The power of the arriving multipath signal m is the total radiated power with subtracted multipath attenuation P_m.

TABLE C.2: tSCME Umi (urban micro cell) MC/A channel model parameter table (all $\alpha_m = 0$)

delay / ns	power P_m / dB	speed $v_{\text{ue},m}$/ km/h	alpha α_m	beta β_m
0	-3.0	14.68	0	0
5	-5.2	14.68	0	0
10	-7.2	14.68	0	0
205	-5.7	26.94	0	0
210	-7.9	26.94	0	0
215	-9.7	26.94	0	0
285	-4.3	20.54	0	0
290	-6.5	20.54	0	0
295	-8.3	20.54	0	0
660	-7.3	26.11	0	0
665	-9.5	26.11	0	0
670	-11.3	26.11	0	0
805	-9.0	19.84	0	0
810	-11.2	19.84	0	0
815	-13	19.84	0	0
925	-11.4	15.50	0	0
930	-13.6	15.50	0	0
935	-15.4	15.50	0	0

TABLE C.3: tSCME Uma (urban macro cell) MC/A channel model parameter table

delay / ns	power P_m / dB	speed $v_{\text{ue},m}$/ km/h	alpha α_m	beta β_m
0	-3.0	17.51	0.962	0
5	-5.2	17.51	0.962	0
10	-7.0	17.51	0.962	0
255	-4.7	27.57	0.937	0
260	-6.9	27.57	0.937	0
265	-8.7	27.57	0.937	0
360	-5.2	8.07	0.947	0
365	-7.4	8.07	0.947	0
370	-9.2	8.07	0.947	0
1040	-8.2	1.31	0.956	0
1045	-10.4	1.31	0.956	0
1050	-12.2	1.31	0.956	0
2730	-12.1	25.69	0.916	0
2735	-14.3	25.69	0.916	0
2740	-16.1	25.69	0.916	0
4600	-15.5	22.71	0.841	0
4605	-17.7	22.71	0.841	0
4610	-19.5	22.71	0.841	0

Bibliography

[1] Wikipedia. (2014, june) TEM waves. [Online]. Available: http://en.wikipedia.org/wiki/Circular_polarization

[2] Kraus, *Antennas - For All Applications*, 3rd ed. New York: McGraw-Hill, 2002.

[3] MVG Microwave Vision Group, "StarMIMO," *Product Brochure*, 2014.

[4] M. Rumney, *LTE and the Evolution to 4G Wireless - Design and Measurement Challenges.* New York: John Wiley & Sons, 2013.

[5] C. v. Gagern, "Decomposition test results from the second CTIA round robin test," *COST IC1004*, no. TD(13)07049, 2013.

[6] B. Auinger, M. Gadringer, A. Tankielun, C. v. Gagern, and W. Boesch, "Numerical analysis of the decomposition method using LTE reference antennas," in *International Conference on Computer and Network Engineering (ICCNE) 2014*, Dec 2014.

[7] "The golden angle: Phyllotaxis and epidermal cell reduction ratio." [Online]. Available: http://dgleahy.com/p27.html

[8] A. Tankielun and C. Gagern, "On spatial chracteristics of the decomposition method in MIMO OTA testing," 2014.

[9] Third Generation Partnership Project (3GPP), "Universal terrestrial radio access (UTRA) and evolved universal terrestrial radio access; verification of radiated multi-antenna reception performance of user equipment (UE)," pp. 1–138, March 2014.

[10] T. Zemen, "OFDMA/SC-FDMA basics for 3GPP LTE (E-UTRA)," April 2008.

[11] J. G. Proakis, *Digital Communications*, 5th ed. New York: McGraw-Hill, 2008.

[12] H. Zarrinkoub, *Understanding LTE with MATLAB - From Mathematical Modelling to Simulation and Prototyping*, 1st ed. Southern Gate, Chichester, West Sussex, UK: Wiley, 2014.

[13] I. Szini, "Reference antennas proposal for MIMO OTA," *COST IC1004*, no. TD(11)02009, Oct. 2011.

[14] G. Bauch, *Training on multiple antenna systems, 'Prinzipien der Mehrantennentechnik in LTE'*. Munich: Bauch, Gerhard, April 2012.

[15] K.-D. Kammeyer, M. Bossert, and N. Fliege, *Nachrichtenübertragung*, 5th ed. Berlin Heidelberg New York: Springer, 2004.

[16] J. R. Barry, E. A. Lee, and D. G. Messerschmitt, *Digital Communication*, 3rd ed. Berlin Heidelberg: Springer Science & Business Media, 2004.

[17] K. D. Kammeyer, *Mehrantennensysteme - räumliches Multiplexing und Nutzung von Raumdiversitäten (Trainingsunterlagen)*. München: Rohde & Schwarz, 2012.

[18] K. Simonyi, *Theoretische Elektrotechnik*. Berlin: VEB Deutscher Verlag der Wissenschaften, 1971.

[19] J. D. Kraus, *Electromagnetics With Applications*, 5th ed. Singapore: McGraw-Hill College, 1998.

[20] D. K. Cheng, *Field and Wave Electromagnetics*, 2nd ed. Amsterdam: Addison-Wesley, 1989.

[21] C. A. Balanis, *Antenna Theory - Analysis*, 3rd ed. New York: John Wiley & Sons, 2005.

[22] T. Taga, "Analysis of correlation characteristics of antenna diversity in land mobile radio environments," *Electronics and Communications in Japan, Part 1*, vol. 74, no. 8, pp. 101–115, September 1991.

[23] S. Ali and J. Warden, "Controlling coupling between two transmitting antennas for MIMO handset applications," in *Personal Indoor and Mobile Radio Communications (PIMRC), 2011 IEEE 22nd International Symposium on*, Sept 2011, pp. 2060–2064.

[24] H. Arun, A. Sarma, M. Kanagasabai, S. Velan, C. Raviteja, and M. Alsath, "Deployment of modified serpentine structure for mutual coupling reduction in MIMO antennas," *Antennas and Wireless Propagation Letters, IEEE*, vol. 13, pp. 277–280, 2014.

[25] C. S. Chuang, W. T. Hsu, and M. L. Chun, "A compact dual band tree-type MIMO antenna for mobile wireless access network application," in *Microwave Conference Proceedings (APMC), 2013 Asia-Pacific*, Nov 2013, pp. 1169–1171.

[26] G. J. Foschini and M. J. Gans, "On limits of wireless communications in a fading environment when using multiple antennas," in *Wireless Pers. Comm., Vol. 6, no.3*, March 1998, pp. 311–335.

[27] I. F. Chen and C. M. Peng, "Compact modified pentaband meander-line antenna for mobile handsets applications," *Antennas and Wireless Propagation Letters, IEEE*, vol. 10, pp. 607–610, 2011.

[28] S. Stein, "On cross coupling in multiple-beam antennas," *Antennas and Propagation, IRE Transactions on*, vol. 10, no. 5, pp. 548–557, September 1962.

[29] S. Zhang, A. A. Glazunov, Z. Ying, and S. He, "Reduction of the envelope correlation coefficient with improved total efficiency for mobile LTE MIMO antenna arrays: Mutual scattering mode," *Antennas and Propagation, IEEE Transactions on*, vol. 61, no. 6, pp. 3280–3291, June 2013.

[30] H. Singh, G. Pandey, P. Bharti, and M. Meshram, "A compact dual band MIMO/-diversity antenna for WLAN applications," in *Engineering and Systems (SCES), 2013 Students Conference on*, April 2013, pp. 1–5.

[31] S.-W. Lee, A. Fathy, S. El-Ghazaly, and V. Nair, "Evaluation of optimum position and orientation of laptop MIMO antennas using envelope correlation coefficients and mutual coupling parameters," in *Antennas and Propagation Society International Symposium, 2007 IEEE*, June 2007, pp. 2973–2976.

[32] V. Ssorin, A. Artemenko, A. Sevastyanov, and R. Maslennikov, "2.7 GHz two element MIMO antenna system for modern USB dongle," in *Antennas and Propagation (EUCAP), 2012 6th European Conference on*, March 2012, pp. 1955–1959.

[33] G. Srinivas, D. Jabin, and A. Singh, "Multiband MIMO antenna with reduction in mutual coupling and ECC," in *Engineering and Systems (SCES), 2014 Students Conference on*, May 2014, pp. 1–5.

[34] L. Zhanmeng, L. Chunlan, Y. Luqu, J. Jianxin, and Y. Jie, "A novel compact dual-band MIMO antenna for WLAN application," in *Microwave and Millimeter Wave Technology (ICMMT), 2012 International Conference on*, vol. 3, May 2012, pp. 1–4.

[35] M. Eleiwa, "Correlation characteristics of diversity antennas in mobile environments," in *Information, Communications Signal Processing, 2007 6th International Conference on*, Dec 2007, pp. 1–4.

[36] X. Zhou, X. Quan, and R. Li, "A dual-broadband MIMO antenna system for GSM/UMTS/LTE and WLAN handsets," *Antennas and Wireless Propagation Letters, IEEE*, vol. 11, pp. 551–554, 2012.

[37] Q. Wang, D. Plettemeier, H. Zhang, K. Wolf, and E. Ohlmer, "Diversity performance of an optimized meander PIFA array for MIMO handsets," in *Antennas and Propagation (EuCAP), 2010 Proceedings of the Fourth European Conference on*, April 2010.

[38] R. Vaughan and J. Andersen, "Antenna diversity in mobile communications," *Vehicular Technology, IEEE Transactions on*, vol. 36, no. 4, pp. 149–172, Nov 1987.

[39] W. Jakes, *Microwave Mobile Communication*, 1st ed. New York: IEEE Press, 1974.

[40] I. Salonen and P. Vainikainen, "Estimation of signal correlation in antenna arrays," in *Proceedings of the 12th International Symposium on Antennas (JINA 2002)*, vol. 2, Nov 2002, pp. 383–386.

[41] A. Diallo, C. Luxey, P. Le Thuc, R. Staraj, and G. Kossiavas, "Diversity performance of multiantenna systems for UMTS cellular phones in different propagation environments," *International Journal of Antennas and Propagation*, 2008.

[42] J. T. Thaysen and K. B. Jokobsen, "Envelope correlation in (N,N) MIMO antenna array from scattering parameters," in *Microwave and Optical Technology Letters*, vol. 48, May 2006, pp. 832–835.

[43] Z. Ying, V. Plicanic, T. Bolin, G. Kristensson, and A. Derneryd, "Characterization of multi-channel antenna performance for mobile terminal by using near field and far field parameters," in *COST 273 TD(04)(095), Göteborg, Sweden*, June 2004.

[44] A. Derneryd and G. Kristensson, "Diversity performance of a small terminal antenna for UMTS," in *Electronics Letters, Vol. 40, no. 7, pp. 401-402,*, June 2004.

[45] Derneryd, "Antenna signal correlation and its relation to the impedance matrix," in *Electronics Letters*, vol. 40, April 2004.

[46] A. Derneryd, "Signal correlation including antenna coupling," *Electronic Letters*, vol. 40, April 2004.

[47] M. Foegelle, "Creating a complex multipath environment simulation in an anechoic chamber," *Microwave Journal*, eigth 2010.

[48] J. Thorpe and J. Bennett, "Characterising the quiet zone of an anechoic chamber," in *Antenna Measurements and SAR, 2004. AMS 2004. IEE*, May 2004, pp. 25–28.

[49] C. Sirles, J. Mantovani, A. Howland, and B. Hart, "Anechoic chamber performance characterization using spherical near-field imaging techniques," in *Antennas and Propagation, 2009. EuCAP 2009. 3rd European Conference on*, March 2009, pp. 1734–1738.

[50] D. Parveg, T. Laitinen, A. Khatun, V. M. Kolmonen, and P. Vainikainen, "Calibration procedure for 2-D MIMO over-the-air multi-probe test system," in *Antennas and Propagation (EUCAP), 2012 6th European Conference on*, March 2012, pp. 1594–1598.

[51] W. Fan, X. Carreno, J. Ashta, J. Nielsen, G. Pedersen, and M. Knudsen, "Channel verification results for the SCME models in a multi-probe based MIMO OTA setup," in *Vehicular Technology Conference (VTC Fall), 2013 IEEE 78th*, Sept 2013, pp. 1–5.

[52] T. Laitinen, P. Kyosti, J. P. Nuutinen, and P. Vainikainen, "On the number of OTA antenna elements for plane-wave synthesis in a MIMO-OTA test system involving a circular antenna array," in *Antennas and Propagation (EuCAP), 2010 Proceedings of the Fourth European Conference on*, April 2010, pp. 1–5.

[53] W. Fan, X. Carren, J. Nielsen, K. Olesen, M. Knudsen, and G. Pedersen, "Measurement verification of plane wave synthesis technique based on multi-probe MIMO-OTA setup," in *Vehicular Technology Conference (VTC Fall), 2012 IEEE*, Sept 2012, pp. 1–5.

[54] A. Khatun, V. Kolmonen, T. Laitinen, and K. Nikoskinen, "Clarification of uncertainties in MIMO over-the-air multi-probe test systems," in *Antennas and Propagation (EuCAP), 2013 7th European Conference on*, April 2013, pp. 1427–1431.

[55] W. Fan, J. Nielsen, X. Carreno, J. Ashta, G. Pedersen, and M. Knudsen, "Impact of system non-idealities on spatial correlation emulation in a multi-probe based MIMO OTA setup," in *Antennas and Propagation (EuCAP), 2013 7th European Conference on*, April 2013, pp. 1663–1667.

[56] A. Scannavini, L. Foged, and N. Gross, "OTA throughput testing of multi-antenna terminals by using StarMIMO test range," in *Antennas and Propagation (EUCAP), Proceedings of the 5th European Conference on*, April 2011, pp. 1554–1557.

[57] S.-S. Oh, J.-M. Kim, J.-H. Yun, and S.-Y. Kang, "Antenna measurement method in fresnel region by phi-variation scanning," *Antennas and Wireless Propagation Letters, IEEE*, vol. 7, pp. 206–209, 2008.

[58] Y. Jing, Z. Wen, H. Kong, S. Duffy, and M. Rumney, "Two-stage over the air (OTA) test method for MIMO device performance evaluation," in *Antennas and Propagation (APSURSI), 2011 IEEE International Symposium on*, July 2011, pp. 71–74.

[59] Agilent Technologies and Tri-L Solutions, "Incorporating self-interference into the two-stage method," in *3GPP TSG RAN WG 4 Meeting 66 MIMO OTA Ad hoc*, March 2013.

[60] C. Gagern and A. Tankielun, "Test results from the second CTIA round robin test," February 2013.

[61] A. Tankielun, "Two-Channel Method for OTA performance measurements of MIMO-enabled devices, rohde & schwarz munich," September 2011.

[62] P. Prusinkiewicz and A. Lindenmayer, *The Algorithmic Beauty of Plants*, 1st ed. New York: Springer, 1990.

[63] A. Adardour, G. Andrieu, and A. Reineix, "Influence of a stirrer on the cavity modes within a reverberation chamber," in *Electromagnetic Compatibility (EMC EUROPE), 2012 International Symposium on*, Sept 2012, pp. 1–4.

[64] Adardour, G. Andrieu, and A. Reineix, "Determination of the quasi-ideal reverberation chamber minimum frequency according to the mode stirrer geometry," in *Electromagnetic Compatibility (EMC EUROPE), 2012 International Symposium on*, Sept 2013.

[65] J. F. Dawson and L. Arnaut. (2007, june) Reverberation (mode-stirred) chambers for electromagnetic compatibility. [Online]. Available: http://www.compliance-club.com/archive/old_archive/030530.htm

[66] P. Plaza-Gonzalez, J. Monzo-Cabrera, J. Catala-Civera, and D. Sanchez-Hernandez, "New approach for the prediction of the electric field distribution in multimode microwave-heating applicators with mode stirrers," *Magnetics, IEEE Transactions on*, vol. 40, no. 3, pp. 1672–1678, May 2004.

[67] P. Plaza Gonzalez, J. Monzo Cabrera, J. Catala Civera, and D. Sanchez Hernandez, "Effect of mode-stirrer configurations on dielectric heating performance in multimode microwave applicators," *Microwave Theory and Techniques, IEEE Transactions on*, vol. 53, no. 5, pp. 1699–1706, May 2005.

[68] Z. Bo, Y. Zhiyong, and H. Jinliang, "Comparison on the test results between reverberation chamber and anechoic chamber," in *Electromagnetic Compatibility (APEMC), 2012 Asia-Pacific Symposium on*, May 2012, pp. 769–772.

[69] C. Bruns and R. Vahldieck, "A closer look at reverberation chambers - 3-D simulation and experimental verification," *Electromagnetic Compatibility, IEEE Transactions on*, vol. 47, no. 3, pp. 612–626, Aug 2005.

[70] A. Ubin and M. Jenu, "Field uniformity evaluation of different stirrer structure in a reverberation chamber," in *Applied Electromagnetics (APACE), 2012 IEEE Asia-Pacific Conference on*, Dec 2012, pp. 32–35.

[71] A. Paulraj, R. Nabar, and D. Gore, *Introduction to Space-Time Wireless Communications.* Cambridge: Cambridge University Press, 2003.

[72] D. Kececioglu, *Reliability Engineering Handbook Volume 1.* DESTech Pulications, Inc., 2002.

[73] 3GPP, "Technical specification group radio access network; evolved universal terrestrial radio access (E-UTRA); user equipment (UE) radio transmission and reception (Release 12)," September 2014.

[74] C. Oestges, "Validity of the Kronecker model for MIMO correlated channels," in *Vehicular Technology Conference, 2006. VTC 2006-Spring. IEEE 63rd*, vol. 6, May 2006, pp. 2818–2822.

[75] ETSI AND 3GPP, "Technical specification: LTE; evolved universal terrestrial radio access (E-UTRA); base station (BS) conformance testing (3GPP TS 36.141 version 12.5.0 Release 12)," October 2014.

[76] Wikipedia. (2014) LTE. [Online]. Available: http://en.wikipedia.org/wiki/LTE_% 28telecommunication%29

[77] Third Generation Partnership Project (3GPP), "Technical specification group radio access network; feasibility study for evolved universal terrestrial radio access (UTRA) and universal terrestrial radio access network (UTRAN) (release 12)," September 2014.

[78] M. Wylie-Green and T. Svensson, "Throughput, capacity, handover and latency performance in a 3GPP LTE FDD field trial," *Global Telecommunications Conference (GLOBECOM 2010), 2010 IEEE*, Dec 2010.

[79] M. R. Soleymani, Y. Gao, and V. U., *Turbo Coding for Satellite and Wireless Communications.* New York, Boston, Dordrecht, London, Moscow: Kluwer Academic Publishers, 2002.

[80] U. Mengali, *Synchronization Techniques for Digital Receivers*, 1997th ed. New York: Plenum Press, 1997.

[81] N. J. Salkind, *Encyclopedia of Research Design*, 1st ed. Thousand Oaks, California: Sage, 2010.

[82] E. Telatar, "On limits of wireless communications in a fading environment when using multiple antennas," in *European Transactions on Telecommunications, Vol. 10, No. 6*, Nov/Dec 1999, pp. 585–595.

[83] W. Fan, I. Szini, M. Foegelle, J. Nielsen, and G. Pedersen, "Measurement uncertainty investigation in the multi-probe ota setups," in *Antennas and Propagation (EuCAP), 2014 8th European Conference on*, April 2014, pp. 1068–1072.

[84] Third Generation Partnership Project (3GPP), "Errors and uncertainties in the mimo ota measurements r4-131673, Meeting 65, New Orleans," November 2012.

[85] 3GPP, "Measurement uncertainty evaluation of multi-probe method, Meeting 66, Chicago," November 2012.

[86] A. Tankielun, "On spatial characteristics of the decomposition method in MIMO OTA testing," *EuCAP 14*, Oct. 2014.

[87] CTIA, "Draft CTIA MIMO OTA test plan version 0.2 (CTIA MOSG131214; sub working group document available to CTIA sub-working group members)," December 2013.

[88] Rohde and Schwarz, "Verification of channel model realization in a baseband fading simulator for MIMO OTA testing," in *(R4 136807), TSG-RAN WG4 Meeting 69, San Francisco, California, USA*, November 2013.